PHILOSOPHICAL TRANSACTIONS OF THE ROYAL SOCIETY A MATHEMATICAL, PHYSICAL & ENGINEERING SCIENCES

Stress Patterns in an Interplate Shear Zone: An Effective Anisotropic Model and Implications for the Transverse Ranges, California

E. R. Ivins and G. A. Lyzenga

Phil. Trans. R. Soc. Lond. A 1986 **318**, 285-347
doi: 10.1098/rsta.1986.0077

Phil. Trans. R. Soc. Lond. A **318**, 285–347 (1986) [285]
Printed in Great Britain

STRESS PATTERNS IN AN INTERPLATE SHEAR ZONE: AN EFFECTIVE ANISOTROPIC MODEL AND IMPLICATIONS FOR THE TRANSVERSE RANGES, CALIFORNIA

By E. R. IVINS and G. A. LYZENGA
Jet Propulsion Laboratory, California Institute of Technology, Pasadena, California 91109, *U.S.A.*

(*Communicated by D. P. McKenzie, F.R.S. – Received* 12 *October* 1984)

CONTENTS

Strong lateral variations in geological structure within a transcurrent interplate deformation boundary have a substantial influence upon the way in which ambient stress is related to the relief of regional stress within the boundary zone. Much of the crustal deformational structure in southern California and environs consists of a conjugate wrench fault system. The Quaternary fault system consists of a series of parallel and sub-parallel strike-slip faults that are causally related to the horizontal interplate shearing. A prominent crustal structural inhomogeneity is the Transverse Ranges, where fault orientation is east–west, transverse to the dominant north-westerly trend.

We investigate some of the consequences of this transverse inhomogeneity on the overall stress and strain field in the southern California region. The activity of the strike–slip (or wrench) system to the south and north of the Transverse Ranges suggests a mechanical model consisting of weak zones with a relatively strong degree of orientation. An effective anisotropy model is constructed based on: (1) a two-component laminate model consisting of competent unfaulted rock adjacent to incompetent faulted rock; (2) theoretical results for the weakening of a plate due to a doubly periodic array of cracks; and (3) finite element treatment of a checkerboard array of cracks. The fundamental parameter for weakening is $\Lambda \equiv 1-L$, where L is a non-dimensional form of Biot's slide modulus. In the limit of $\Lambda \to 1$ the crust becomes extremely weak and anisotropic, and as $\Lambda \to 0$ the condition of a strong, isotropic crust is recovered. The components of the stiffness (or compliance) matrix are directly related to the mechanical properties of a finite width fault zone, or to the average fault spacing and asperity density within a particular geological province, or both. An elastic plate model that incorporates the stress–strain channelling caused by multiple, oriented fault systems is constructed. The plate is assumed to be stressed by pure shearing forces maintained at infinity. The ambient field then corresponds to the north–south compressional, east–west extensional tectonic régime that dominates North-American–Pacific interplate shear along the San Andreas fault, California. Embedded within the plate is an elliptical inclusion in which multiple fault stress channelling also occurs. The inclusion thus mimics the misaligned structure of the Transverse Ranges in southern California. The boundary value problem associated with the model is treated both analytically and with finite element computations. The simple model predicts (i) the enhanced seismic energy release associated with the Transverse Ranges; and (ii) the clockwise rigid rotation indicated by a palaeomagnetic studies. The relatively simple nature of the model helps to isolate those features of the southern California tectonic stress régime that might be attributed to the transverse orientation of the Transverse Ranges. Stress channelled into the crosscutting tectonic structure from the ambient interplate field is significant. Contradirectionality alone cannot provide an explanation for the enhanced north–south compressive stress relative to east–west extension.

1. Introduction

The application of dislocation theory to the problem of faulting has profoundly affected our understanding of earthquake mechanics. Dislocation models that are based upon prescribed fault slip have provided valuable information about the changes in stress associated with

earthquakes. The models allow us to understand how deformation and stress occur in the vicinity of a fault surface. More precisely, these models allow us to estimate the geodetic depth: the length scale over which faults have a strong influence upon the ambient stress-strain field (Kasahara 1981; Mavko 1981). Chinnery (1963) demonstrated that the geodetic depth is of the order of the along-strike lateral extent of a finite fault and that most of the stress change occurs quite close to the fault surfaces. Crack models of faults exhibit precisely these features and probably have greater versatility in connecting series of earthquake cycles with one another (Barenblatt *et al.* 1981).

Recently, the concepts of dislocation and crack mechanics have found application in the treatment of geological problems associated with the length and time scales of interplate deformation. Rodgers & Chinnery (1973) have shown that a static elastic model of a bent dislocation is a reasonable mechanical analogue of the Big Bend feature of the San Andreas fault in southern California. They demonstrated that the Big Bend probably causes an enhancement of regional tectonic stress. Bird & Piper (1980) have constructed a dynamic model treatment of cumulative strain, seismicity and creep along numerous southern California faults. By attempting to match geodetic constraints with discrete motions along a series of dislocations (faults) Bird & Piper (1980) concluded that the northwesterly striking strike-slip (or wrench) system of southern California (see figure 1) acts to significantly weaken the crust over a broad North American–Pacific interplate zone of shear. In this paper we investigate how this northwesterly directional weakening interacts with the east–west directional weakening caused by the Transverse Ranges (see figure 1). To capture the constitutive properties of directional weakening we employ the theory of anisotropic elasticity. Crustal rock within a fault zone may actually creep owing to its relatively low frictional resistance to sliding (Byerlee 1978). This anelastic process is capable of accounting for a large portion of the strain accumulation for time scales of 100 years or greater. However, elastic models can accurately reveal the spatial distribution of recoverable strain energy, a property of fundamental importance to the process of earthquake generation (Tsuboi 1956; Rice 1980). Model properties of the anisotropic theory are treated at length here. The primary focus of this paper, however, is to use the anisotropic constitutive theory to investigate how the northwest and east–west directional fault systems channel strain, stress and recoverable elastic work. An implicit assumption is that such a simple model may reveal the cumulative effects of the elastic interaction among the two non-aligned parallel sets of faults over the duration of many great earthquake cycles.

Late Tertiary and Quaternary right lateral displacement along the North-American–Pacific plate boundary has been largely accommodated by motion along the Hosgri–San Gregorio and San Andreas faults (Graham & Dickinson 1978). However, overall Neogene (*ca.* 18 Ma) right lateral horizontal shearing deformation cannot be explained as a sole result of activity along these two discontinuities. A seismically active tectonic fabric exists in this region and consists of a system of parallel and sub-parallel minor fault systems. Chinnery (1966) has shown how the stress field around a single dislocation gives rise to a secondary strike-slip system when long-term deformations are large. The clay analogue experiments of Tchalenko (1970) and Wilcox *et al.* (1973) suggest that the set of conjugate Riedel shears, known as a wrench fault system, associated with the same shearing that results in major transform faulting, accounts for both this additional deformation field and the observed regularity in orientation of this minor system. Wilcox *et al.* noted that increasingly large deformation tends to transform the conjugate system into a parallel braided pattern.

With the use of a compilation of quantitative estimates of the principal stress directions from

well determined earthquake focal mechanisms, late Cainozoic geological indicators, *in situ* estimates and hydro-fracturing experiments, Zoback & Zoback (1980*b*) have shown that the tectonic stress régime in southern California and environs is one of pure shear. This pure shear is exactly that which would be predicted on the basis of the directions of relative motions of North American and Pacific plates in the Minster & Jordan (1978) global tectonic model. This lithospheric pure shear state is equivalent to north–south compression and east–west extension acting at a distance. The Transverse Ranges (see map in figure 1) are a longitudinal structure whose axis runs perpendicular to the north–south compressional axis. The Ranges are dominated by reverse thrust faults whose strikes are about 90°, running across the structural fabric of the strike-slip faults (of strikes 30–45°) surrounding it. The seismicity of the Transverse Ranges has revealed a relatively complicated fault structure, particularly as deduced from after-shock sequences (Whitcomb *et al.* 1973; Langston 1978; Corbett & Johnson 1982). Fault surfaces are concave upwards forming an imbricate structure with the deepest portions of very shallow thrusting angle (Yeats 1981, 1983). Earthquake focal mechanisms within the Ranges indicate that the north–south compression is enhanced over east–west extension (Yerkes & Lee 1979). It has been suggested that the Quaternary compressional tectonics of the Ranges might be attributed to the transpression caused by the Big Bend feature of the San Andreas fault (Yerkes *et al.* 1981; Dickinson 1981). By solving a series of analytical and finite element models we demonstrate that this 'transpressional' stress state is likely to be enhanced by the transverse structural trend of the Transverse Ranges.

It is possible to construct a simple model of the stress environment of the Transverse Ranges that ignores the contribution due to the Big Bend (or of the San Andreas in specific), but which focuses attention upon the activity of all northwesterly striking faults of southern California and environs. Activity of the northwesterly striking San Clemente, Elsinore, Newport–Inglewood, San Jacinto, Santa Lucia and Sur–Nacimento systems and those of the Mojave region (see figure 1) are all envisioned as being zones of weakness and as having structural significance. The model assumes that a sheared thin elastic plate of infinite lateral extent is weakened by a spatial distribution of both northwesterly and east–west oriented faults. We approximate the northwesterly striking faults to pervade everywhere, except in a local longitudinal region that contains solely east–west striking faults. If the longitudinal region is approximated as elliptical this physical situation can be posed formally as a mathematical boundary–value problem. Analytical solutions to the equilibrium equations of incremental elasticity exist that allow the stress and strain field both within and around this discordant faulting heterogeneity to be fully treated. Model solutions demonstrate that it is possible to obtain the enhanced compressional state of the Ranges by the stress channelling that occurs as a result of the geometry of the ambient tectonic stress field alignment and the bidirectionality of the multiple parallel fault structure. Depending upon the faulting anisotropy style that we choose for the longitudinal elliptical structure we may generate any one of a number of deformational fields. The most striking feature revealed in both finite-element and analytical solutions is that the Ranges act a concentrator of regional stress. However, only a thrust-dominated anisotropy model generates an enhanced compressional state.

Hill (1982) has proposed a model that quantitatively relates data pertaining to earthquake focal mechanisms and overall geological structure in both California and Nevada. Hill's (1982) kinematic block model organizes a rather unified picture of how the overall north–south compressional, east–west extensional stresses which act along the western North American continent as whole (Zoback & Zoback 1980*a*, *b*) are related to the current activity of specific faults in California and its environs.

PHILOSOPHICAL TRANSACTIONS OF THE ROYAL SOCIETY A MATHEMATICAL, PHYSICAL & ENGINEERING SCIENCES

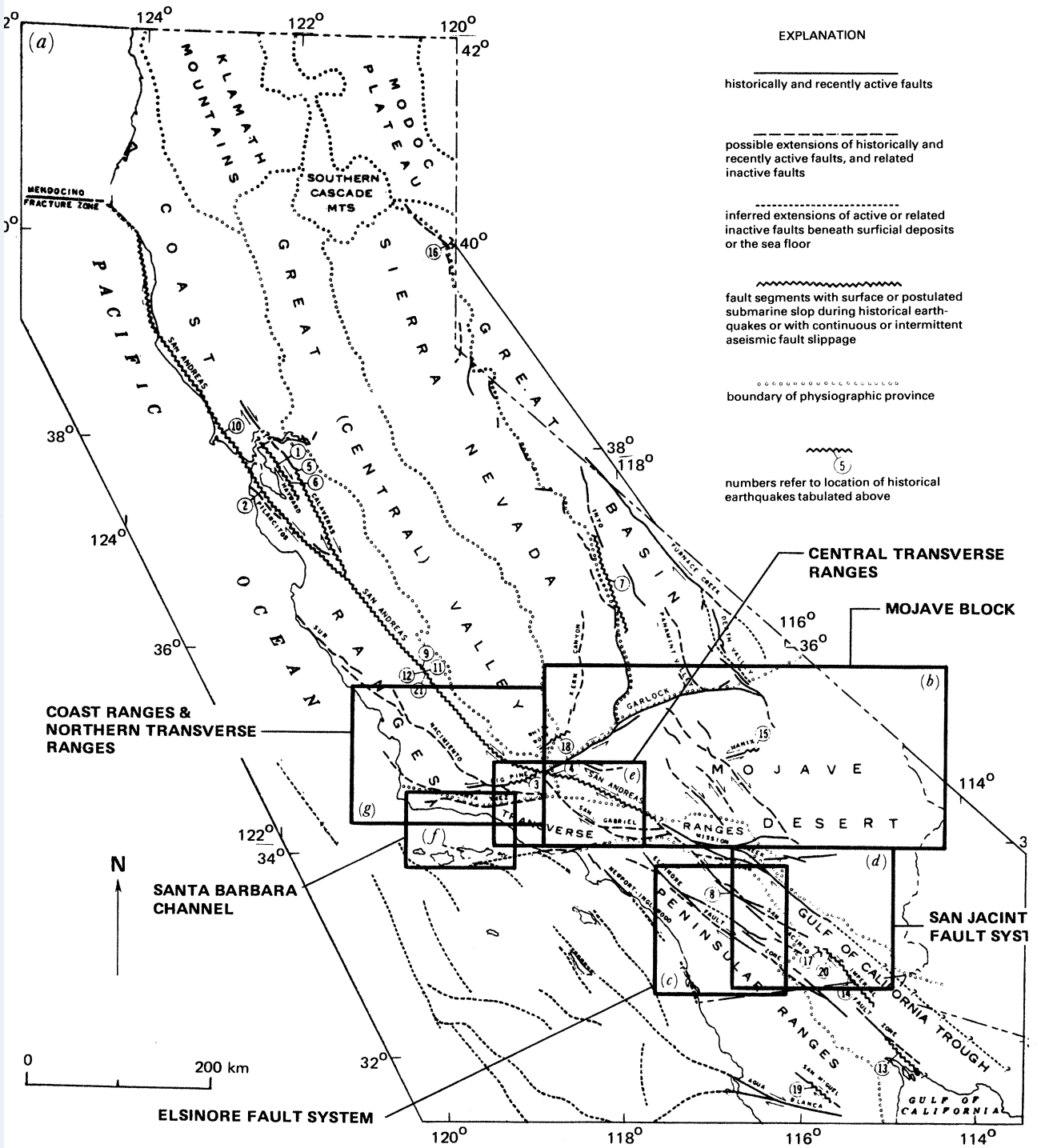

FIGURE 1. (*a*) Map of active Quaternary faults, adapted from Burk & Moores (1968). (Circled numbers correspond to references given by Burk & Moores). The inset maps (*b–g*, on the following pages) are: (*b*) the Mojave Block, (*c*) the Elsinore fault system, (*d*) the San Jacinto fault system, (*e*) the central Transverse Ranges, (*f*) the Santa Barbara Channel, and (*g*) Coast Ranges and northern Transverse Ranges. The numbers on faults in the Mojave Block inset correspond to names listed in Norris & Webb (1977, p. 132). The inset of the Coast Ranges is modified after Veeder & Brown (1968) and Hall (1981*b*); all others are reproduced from Norris & Webb (1977).

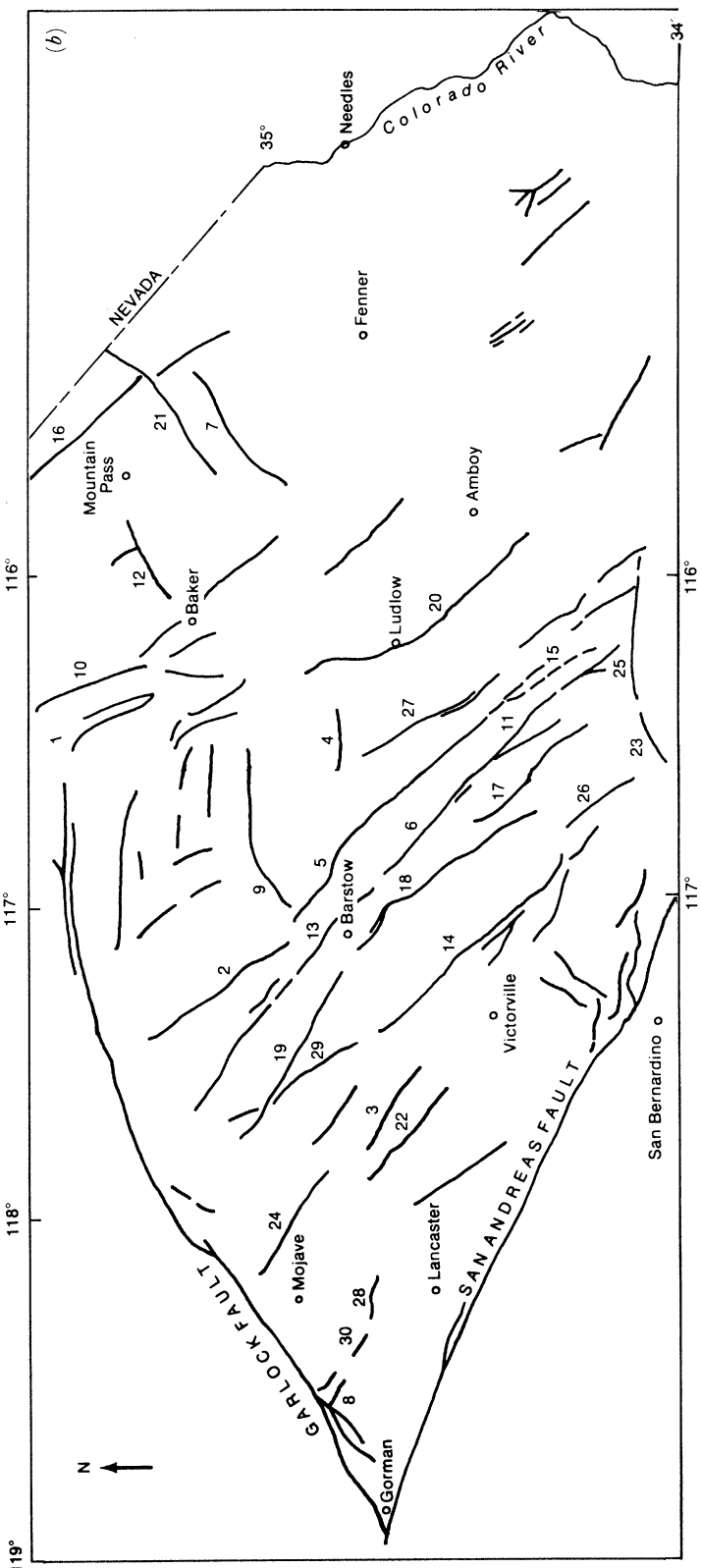

FIGURE 1 (*b*). For legend see p. 289.

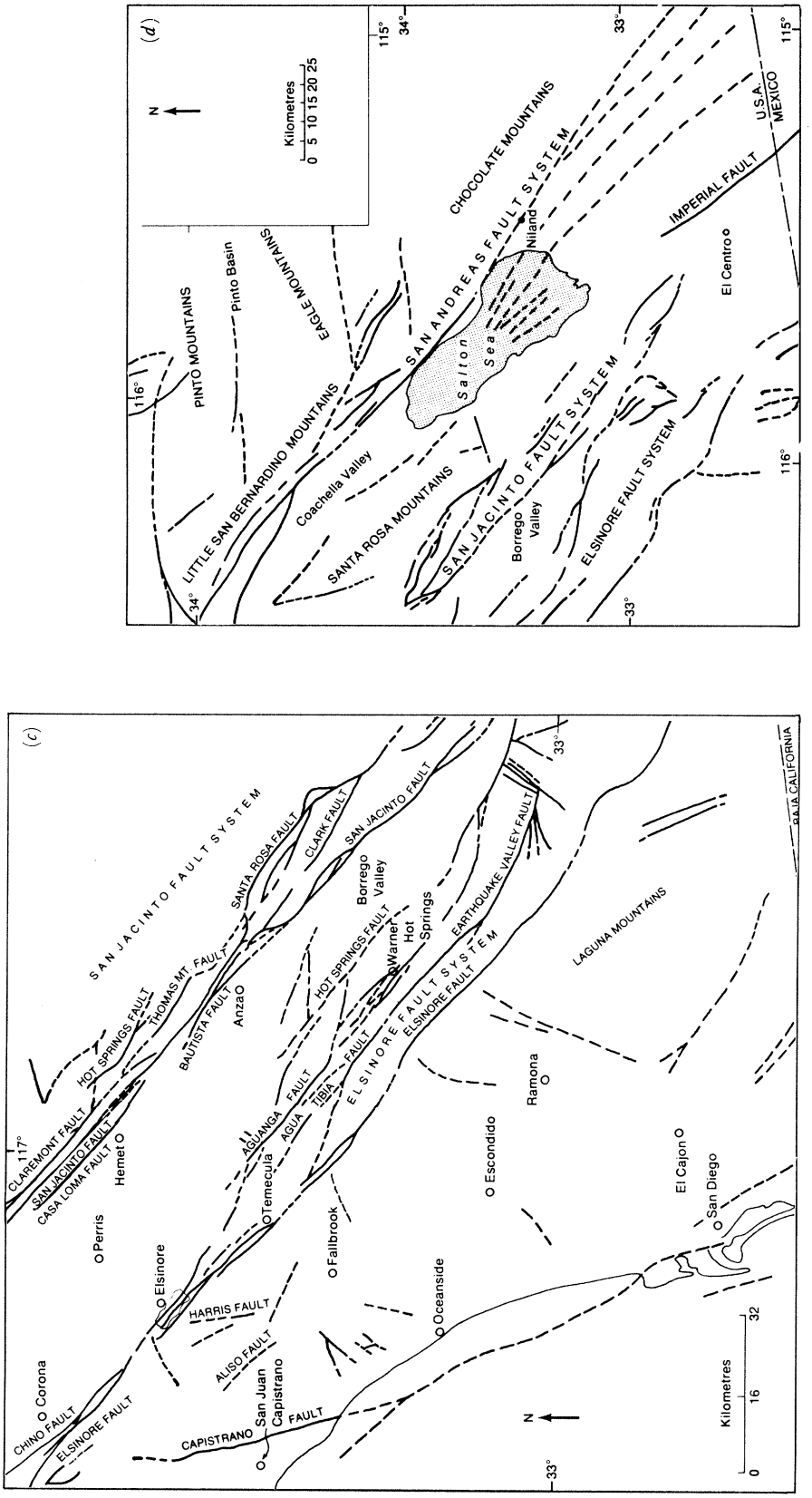

FIGURE 1 (*c*, *d*). For legend see p. 289.

PHILOSOPHICAL TRANSACTIONS OF THE ROYAL SOCIETY A MATHEMATICAL, PHYSICAL & ENGINEERING SCIENCES

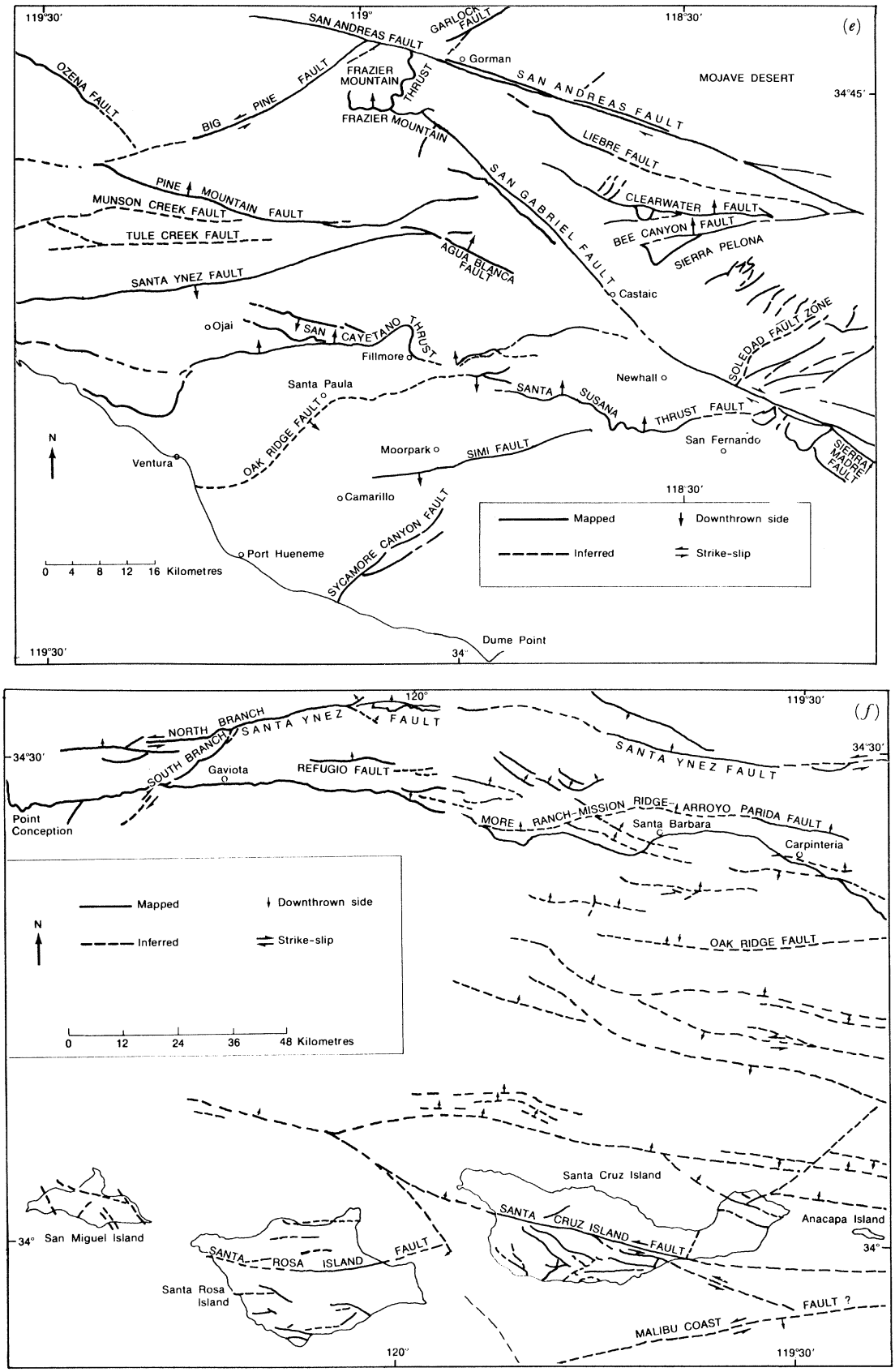

FIGURE 1 (*e*, *f*). For legend see p. 289.

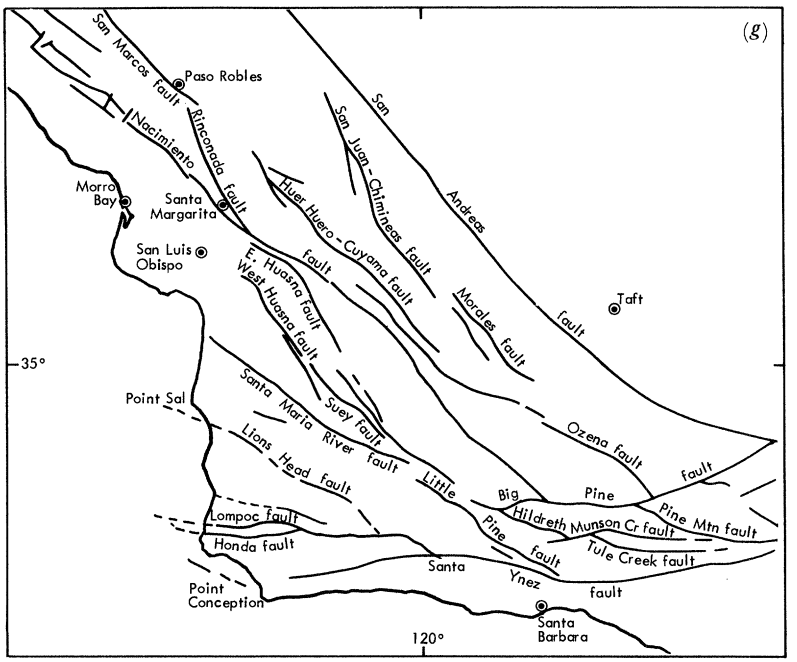

FIGURE 1 (*g*). For legend see p. 289.

The use of regional patterns in geological structure and seismicity to constrain the stress–strain state assumes that fracture occurs repetitively on time scales of 10^2–10^6 years, along pre-existing planes of weakness. In this paper we shall use the concept that pre-existing fault planes are zones of weakness and that they accommodate large strains and locally reduce ambient tectonic stresses.

Both fault directionality and the effective weakening can be accounted for by considering the crust to be elastically anisotropic. We develop three different approaches to crustal weakening and anisotropy. The formulations include: (1) a two-component material that forms a laminate model; (2) a plate crack model in which both mode I and II crack deformation occurs; and (3) a plate crack model in which only shearing (mode II) along a crack surface is allowed. Some simple analytical cases demonstrate the pronounced effect that multiple and oriented faulting can have upon tectonic stress–strain fields when considering the length scales associated with intraplate boundary shearing.

Sbar (1982) recently computed static elastic stress fields in a sheared plate containing a zone of material whose isotropic stiffnesses are reduced by a factor of ten. His results elucidate possible mechanical causes for spatial variation of tectonic stress in the northern Basin and Range province in western North America. This paper explores ways in which such weakening can be put on firmer theoretical grounds and then demonstrates that regional heterogeneity in weakening strongly influences the local crustal stress pattern.

2. TECTONIC SETTING

The southern California region encompasses a zone of transition from the short ridges connected by long transforms, which are characteristic of the Gulf of California trough, to a transcurrent transform tectonic style to the north. The transition occurs in the vicinity of the

PHILOSOPHICAL TRANSACTIONS OF THE ROYAL SOCIETY A MATHEMATICAL, PHYSICAL & ENGINEERING SCIENCES

Imperial fault (see figure 1). The northern Gulf of California is dominated by the long transform segments. Right lateral strike-slip is the pervasive faulting style of northern Baja California (Puente & de la Peña 1979). The primary fault trend there is northwesterly. This trend continues northward into the Elsinore, San Jacinto and offshore fault systems of southern California (see maps in figure 1).

TABLE 1. SOURCE LITERATURE FOR REGIONAL SEISMICITY AND TECTONICS

(Selected on the basis of recency, comprehensiveness and bearing upon Quaternary deformation.)

region (see figure 1 maps)	reference
Southern Coast Ranges	Dibblee (1976); Page (1981); Gawthrop (1978)
Mojave Block	Garfunkel (1974); Cummings (1976); Dokka (1983)
Western & Central Transverse Ranges (including Santa Barbara Channel)	Hadley & Kanamori (1977); Corbett & Johnson (1982); Sylvester & Darrow (1979); Yerkes & Lee (1979); Yeats (1983); Langston 1978; Yerkes *et al.* (1981); Pechmann (1983)
San Jacinto	Sylvester & Smith (1976); Ebel & Helmberger (1982); Sharp (1981)
Elsinore	Allison *et al.* (1978); Crowell (1981)

The linear trend associated with the Malibu Coast fault strikes east–west towards the Mission Creek fault below the Mojave Desert (see both large and inset maps of figure 1) marks the abrupt southern boundary that separates Transverse Ranges and the northwesterly trending right lateral strike-slip system. The Mojave block also contains numerous northwesterly striking faults (see figure 1). However, this region has relatively low historical seismicity.

The bend of the San Andreas, the left lateral Big Pine and Santa Ynez faults occurs in a region of transition from the northern extent of the Transverse Ranges to the major transform style that occurs to the Medicino triple junction. North of the Transverse Ranges the Sur–Nacimiento, Hosgri–San Gregorio and Santa Lucia Bank fault systems are also active (Gawthrop 1978). However, historically recorded seismicity indicates that this region releases at least an order of magnitude less tectonically generated elastic energy in the form of moderate to large earthquakes ($M \lesssim 7$) relative to their northwesterly striking counterparts to the south of the Transverse Ranges (Allen *et al.* 1965). Contemporary deformation rates in the Southern Coast Ranges are not well documented.

Within the Transverse Ranges faulting trends are primarily east–west. The eastern Transverse Ranges are separated and slightly offset from the western and central Ranges by the San Andreas fault. The two east–west trending faults that bound the Pinto Mountains from the north and the Eagle Mountains from the south (see the San Jacinto fault system inset map of figure 1) also bound the eastern Transverse Ranges. Later in this paper we shall consider the mechanical implications of the contrariant direction of faults within the Transverse Ranges with respect to the overall trend (northwesterly). When the San Andreas can be considered perfectly locked within the region which separates the eastern from western Transverse Ranges, then the Transverse Ranges can be considered as unified tectonic block. However, this is probably not generally true. Consequently, in this paper we shall often, for the sake of brevity, refer to the western and central Transverse Ranges collectively as the Transverse Ranges, and distinguish these from the eastern Transverse Ranges.

The mid-Miocene San Gabriel fault of the central Transverse Ranges accommodated considerable horizontal strain (Crowell 1952). Quaternary activity in the Transverse Ranges is accompanied by both strike-slip and thrusting deformation (Briggs *et al.* 1977). Thrusting,

however, is by far dominant. The western branch of the Santa Ynez fault and the Santa Cruz Island and Santa Rosa Island faults are among the most notable east–west striking features (Sylvester *et al.* 1970). Seismic waveforms from earthquakes in the middle portion of the western Transverse Ranges reveal that fault planes are apparently contorted and geometrically complex at depth (0–20 km) (Langston 1978; Yeats 1981). It is not clear how the relative motion of the North American and Pacific plates is accommodated at depth beneath the Transverse Ranges. Studies of focal mechanisms of earthquakes south of the Santa Ynez fault indicate the existence of an imbricate structure of reverse and thrust faults whose dips become nearly horizontal at depths greater than 15 km (Corbett & Johnson 1982). Detachment of the upper 15–20 km of lithosphere from its base is strongly suggested and would be consistent with continuous large clockwise rotation of the region since the late Miocene (Luyendyk *et al.* 1980). Stauffer (1967) has shown that sediment deposits in the Santa Ynez Mountains in the vicinity of the Santa Ynez and Big Pine faults are due to an early Tertiary continental shelf. Together with lithological evidence (Baird *et al.* 1974; Yeats *et al.* 1974; Crouch 1979), this supports the idea that the Transverse Ranges have undergone significant allochthonous rotational motion during the Neogene. Hall (1981*a*, *b*) supports the view that this Neogene rotation was counter-clockwise. Palaeomagnetic evidence (Kamerling & Luyendyk 1979; Luyendyk *et al.* 1980) indicates that this motion was clockwise rotational. The large left lateral offset (10–30 km) inferred along the Santa Ynez fault since early Miocene (Sylvester & Darrow 1979) is consistent with the notion that there has been significant rotational and translational motion.

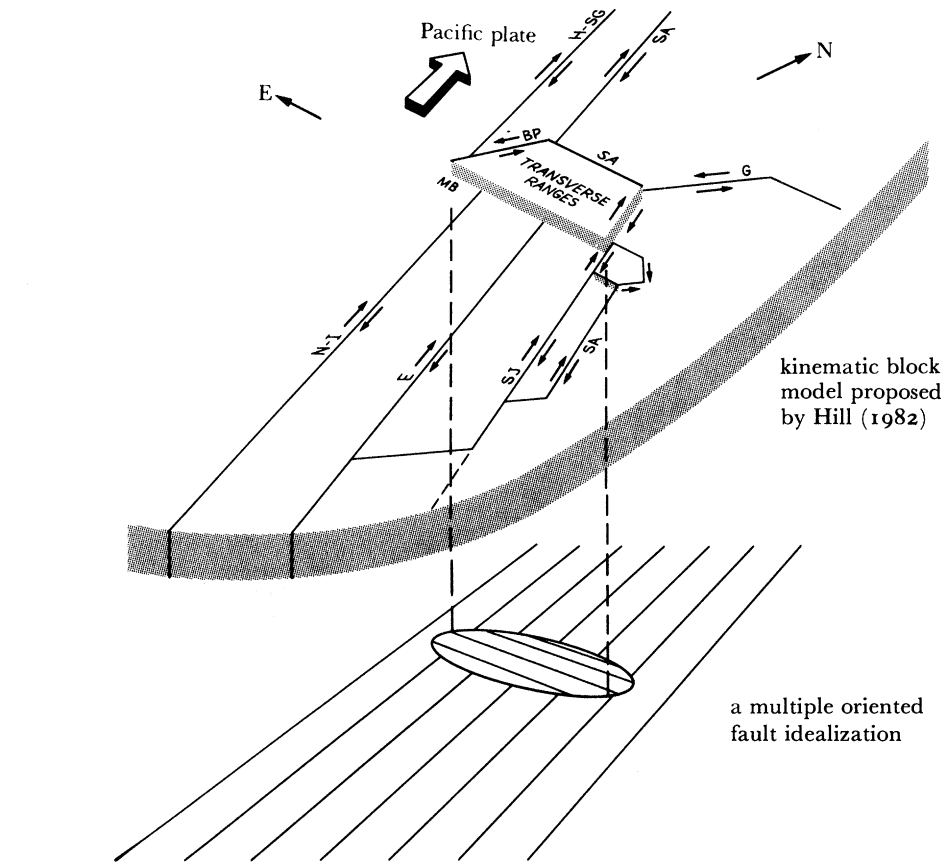

FIGURE 2. Three-dimensional view of fault block model proposed by Hill (1982).

Hill (1982) has proposed a kinematic block model that explains some of the relations between earthquake focal mechanisms on major faults, overall geological structure and relative plate motion. In order to test and quantify a block model adequately, Hill (1982) made some useful simplifying assumptions about the geometry. In figure 2 we have redrawn a portion of Hill's geometrical idealization. The underlying theme of the block model is that seismic activity and periodic plastic straining relieve the build-up of ambient tectonic stress to a degree sufficient to inhibit incipient failure of block interiors. Hence blocks are truly seen as being rigid.

In figure 2 projections are drawn from the western and eastern ends of the western and central Transverse Ranges, respectively, to ends of the major axis of an ellipse. The lower portion of figure 2 represents the geometrical idealization that we use to isolate some relations between stress–strain pattern and heterogeneity in fault orientation and crustal weakening. Structure to the south and to the northwest of the Transverse Ranges is similar to that assumed by Hill (1982). In our idealization the mechanical contribution of the western portion of the left lateral Garlock fault (G), the Big Pine (BP) fault and the Big Bend of the San Andreas might be considered as part of the east–west trending fault system.

3. Viability of a two-dimensional model

In this paper we shall attempt to draw some analogy between a two-dimensional model with heterogeneity in fault weakening and orientation with stress and deformation in the region of the Transverse Ranges in southern California. Certainly no two-dimensional theory is entirely adequate.

Ergas & Jackson (1981) have demonstrated that southern California and environs displays rather remarkable lateral homogeneity in crustal P-wave velocity considering the contrast in both lithology and metamorphic grade. This evidence and the regional Bouguer gravity might indicate that the Transverse Ranges have no deep roots (Oliver 1980; Walck & Minster 1982; Aki 1982). However, Humphreys *et al.* (1984) have shown that the mantle directly beneath the Transverse Ranges transmits compressional seismic waves nearly 3% faster than its surroundings. A convergent lithospheric flow that advects cold material into the region might be implied (Bird & Rosenstock 1984). The viscous stress or the negative buoyancy, or both, associated with the anomaly may have to be considered in any accurate forward model of stress in southern California. Density anomalies at depth may act to influence crustal stress patterns significantly (Fleitout & Froidevaux 1982).

Crustal thickness variations may play an important role in the Neogene (or *ca.* 10 Ma) timescale evolution of strain and stress in the interplate zone. Using a series of numerical viscous flow experiments, England & McKenzie (1982) have shown that the ratio of stress caused by crustal thickness contrast to stress associated with observed strain rate can be used as a measure of the relative importance of topography in determining lateral variations in deviatoric stress. England & McKenzie call this ratio the Argand number, Ar. The values of the maximum shear stress at 10 km depth are probably between 10 and 100 MPa in the North-American–Pacific interplate zone (McGarr 1980; Christie & Ord 1980; Lachenbruch & Sass 1980). The Transverse Ranges are uplifted by 1.5 km, so

$$Ar \approx 1.5 \text{ km} \quad \rho g/(\text{maximum shear stress estimate}).$$

Thus the use of $\rho = 2.8$ g cm^{-3} and $g = 10$ m s^{-2} gives: $0.35 \lesssim Ar \lesssim 3.50$. England & McKenzie's (1982) calculations with $Ar = O(1)$ for colliding sheets of power-law fluids show

that crustal thickness contrasts do have some influence upon the deformation field. However, they are not the dominant source of regional variation in deviatoric stress (as occurs, for example, when $Ar \gtrsim 10$). Thus for the Transverse Ranges and environs, crustal thickness variations may effect the overall stress distribution.

An additional source of difficulty in constructing a reliable model of stress variation in the interplate shear region of southern California is the potentially important influence of spatial irregularity in upper mantle drag (McGarr 1982; Bird & Baumgardner 1984). The three-dimensional effects mentioned above (density anomalies, crustal thickness variation and basal drag) are ignored in the models treated in §§8 and 9. The isolation of the distinct role played by two-dimensional faulting heterogeneity in an interplate shear therefore appears, but only at the expense of giving full treatment to stress models of the Transverse Ranges.

4. Anisotropic weakening and tutorial models

Constitutive equation development appropriate to the weakening induced by active geological faulting can generally take two courses: either (1) analysis of oriented cracks or joints (Singh 1973), or (2) mixture theory for oriented media (Walpole 1981). The latter is often called 'laminate theory' (Biot 1965). We shall entertain both courses of analysis. Our application of constitutive theory for an anisotropic elastic media to unidirectional fault weakening will reply upon: (1) a multiple component constitutive theory originally developed by Bruggeman (1937); (2) the model due to Delameter *et al.* (1975) of a plate that is weakened by a doubly periodic array of cracks capable of both mode I (compression) and mode II (shear) deformation; and (3) our finite-element treatment of a checkerboard array of cracks that are restricted to mode II (shear) deformation.

In §§5, 6 and 7 these anisotropic constitutive models will be introduced. In addition, a series of extremely simple models will be discussed. These simple models help to clarify how the various assumptions of the anisotropic theory induce directionality, or channelling, of crustal deformation and stress. The tutorial models presented in §§5, 6 and 7 are *not* models of tectonic phenomena *per se*. In §§8 and 9 we shall apply the anisotropic constitutive weakening theory to tectonic models of the Transverse Ranges and demonstrate that the stress channelling induced by fault orientation has broad implications for the long-term distribution of recoverable elastic work in the southern California region. Below we introduce the laminate theory, a model that is often used in the context of seismic wave propagation in a layered media (Backus 1962).

5. Three-dimensional laminate

The static mechanical properties of a periodically active fault site are probably well characterized by the properties associated with fault gouge and a matrix of cracked, or highly fractured, rock. The width of typical active faults at depth is unknown. However, it can be easily shown by using elastic constants typical of cracked laboratory rock samples (see Walsh & Grosenbaugh 1979) that a composite formed by adjacent layers of cracked and uncracked rock at depth gives rise to a negligible mechanical weakening and anisotropy of the crust if fault widths are limited to 2 km. On the other hand, if the weak component of the crust is characterized by the weakening limits of theoretically derived models of intensely cracked rock (see Budiansky & O'Connell 1976; Rice *et al.* 1978), or of stress–strain observations of gouge in the strain hardening creep range (Morrow *et al.* 1982), then the composite crust may become

PHILOSOPHICAL TRANSACTIONS OF THE ROYAL SOCIETY A MATHEMATICAL, PHYSICAL & ENGINEERING SCIENCES

both weak and very anisotropic. The elastic constants derived for intensely cracked rock may be appropriate to the pre-rupture state of a fault.

Finally in this section a simple parameter study of the deformation resulting from the shearing of a rhomboidal block is undertaken. The mechanical behaviour deviates significantly from what is predicted on the basis of an isotropic constitutive assumption. The effect of the weak components of the laminate is to channel stress and strain.

(*a*) *Bruggeman's oriented composite*

The three-dimensional laminate model is a constitutive equation system that describes the bulk behaviour of a composite mixture. Orientation and periodicity is assumed (see figure 3). This model does not rely upon variational bounds on composite moduli, as with unoriented multiple-component media. The exactness with which continuity conditions may be applied to adjoining components allows for the development of more accurate and reliable constitutive relations than is typical of mixture laws for unoriented substances (Walpole 1981). The laminate model given below was first derived by Bruggeman (1937) and has also been treated by Helbig (1957) and Biot (1965). We therefore only state the results, noting that

$$a' = a/d, \quad b' = b/d$$

and dropping the primes below (see figure 3):

$$c_{11} = c_{\mathrm{I}}^{(1)}\, c_{\mathrm{I}}^{(2)}/B^*, \tag{1a}$$

$$c_{22} = c_{33} = (a^2+b^2)\, c_{11} + (ab/B^*)\,[(c_{\mathrm{I}}^{(1)})^2 + c(c_{\mathrm{I}}^{(2)})^2 - (\lambda^{(1)}-\lambda^{(2)})^2], \tag{1b}$$

$$c_{12} = c_{13} = [\lambda^{(1)}\lambda^{(2)} + 2(a\mu^{(2)}\lambda^{(1)} + b\mu^{(1)}\lambda^{(2)})]/B^*, \tag{1c}$$

$$c_{23} = [\lambda^{(1)}\lambda^{(2)} + 2(a\lambda^{(1)} + b\lambda^{(2)})\,(a\mu^{(2)} + b\mu^{(1)})]/B^*, \tag{1d}$$

$$c_{44} = a\mu^{(1)} + b\mu^{(2)} = \tfrac{1}{2}(c_{22} - c_{23}), \tag{1e}$$

$$c_{55} = c_{66} = \mu^{(1)}\mu^{(2)}/(a\mu^{(2)} + b\mu^{(1)}), \tag{1f}$$

where

$$B^* \equiv ac_{\mathrm{I}}^{(2)} + bc_{\mathrm{I}}^{(1)}$$

and

$$c_{\mathrm{I}}^{(1)} \equiv \lambda^{(1)} + 2\mu^{(1)}, \quad c_{\mathrm{I}}^{(2)} = \lambda^{(2)} + 2\mu^{(2)}.$$

In (1), λ and μ represent the isotropic Lamé constants of the faulted (superscript 1) and unfaulted (superscript 2) components (see figure 3*b*). The composite stiffnesses are the five independent constants c_{11}, c_{22}, c_{12}, c_{23} and c_{66}, and they determine the balance between stress, τ_{rs}, and strain, ϵ^{ij}. The constitutive equation is

$$\tau_{11} = c_{11}\,\epsilon_{11} + c_{12}\,\epsilon_{22} + c_{12}\,\epsilon_{33}, \tag{2a}$$

$$\tau_{22} = c_{12}\,\epsilon_{11} + c_{22}\,\epsilon_{22} + c_{23}\,\epsilon_{33}, \tag{2b}$$

$$\tau_{33} = c_{12}\,\epsilon_{11} + c_{23}\,\epsilon_{22} + c_{22}\,\epsilon_{33}, \tag{2c}$$

$$\tau_{23} = \tfrac{1}{2}(c_{22} - c_{23})\,\epsilon_{23}, \tag{2d}$$

$$\tau_{13} = c_{66}\,\epsilon_{13}, \tag{2e}$$

$$\tau_{12} = c_{66}\,\epsilon_{12}. \tag{2f}$$

PHILOSOPHICAL TRANSACTIONS OF THE ROYAL SOCIETY A MATHEMATICAL, PHYSICAL & ENGINEERING SCIENCES

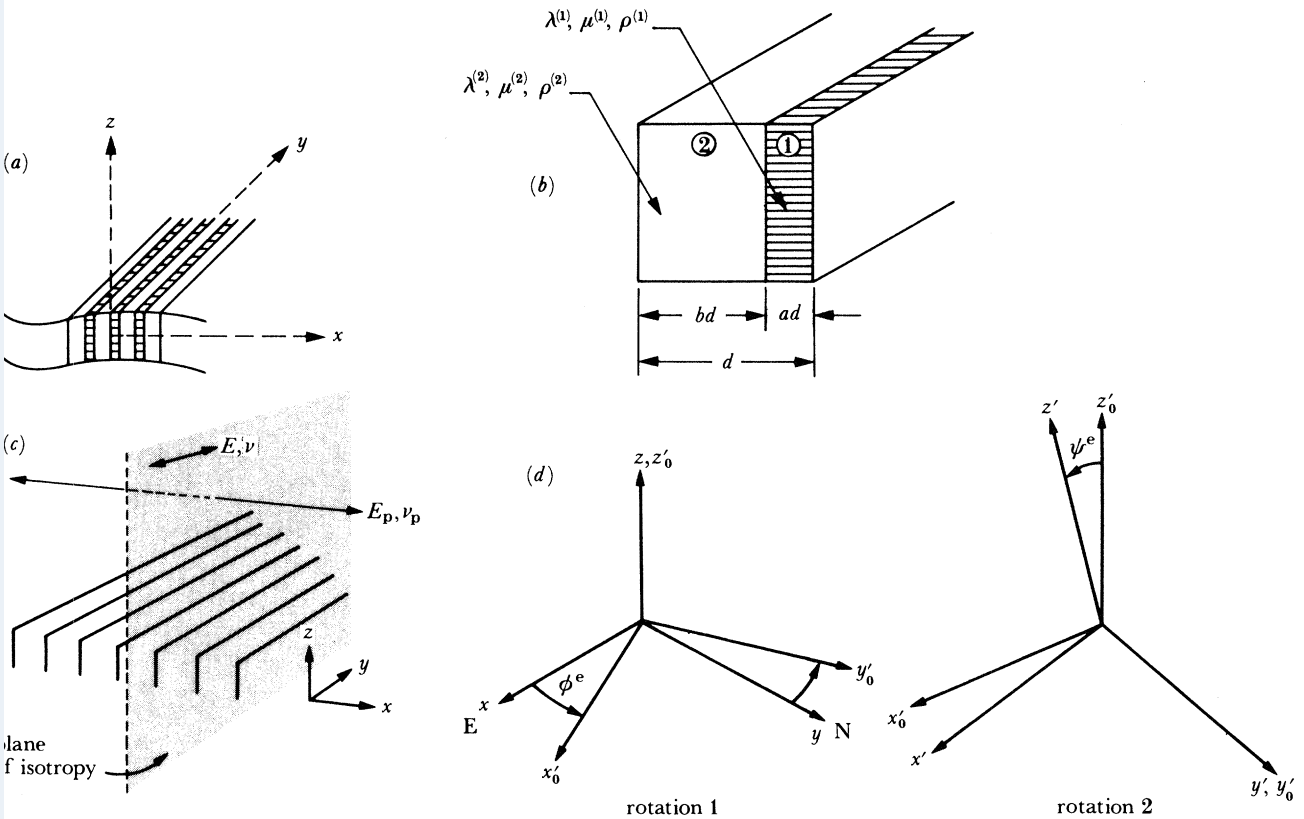

FIGURE 3. Three-dimensional, two-component laminate model: (*a*) coordinates of the laminate; (*b*) faulted (1) and unfaulted (2) phases; (*c*) interpretation of moduli E, E_p, ν and ν_p in terms of crustal fault orientation; (*d*) counter-clockwise rotations from coordinates of transverse isotropy (x, y, z) to attitude of fault plane ($y'-z'$), yielding the inverse of the rotation matrix given by Rose (1957) (see equation (4) in text). (E and E_p are the Young moduli for tension or compression in the plane of isotropy and normal to the plane; respectively; dip $= 90°-\psi^e$; strike $= \phi^e$.)

We assume a definition for ϵ^{ij} such that

$$\epsilon^{ij}\,\delta^{ij} = (\partial^i u^j + \partial^i u^j), \tag{3a}$$

$$\epsilon^{ij}(1-\delta^{ij}) = \tfrac{1}{2}(\partial^i u^j + \partial^j u^i), \tag{3b}$$

where δ^{ij} is the Kronecker delta and $\partial^i u^i$ is the displacement gradient tensor with $\partial^i \equiv \partial/\partial x^i$. Forms (3*a*) and (3*b*) for ϵ^{ij} yield a set of five anisotropic constants identical to those of Lekhnitskii (1981) and Green & Taylor (1939).

Equations (1) assume an x-axis of rotational symmetry as shown in figure 3*b*. Table 2 gives the corresponding component ensemble of the compliance tensor A^{ijrs} with directional moduli E, E_p, ν, ν_p, G and G_p. The inequalities shown in table 2 must be obeyed if the composite moduli represent a real material since they are conditions for positive definiteness of the strain energy (Eubanks & Sternberg 1954; Backus 1962).

When the plate shown in figure 3*a* is aligned with the axes of mechanical symmetry parallel to (x, y, z) as shown, then the Young moduli, E and E_p, and Poisson ratios, ν and ν_p, can be interpreted with the directionality indicated (also see table 2).

Figure 4 shows the moduli E, E_p, G and the corresponding stiffnesses c_{11}, c_{22}, c_{12} and c_{66} as

TABLE 2

anisotropic media

$$\bar{C}^{klmn} = \frac{\partial \bar{x}_k}{\partial x_i}\frac{\partial \bar{x}_l}{\partial x_j}\frac{\partial \bar{x}_m}{\partial x_r}\frac{\partial \bar{x}_n}{\partial x_s} C^{ijrs} \tag{T 1}$$

$$e^{ij} = A^{ijrs}\tau_{rs} \tag{T 2}$$

transversely isotropic (x-axis symmetry)

$$A^{ijrs} \rightarrow \begin{bmatrix} a_{11} & a_{12} & a_{12} & 0 & 0 & 0 \\ a_{12} & a_{22} & a_{23} & 0 & 0 & 0 \\ a_{12} & a_{23} & a_{22} & 0 & 0 & 0 \\ — & — & — & 2(a_{22}-a_{23}) & 0 & 0 \\ — & — & — & — & a_{66} & 0 \\ — & — & — & — & — & a_{66} \end{bmatrix}$$

$$= \begin{bmatrix} \frac{1}{E_p} & -\frac{\nu_p}{E_p} & -\frac{\nu_p}{E_p} & 0 & 0 & 0 \\ -\frac{\nu_p}{E_p} & \frac{1}{E} & -\frac{\nu}{E} & 0 & 0 & 0 \\ -\frac{\nu_p}{E_p} & -\frac{\nu}{E} & \frac{1}{E} & 0 & 0 & 0 \\ — & — & — & \frac{2(1+\nu_p)}{E_p} & 0 & 0 \\ — & — & — & — & \frac{1}{G} & 0 \\ — & — & — & — & — & \frac{1}{G} \end{bmatrix} \tag{T 3}$$

strain energy positive definite

$$G > 0,\ E > 0,\ E_p > 0,\ 1-\nu > 2E\nu_p^2/E_p,\ \nu > -1$$

a function of increasing proportion (a/b) of the weak component. The three cases I, II and III corresponding to the moduli shown in table 3. These cases shown in figure 4 can be split into two groups depending upon the ratios $\mu^{(1)}/\mu^{(2)}$ and $K^{(1)}/K^{(2)}$ assumed for the two laminate components. $K^{(1)}$ and $K^{(2)}$ are the bulk compressibilities for weak and strong components, respectively. When $\mu^{(1)}/\mu^{(2)} \ll 1$, but $K^{(1)}/K^{(2)} \approx 1$, then the static mechanical response to horizontal $(x-y)$ shearing applied to the aligned plate shown in figure 3*a* is a directional enhancement, or channelling, of shear strain, ϵ_{12}, relative to the isotropic case. We refer to this case as shear, or strike-slip, dominated since the composite plate's response is qualitatively similar to strike-slip faulting. This case is characterized by a low value of the composite shear modulus, G. In figure 4*a*, G drops by almost two orders of magnitude even for $(a/b) \approx 0.2$. In the case shown in figure 4*a* c_{12} remains constant with respect to variations in (a/b) because we have set $\lambda^{(1)}/\lambda^{(2)} = 1$.

Consider now G_0 to be the typical rigidity of competent crustal material. It is instructive to examine (1*f*) with $\mu^{(2)} \approx G_0$ and $a/b \ll \mu^{(1)}/G_0$. In this case Biot's (1965) slide modulus, $L \equiv G/G_0$, is

$$L \approx 1/b = O(1),$$

and hence we may expect that the laminate model must assume that faults are fairly wide at depth if they effectively weaken the crust. Though fault zones may widen with depth it is probably safe to assume that

$$O(10^{-4}) \lesssim a/b \lesssim O(10^{-1}).$$

PHILOSOPHICAL TRANSACTIONS OF THE ROYAL SOCIETY A MATHEMATICAL, PHYSICAL & ENGINEERING SCIENCES

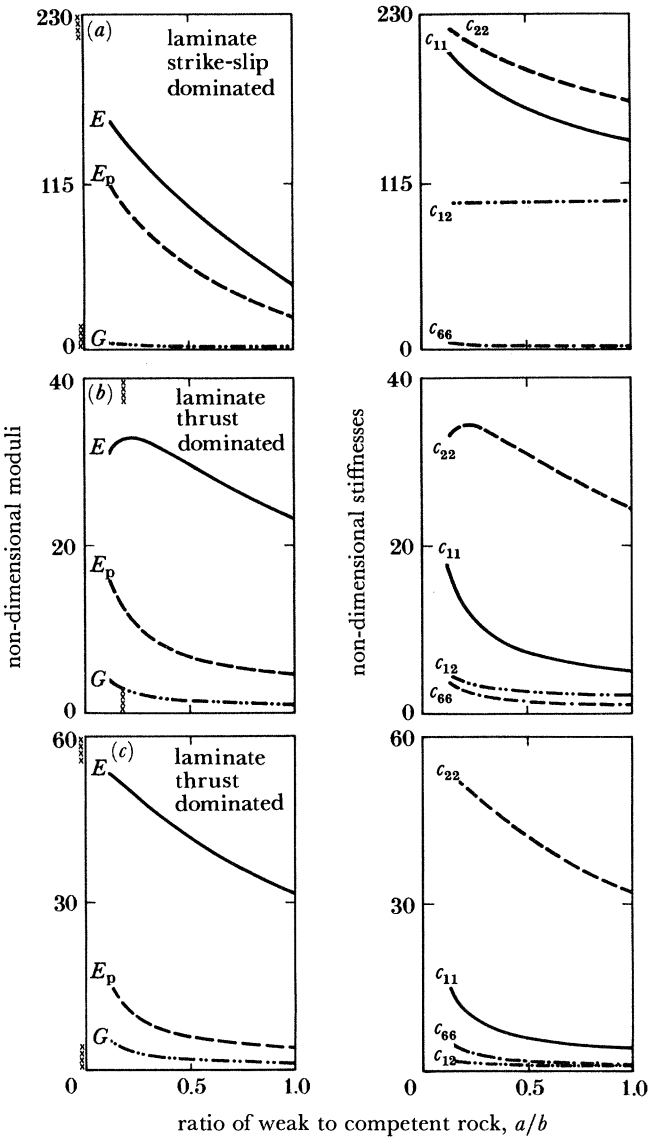

FIGURE 4. Values of E, E_p, and shear modulus G and the corresponding stiffness as a function of increasing proportion of weak rock phase. Any value shown to the left of the four vertical ×'s at the top and bottom violate the condition of positive definite strain energy. Cases I, II and III of table 3 correspond to (*a*), (*b*) and (*c*), respectively.

Hence the weakening range $L = O(10^{-1})$ occurs in the laminate model when a/b and $\mu^{(1)}/G_0$ are of similar order if the rigidity of the weak component is to be connected to the theoretical weakening limits of cracked rock. Model calculations by Budiansky & O'Connel (1976) (see their figure 8 for example) of the weakening caused by partly saturated circular cracks indicate that $\mu^{(1)}/G_0 \approx 0.2$–$0.1$ when volumetric crack densities are between 0.5 and 0.75. Such a strong decrease in effective shear modulus occurs in the strain-hardening creep range when fault gouge is sheared in the laboratory under confining pressures of 200 MPa. Morrow *et al.* (1982) have recently performed laboratory experiments in which the effective shear modulus drops to the range one tenth to one fiftieth of their low strain elastic values before brittle failure (see their figure 10 for example). $L = O(10^{-1})$ is therefore not an unreasonable expectation for faults

whose mechanical properties correspond to the strain softening, or pre-rupture, state of a fault. No cogent argument can be made that active faults can be characterized in this way for more than a relatively short span of their temporal histories. Evidence that overall regional tectonic stress is characterized by the sliding frictional strength of fractured rock (see, for example, Byerlee 1978; Zoback & Zoback 1980*a*; Hill 1982) suggests, however, that a characterization of the static stress field with the theoretical weakening limit $L = O(10^{-1}$ to $10^{-2})$ may be of some value in predicting stress patterns from observed fault orientation. In a later section we develop elastic constitutive relations for a model that characterizes the weakening of faults by a two-dimensional array of cracks.

If the adjacent components in the laminate model are characterized by $\mu^{(1)}/\mu^{(2)} \approx K^{(1)}/K^{(2)} \ll 1$, then the mechanical response to applied horizontal shearing will be characterized by both enhanced shear and compressional straining. We refer to this limit as compression, or thrust, dominated (see figure 4*b*, *c*). An enhanced compressional strain is analogous to tectonic straining, or crustal shortening, associated with thrusting or folding. This limit is useful in simulating the combined effects of local crustal stress–strain channelling and low-stress–high-strain. The maximum estimates of crustal shortening due to thrusting are around 1.66:1 (Scheidegger 1956) and consequently involve strains entirely unmodelable within the confines of linear elastic constitutive assumptions. However, the sense of straining response is an analogue to thrusting behaviour. Below, a model of strain channelling along thrusting planes allows us to determine when effective anisotropy may become a significant feature in crustal deformation.

TABLE 3. SCALE FACTORS AND PARAMETERS OF SEPARATE PHASES FOR LAMINATE MODEL RESULTS SHOWN IN FIGURE 4

case no.	scale factor / MPa	$\nu^{(1)}$	$\nu^{(2)}$	$\mu^{(1)}$	$\mu^{(2)}$	$E^{(1)}$	$E^{(2)}$	$K^{(1)}$	$K^{(2)}$
I	3.32×10^2	0.498	0.299	1.67×10^2	2.25×10^4	5.01×10^2	5.83×10^4	3.35×10^4	4.83×10^4
II	2.06×10^3	0.380	0.194	1.05×10^3	4.3×10^4	2.90×10^3	1.0×10^5	3.28×10^3	6.12×10^4
III	4.09×10^3	0.280	0.094	2.92×10^3	1.31×10^5	6.7×10^3	2.6×10^5	5.09×10^3	1.06×10^5

Crustal zones where pervasive faulting occurs are probably best characterized by a low stiffness c_{66}, or shear-dominated, case (figure 4*a*) and not by the compressional case (figure 4*b*, *c*). Values of the bulk shear modulus c_{66} that represent a significantly weakened crust should enable strong stress and strain channelling to occur along the directions of multiple parallel fault planes. A weak strike-slip fault corresponds to a region of low shear modulus (or, equivalently, low c_{66}, high a_{66}). Biot (1965) refers to this as a case of low slide modulus L. An additional non-dimensional parameter will be useful in the discussion. We define a weakening parameter Λ such that

$$\Lambda \equiv 1 - L.$$

As $\Lambda \to 0$ isotropy is recovered and as $\Lambda \to 1$ the limit of extreme weakening, anisotropy and stress–strain channelling is approached.

Often thrust faulting is thought to be associated with compressional forces acting at a distance. Rundle & Thatcher's (1980) three-dimensional model of a high-angled dislocation has clearly demonstrated that this is not always so. A multiple, parallel faulting anisotropy can

also demonstrate how fault planes actually channel stress–strain from a horizontal $(x-y)$ shear stress acting at a distance. The channelling can generate significant z–x and z–y shear straining. The parallel fault plane attitude of the crustal inhomogeneity shown in figure 5*a* deviates from that of the surrounding crust. If x–y shearing were applied to the plate boundary shown in figure 5*a*, how might we quantify the thrusting response of the crustal heterogeneity in terms of the reduced composite shear modulus G and weakening parameter?

We approximate the heterogeneity as a rectangular rhomboidal element and then examine the deformational response of the section due to x–y pure shear. If the forces applied on the heterogeneity are pure shearing and the displacements at its interface are unrestricted then the solution of this problem is trivial. The solution simply involves the constitutive equation (see table 2 and equations (1), (2) and (3)). This problem has been given analytical treatment by Lekhnitskii (1981, p. 83). The lack of displacement boundary conditions implies that solutions should be treated as a *qualitative* description of thrust–fault induced vertical strain and uplift. The case, however, illustrates the important roles that both geometry and the weakening parameter Λ are to play in models of crustal anisotropy.

(*b*) *Treatment of strike and dip*

The vertical plane of isotropy of the heterogeneity shown in figure 5 is not perpendicular to the x–y plane. Consequently, the full stiffness matrix, (with all 36 non-zero elements) $\bar{C}^{klmn}$ (see table 2) must be considered in the coordinate frame (x, y, z). The relation between coordinates of the material aelotropy (primed in figure 5) and the coordinates of the applied $(x$–$y)$ shear stress is defined by the direction cosines, $\partial x_k/\partial x_i$ (see table 2). Representation of the fourth-rank tensor C^{ijrs} in an arbitrarily rotated, non-translated frame (thus obtaining $\bar{C}^{klmn}$) requires operating upon C^{ijrs} with the series of four transformation matrices $\partial \bar{x}_k/\partial x_i$ (see first equation in table 2). We can construct the rotation matrix in terms of observed fault attitude angles, ϕ^{e} (strike) and ψ^{e} $(90°-\mathrm{dip})$. The consecutive rotations through ϕ^{e} and ψ^{e} (see figure 3*d*) determine the components of the second-rank tensor $\partial \bar{x}_k/\partial x_i$. The components of the rotation matrix are then identical to the inverse of the matrix given by Rose (1957). Note that only two rotations are necessary to define the dip and strike. The dyadic matrix form of the rotation tensor is

$$\partial \bar{x}_k/\partial x_i = \begin{bmatrix} \cos\phi^{\mathrm{e}}\cos\psi^{\mathrm{e}}\,\hat{\imath}\hat{\imath} & -\sin\phi^{\mathrm{e}}\cos\psi^{\mathrm{e}}\,\hat{\imath}\hat{\jmath} & \sin\psi^{\mathrm{e}}\,\hat{\imath}\hat{k} \\ \sin\phi^{\mathrm{e}}\,\hat{\jmath}\hat{\imath} & \cos\phi^{\mathrm{e}}\,\hat{\jmath}\hat{\jmath} & 0 \\ -\cos\phi^{\mathrm{e}}\sin\psi^{\mathrm{e}}\,\hat{k}\hat{\imath} & \sin\phi^{\mathrm{e}}\sin\psi^{\mathrm{e}}\,\hat{k}\hat{\jmath} & \cos\psi^{\mathrm{e}}\,\hat{k}\hat{k} \end{bmatrix}. \tag{4}$$

The tensor $\partial \bar{x}_k/\partial x_i \cdot \partial \bar{x}_l/\partial x_j \cdot \partial \bar{x}_m/\partial x_r \cdot \partial \bar{x}_n/\partial x_s$ is a lengthy expression, and Lekhnitskii (1981, p. 42) has given a complete table of the components of this product. Application of this product on the compliance tensor A^{ijrs} yielding $\bar{A}^{klmn}$ renders all the zero terms in the matrix shown in table 2 finite.

(*c*) *Non-aligned segment in horizontal shear*

If horizontal $(x$–$y)$ shearing stress is τ_{sh}, then the y–z component of strain far from the boundary is

$$\epsilon_{23} = a_{46}\,\tau_{\mathrm{sh}} \tag{5}$$

(see Lekhnitskii 1981, p. 85). Implicitly assumed is that ϵ_{23} is measured in a frame corresponding to the frame shown by the dotted lines in figure 5*a*.

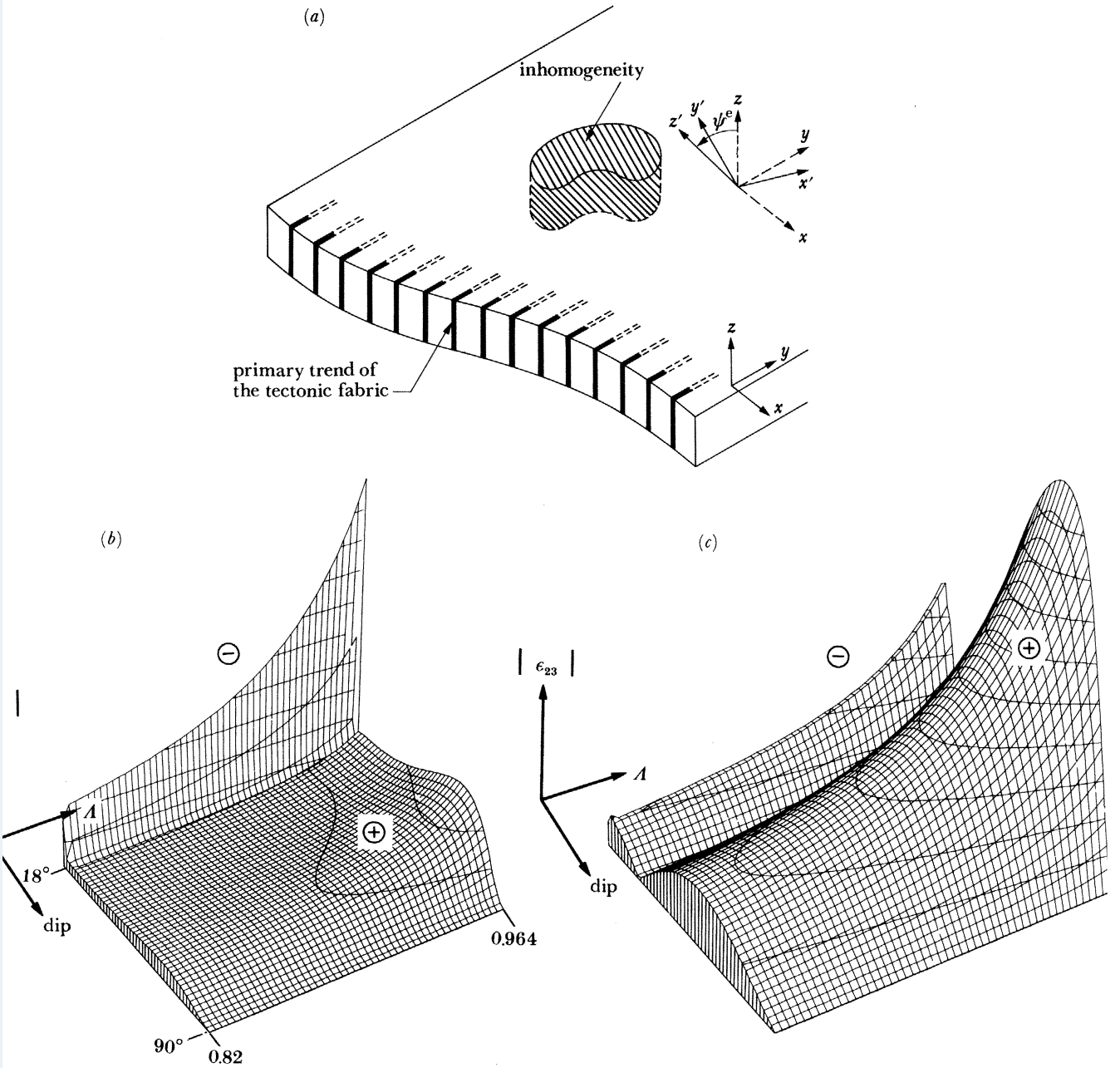

FIGURE 5. Horizontally sheared crustal inhomogeneity (*a*) and measures of anisotropically induced distortions for differing fault plane attitudes (*b*, strike = 15°; *c*, strike = 60°). Fault plane attitude of the inhomogeneity corresponds to (x', y', z') and applied shearing is in the $(x-y)$ plane (*a*). For (*b*) and (*c*) $1-G/G_0 = \Lambda$. See (5) for strain ϵ_{yz}. The vertical contours are (*b*) 820μ and (*c*) 940μ strain for $\tau_{sh} = 10$ MPa and bulk laminate compliances; $a_{11} = 2.66 \times 10^{-5}$, $a_{22} = 1.93 \times 10^{-5}$, $a_{23} = 5.58 \times 10^{-6}$, $a_{12} = -5.59 \times 10^{-6}$, $a_{44} = 1.39 \times 10^{-5}$ MPa^{-1} in the primed frame.

The vertical component of displacement is a linear function of a_{16} and a_{46}. If the rhomboidal heterogeneity is much wider than its depth, then the linear dependence of vertical displacement upon a_{46} dominates. The compliance a_{46} is a complicated function of the angles ϕ^e (strike) and ψ^e (90° − dip) and the transversely isotropic compliances. Rather than writing out the full expression for a_{46} we show the dip, strike, and dependence upon Λ of the strain component

ϵ_{23} in figure 5*b*, *c*. The contours of vertical displacement are nearly identical to those shown in figure 5*b*, *c* for a thin flat heterogeneity. The non-linearity of $|\epsilon_{23}|$ against Λ in the range $0.82 \leqslant \Lambda \leqslant 0.964$ displayed in figure 5*b*, *c* shows where shear weakening significantly begins to influence the crust mechanically. There is an interplay of fault attitude and weakening parameter Λ. The three-dimensional diagrams shown in figure 5 demonstrate that the net deformational channelling with oriented crust will depend upon both strike and dip.

6. Stress channelling

The simple three-dimensional results discussed above reveal that when $\Lambda \approx 0.9$ the influence of the *directionality* of the multiple fault planes is non-negligible. Let us now examine the case of a plate of infinite lateral extent that experiences an in-plane stress applied at the origin. The plate is assumed to be governed by the equations of generalized plane stress.

Figure 6 shows contours of the radial stress distributions for an in-plane stress directed both along, and orthogonal to, the fault orientation. The results shown in the three cases correspond to (1) weakening due to cracks (discussed in the next section), (2) moduli from the strike-slip-dominated laminate of figure 4*a*, and (3) from the compression-dominated laminate of figure 4*c*. The three cases correspond to figure 6*a*, *b* and *c*, respectively. All three cases assume values of *ca.* 0.9 for the weakening parameter Λ.

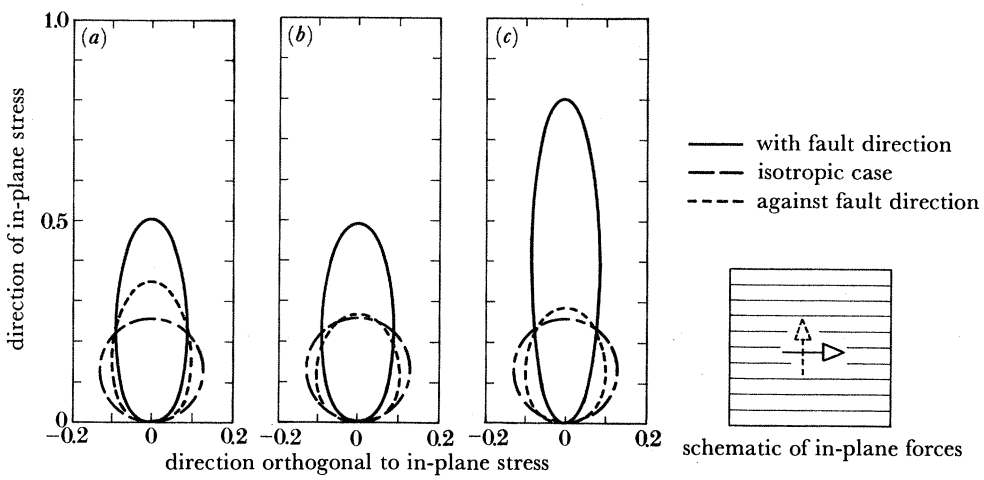

Figure 6. Radial stress channelling for three cases of crustal anisotropy. Lines show contours of constant values of $\tau_{rr}\ (x^2+y^2)^{\frac{1}{2}}$. The point force in-plane stress is at the origin. The crack model corresponds to the first pair shown in figure 9*d* with an asperity density of 65% (*a*). Diagram (*b*) corresponds to the laminate model shown in figure 4*a* with ratio $a/b = 0.19$. Diagram (*c*) corresponds to the laminate model with thrust domination (large contrast between E and E_p) in figure 4*c* ratio $a/b = 0.19$. Note the deepest penetration (*c*) occurs for large contrast in directional Young modulus (i.e. when E_p/E is small). Crack model and strike-slip dominated laminate model similar penetration depths (i.e. compare (*a*) and (*b*)). The analytical expression for the radial stress component, τ_{rr}, when both the faults and in-plane stress, P, are directed in the y direction is

$$P \sum_{n=1}^{2} x\chi_n/[2\pi(\beta_1^*-\beta_2^*)\, a_{22}(x^2+y^2)^{\frac{1}{2}}],$$

where

$$\chi_n \equiv (-1)^n \beta_n^{*-\frac{1}{2}}(a_{12}-\beta_n^* a_{22})\,[(3\beta_n^*-1)-C_n]/(\beta_n^*+1+C_n)$$

and

$$C_n \equiv (\beta_n^*-1)\,[1-2x^2/(x^2+y^2)],$$

and the roots β_2^* and β_1^* are $\frac{1}{2}[f_a+(a_{66}+2a_{12})/a_{22}]$ and $a_{11}/(\beta_2^* a_{22})$, respectively, with $f_a \equiv \{[(a_{66}+2a_{12})/a_{22}]^2-4a_{11}/a_{22}\}^{\frac{1}{2}}$. For in-plane stress directed normal to faulting direction, the same expression applies only with compliances that result when operating with the transformation matrix with $\phi^e = 90°$. (See Green & Taylor (1939).)

Note the similarity in radial stress penetration depth for strike-slip-dominated and crack result, relative to the isotropic case. The compression-dominated laminate (figure 6*c*) shows the strongest penetration, or channelling, because the radial stress is a stronger function of the ratio E/E_p than of other directional moduli ratios.

The similarity between radial stress channelling in crack and laminate models suggests a link between the constitutive effects. The two models, based upon vastly different assumptions about the basic physics, are likely to yield similar overall stress and strain reliefs. Let us now examine the crack model in more detail. In a later section we shall examine further the question of the similarity in stress patterns among laminate and crack anisotropies.

7. Collinear cracks

When the weakening parameter $\Lambda = 0.9$ then anisotropy must play a significant role constitutively. An explicit connection between realistic faulted-rock parameters and a value of Λ that is in the weakened range, however, has not yet been given. The three-dimensional laminate model has served only to demonstrate the importance of the details of multiple oriented fault plane attitude. In this section we argue that the crust may, in fact, weaken with $\Lambda \approx 0.9$. The plausibility of this weakening is demonstrated by considering the effect of collinear sets of cracks in static deformation.

The three-dimensional heterogeneity of single faults may occur owing to irregularities in geometry, stress or mechanical property. The heterogeneity in earthquake rupture as constrained by synthetic seismogram modelling indicate that the breaking of relatively small (diameter *ca.* 1–10 km) fault asperities may account for a considerable portion of the total seismic moment (Aki 1979). Whether or not these coseismic anomalies are indicative of asperities that control the locking of a fault during the interseismic period is unknown. If such asperities along a fault occur because of geological controls such as local contortion of the fault surface or because of local differences in basement rock across the fault trace, then these features also act as barriers to static elastic straining. Furthermore, where superficial features disappear along a linear fault trace and then reappear several or tens of kilometres further down the trace, it is probable that little or no brittle deformation occurs in the uppermost portion of the crust and that the fault is elastically locked within that region. Such areas and seismic gaps (regions where linear trends in seismicity are abruptly truncated by a so-called locked region) qualify as effective asperities under the loose definition we now adopt.

(*a*) *Doubly periodic array*

In figure 7*a* an idealized plate is shown that is weakened by a doubly periodic array of cracks. Here the elastically locked portions of the strike-slip faults correspond to static elastic barriers (asperities). Since the plate is idealized with the doubly periodic array, interspacing parameters, β, δ and crack length, 2α, can be related to the weakening of a crustal plate. We interpret these as representative of the average locked and unlocked distributions of a particular crustal-tectonic province characterized by multiple, oriented faults. Unfortunately, we do not have strong observational controls on δ, the distance between neighbouring collinear unlocked segments. The distance along a locked portion of a fault ($\delta - 2\alpha$) may be quite large if those areas are analogous to seismic gaps. Sanders & Kanamori (1984) suggest 22 km for the Anza seismic

gap in the San Jacinto fault zone. On the other hand, if the locked portion is similar to asperity dimensions estimated from seismic sources of earthquakes then the percentage of a fault that is locked may be quite small (2%), according to an analysis by Rudnicki & Kanamori (1981). Hartzell & Brune (1979) suggest a double-asperity source dimension of about 0.5–1.0 km for an earthquake of moderate magnitude in the San Jacinto fault system. Source models for earthquakes in the western Transverse Ranges and of other earthquakes in the San Jacinto fault system suggest similar asperity length scales (see, for example, Wallace *et al.* (1981) and Ebel & Helmberger (1982), respectively).

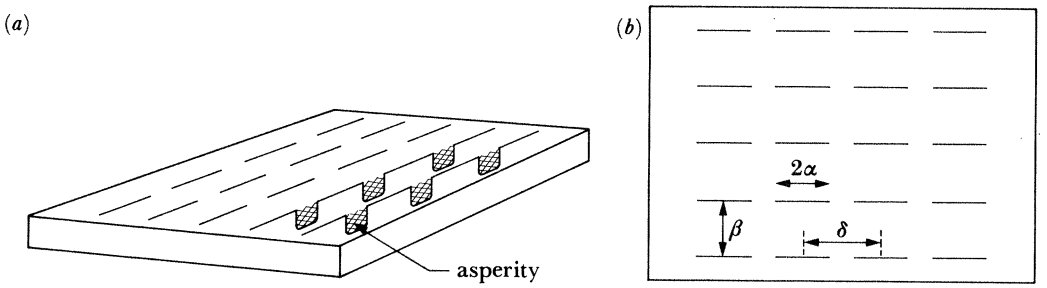

FIGURE 7. Geometrical diagram of cracked plate in terms of N strike-slip faults with N_c asperities (a) and interspacing dimensions of doubly periodic crack array from bird's-eye-view (b). This interspacing corresponds to the model proposed by Delameter *et al.* (1975), which allows both mode I and mode II deformation.

Delameter *et al.* (1975) analysed the mechanical weakening associated with the doubly periodic crack array shown in figure 7. Delameter's model allowed stress field interaction for both mode I and mode II deformation (see Bilby & Eshelby 1968, p. 116). The numerically determined first-order stress-intensity coefficients B_1^{I} and B_1^{II}, associated with those deformation modes (i.e. corresponding to tensional and shearing responses, respectively) are related to the parameters of a planar orthotropic elastic material (see figure 3c and table 2):

$$E_{\mathrm{p}}/E = \nu_{\mathrm{p}}/\nu = 1/(1+2\pi\alpha^2 B_1^{\mathrm{I}}/\beta\delta), \tag{6a}$$

$$\Lambda = (2\pi\alpha^2 B_1^{\mathrm{II}} G_0/\beta\delta E_0)/(1+2\pi\alpha^2 B_1^{\mathrm{II}} G_0/\beta\delta E_0), \tag{6b}$$

where G_0 and E_0 are the isotropic values of the shear modulus and Young modulus, and α, β and δ are interspacing parameters shown in figure 7b. A schematic representation of the numerically determined values of B_1^{I} and B_1^{II} given by Delameter *et al.* (1975) as a function of the interspacing ratios $\delta/2\alpha$ and $\beta/2\alpha$ is shown in figure 8. On the basis of these results notice that when collinear interspacing is close ($\delta/2\alpha \to 1$) relative to adjacent collinear line interspacing ($\beta/2\alpha \to 1$) then the ratio of the coefficients of stress intensity, $B_1^{\mathrm{II}}/B_1^{\mathrm{I}}$, is roughly 2–4. Weakening due to mode I deformation becomes dominant only when adjacent linear features become increasingly close together and $\beta/\delta \ll 1$. Since adjacent faults are spaced relatively far from one another, we are interested in the cases where $\beta/\delta \gtrsim 1$, and mode II dominates the weakening.

In figure 9 we have plotted the effect of fault weakening in terms of the stiffnesses c_{11}, c_{22}, c_{12} and c_{66} and the cross-structure Young modulus E_{p} as a function of decreasing linear asperity percentage or, in effect, decreasing locked portion. However, in each individual case we decrease the interspacing ratio $\delta/2\alpha$ to affect changes in the collinear asperity percentage. In

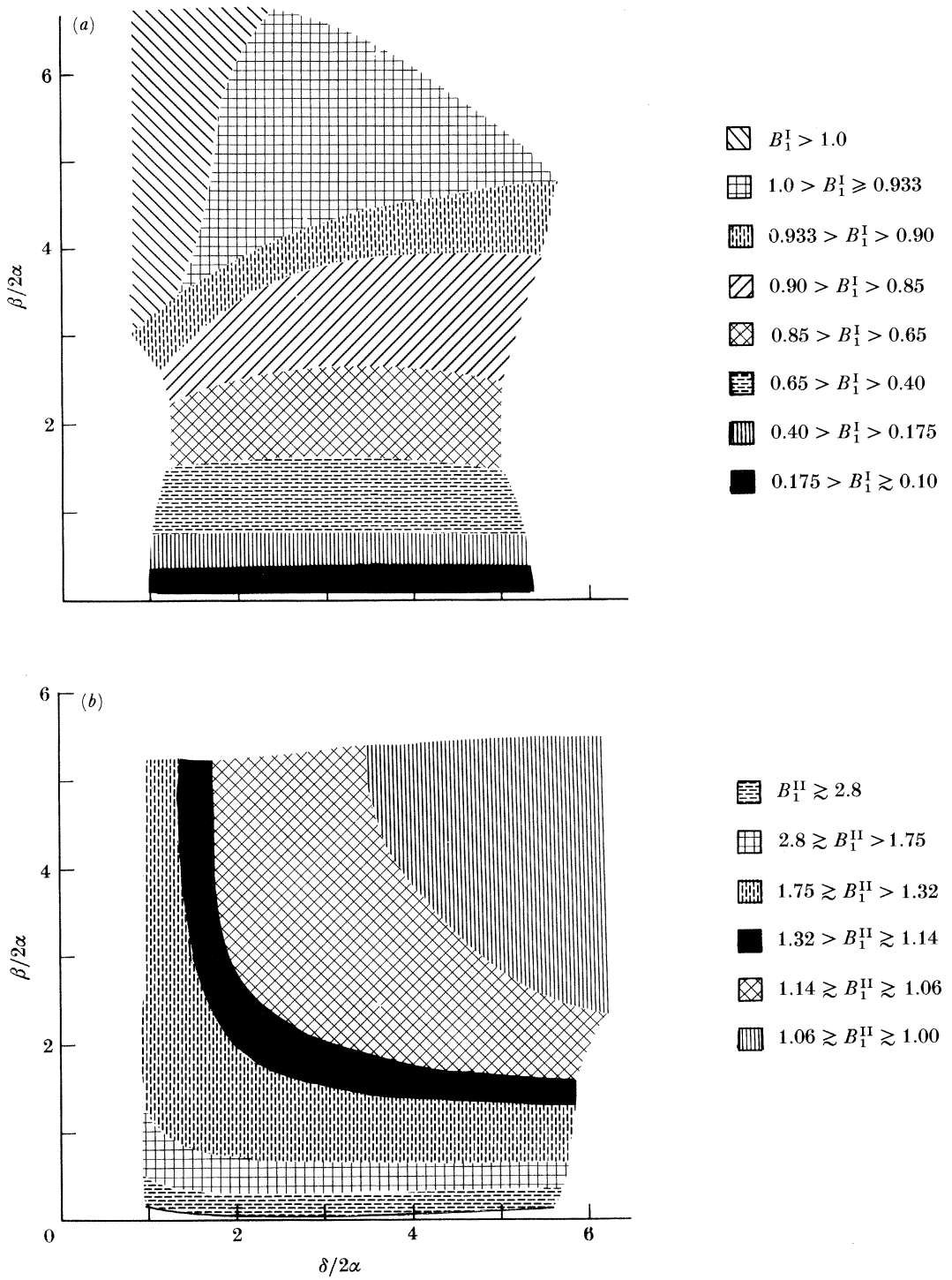

FIGURE 8. Schematic diagram of stress intensity coefficients B_1^{I} and B_1^{II}, as a function of crack interspacing parameters $\beta/2\alpha$ and $\delta/2\alpha$. Values have been interpolated from a table of numerical values calculated by Delameter *et al.* (1975). Large B_1^{I} (mode I) and B_1^{II} (mode II) cause directional weakening associated with E_{p} and G (or Λ), respectively.

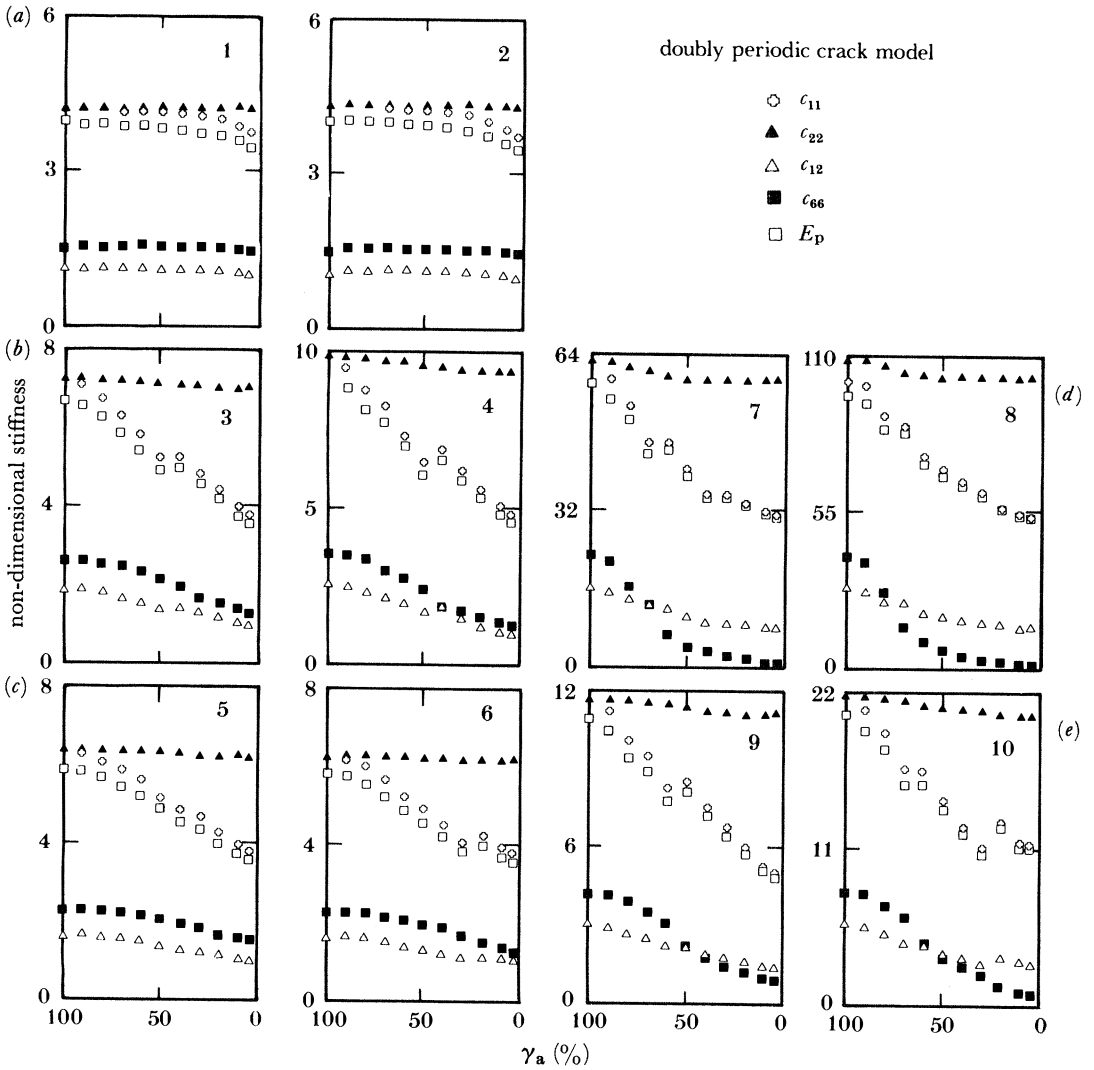

FIGURE 9. Ten cases of differing interspacing. A decrease in moduli and stiffnesses occurs with decreasing asperity density along strike-slip faults. Cases numbered 1–10 correspond to the sets of parameters given in table 4. Note that the decrease in asperity density marginally weakens the plate in case (*a*). For all cases 100% asperity corresponds to isotropic values $E_p = E = 9.07 \times 10^4$, $c_{22} = c_{11} = 9.77 \times 10^4$, $c_{12} = 2.61 \times 10^4$, $c_{66} = 3.58 \times 10^4$ MPa.

all five pairs of cases shown in figure 9 we can relate the spatial parameters of a rectangular crustal section of total area extent A in the following way:

$$A = H_c H = \beta N \delta N_c, \tag{7a}$$

$$N = H/\beta, \tag{7b}$$

$$N_c = A/N\delta\beta, \tag{7c}$$

$$A_d = N_c N/A = (\delta\beta)^{-1}, \tag{7d}$$

$$\gamma_a = 100(1 - 2\alpha/\delta). \tag{7e}$$

PHILOSOPHICAL TRANSACTIONS OF THE ROYAL SOCIETY A MATHEMATICAL, PHYSICAL & ENGINEERING SCIENCES

TABLE 4. INTERSPACING PARAMETERS CORRESPONDING TO FIGURE 9

(See equations (7) in text.)

collinear asperity density, $\gamma_a = 50\,\%$

case no.	N_c	N	δ/km	β/km	α/km	scale at $\gamma_a = 100\,\%$ (10^5 MPa)	A / 10^4 km^2
1	110	4	2.0	55.0	0.5	2.29	4.84
2	165	8	1.3	27.5	0.4	2.29	4.84
3	5	6	28.3	23.6	7.0	1.34	2.0
4	5	12	28.3	11.8	7.0	0.99	2.0
5	10	6	14.2	23.6	3.5	1.55	2.0
6	13	12	10.3	11.8	2.6	1.55	2.0
7	1	4	443.0	55.0	110.8	0.15	4.84
8	1	8	295.6	27.5	73.9	0.09	4.84
9	2	6	250.0	83.3	62.5	0.84	25.0
10	3	12	166.7	41.7	41.7	0.45	25.0

Here H and N are the total lateral dimension and the total number of faults perpendicular to the strike of the collinear set, respectively. The same parameters subscripted with a 'c' are total linear extent and number of cracks in a single collinear set. A_d is the total areal density of unrestricted faults and γ_a is the asperity percentage per single collinear set. In table 4 we give a set of values corresponding to a crustal-tectonic province of total areal extent A. The values in table 4 correspond to the five pairs of cases shown in figure 9. The paired cases (figure 9*a–e*, respectively) show the effect of varying the ratio of collinear to parallel number N_c/N. Differences between the parts of figure 9 might seem to indicate that as the ratio N_c/N (number of locked portions along the strike to lateral number of strike-slip faults) decreases, overall weakening would be increased. However, a closer examination of figure 9 reveals that the strong reduction in c_{66} with decreasing asperity percentage is insensitive to a twofold increase in the number of lateral strike-slip faults, N (see table 4). Hence the number of collinear locked portions of a fault N_c is a more important parameter than total areal density A_d. In spite of the fact that the doubly periodic crack model of Delameter *et al.* (1975) allows for mode I deformation, in no case does E_p or c_{11} decrease to less than half. On the other hand, c_{66} may weaken by as much as a factor of 500 ($\Lambda = 0.998$).

(*b*) *Checkerboard crack array*

Since stress concentrations become more intense as crack tips become closer and closer to one another ($\delta - 2\alpha \to 0$), the doubly periodic array shown in figure 7 might yield results peculiar to its geometrical spacing pattern. To investigate this possibility we now examine the weakening in a checkerboard (staggered) pattern of faults. This pattern is shown in figure 10*a*. In this case only mode II deformation is allowed. The finite-element technique is employed to determine the constitutive parameters by relating the components of stress with strain. Cracks here are assumed to be incompressible and perfectly sliding, thus accommodating shearing motion (mode II). Details of this technique of fault simulation have been discussed by Melosh & Raefsky (1981).

Shear weakening dominates this deformation style and is the most appropriate analogy to crustal faulting that extends to depth. The anisotropic shear weakening was studied as a function of fault interspacing. The results of this parameter study are shown in figure 10*b*. When

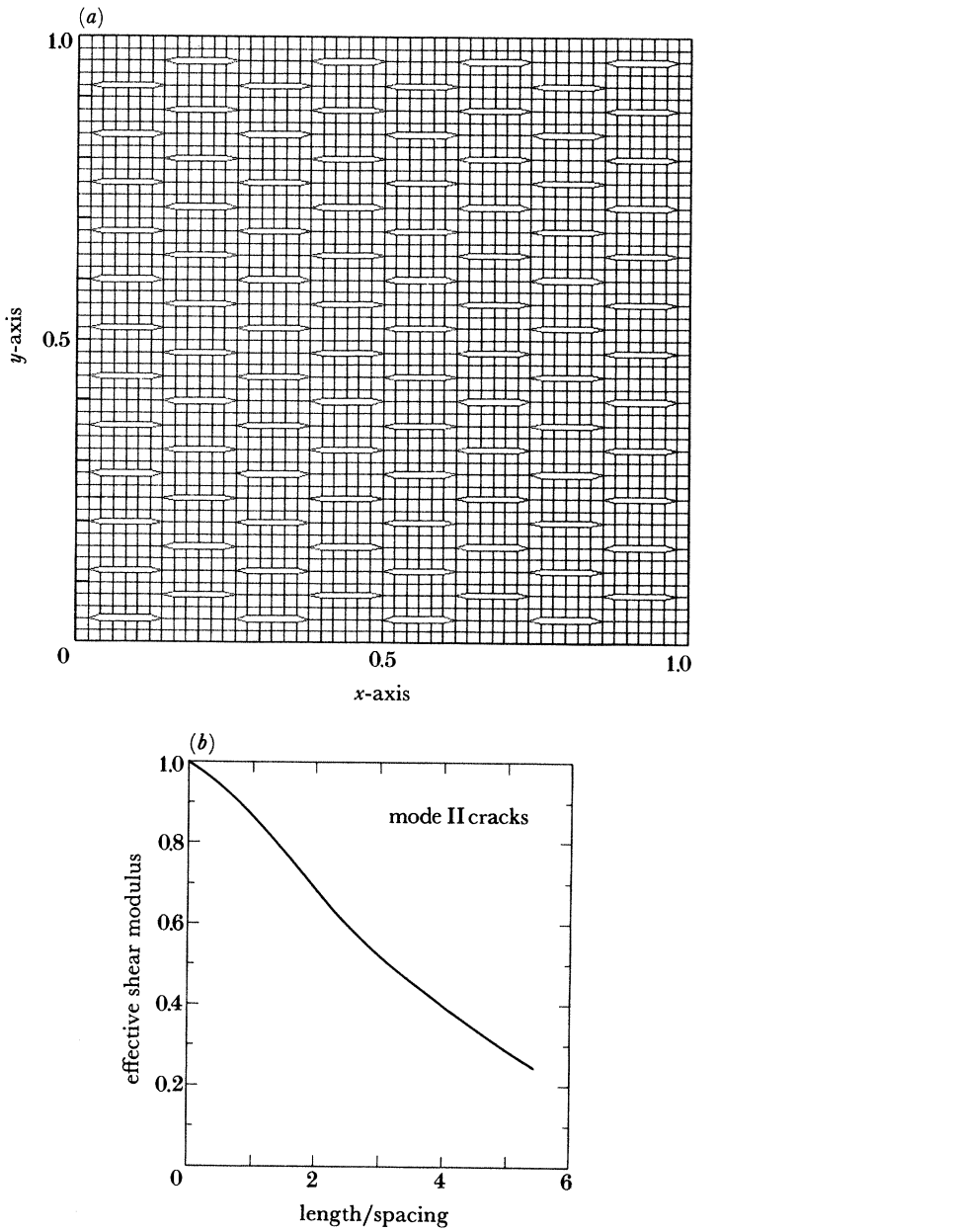

FIGURE 10. Finite element grid (*a*) and weakening of shear modulus G found in parameter study (*b*).

the ratio of length to spacing is zero the isotropic shear modulus G_0 is recovered. The curve in figure 10*b* indicates that the anisotropic weakening range, $A = 1 - G/G_0 \approx 0.9$, is obtained even with a relatively large number of locked portions N. We conclude that the pattern of weak fault interspacing is an important factor in estimating the range of weakening. All other parameters being equal, a two-dimensional plate with staggered crack array (figure 10*a*) is weaker than one with an unstaggered array.

PHILOSOPHICAL TRANSACTIONS OF THE ROYAL SOCIETY A MATHEMATICAL, PHYSICAL & ENGINEERING SCIENCES

8. Application of the anisotropy models to the transverse ranges

The two examples of deformation and stress that have been employed so far in this paper (figures 5 and 6) have served as quantitative measures of the physical effects caused by the faulting anisotropy. In this section we shall be concerned with a physical model that isolates the mechanical effect of the bidirectionality of parallel faulting in southern California and its immediate environs. Our approach will take a pedantic course to learn as much as possible about the causes and implications of each physical effect.

(*a*) *North–south compression, east–west extension*

The east–west *v.* northwesterly faulting in southern California is demonstrably shown in the maps of figure 1. The east–west fault trend corresponds to the Transverse Ranges. This longitudinal anomaly in faulting direction will be approximated as an elliptical anisotropic inclusion embedded in a thin anisotropic plate of infinite lateral extent. The model will be treated as a boundary-value problem in incremental elasticity theory of tractional type (see Gurtin 1972, p. 103). The stress condition applied to the plate is that of pure shear. At an infinite distance the y component of normal stress is τ_{yy}^{bg} (north–south) and the x component is τ_{xx}^{bg} (east–west). Pure shear demands that the deviatoric stresses are

$$\tau_{yy}^{\mathrm{bg}} = -\tau_{xx}^{\mathrm{bg}},\ \tau_{xx}^{\mathrm{bg}} > 0.$$

This ambient tectonic state is exactly that argued for by Zoback & Zoback (1980*b*) and is consistent with the overall geodetically recorded deformation pattern (Savage 1978). The contact between the embedded elliptical heterogeneity is non-dislocational, the interface maintaining continuity of both displacement and stress. The longitudinal heterogeneity lies with its major axis perpendicular to the ambient compressional axis (or equivalently the y-axis). Below we shall treat only strikes interior to the inclusion that are parallel to its major axis (see figure 2). The faults trend counter to the northwesterly direction and will act as a mechanical heterogeneity, a concentrator of stress.

The mathematical treatment of the associated boundary value has been given by Lekhnitskii (1954) and is given in detail in Appendix A. Comparison of both analytical and finite element numerical procedures to the published work of Lekhnitskii (1954, 1968, 1981) were crucial to the development of reliable model solutions. The analytical solutions rely upon defining a stress function and applying the compatibility conditions for the static planar problem. This yields a fourth-order partial differential equation of elliptic type (see (A 2) and (A 3) of Appendix A). The remaining work is then to obtain solutions to the contact problem by using affine transformations to the complex plane. The conditions of contact in the transform space are given by (A 34). Ultimately solutions for the stress and strain field interior to the elliptical boundary are obtained via solutions to (A 39). Rewritten, this equation is

$$\boldsymbol{M}\boldsymbol{S}^{\mathrm{int}} = \boldsymbol{S}^{\mathrm{ext}},$$

where the four-vector $\boldsymbol{S}^{\mathrm{int}}$ contains the three unknown (but spatially uniform) stress components $\tau'_{xx}, \tau'_{yy}, \tau'_{xy}$ together with the rigid rotation ϵ_{R} of the elliptical inclusion. Incorporation of the rotation ϵ_{R} is necessitated by the fact that boundary conditions of contact allow for net moments (Milne–Thomson 1968, p. 21; Lekhnitskii 1968, p. 32). The complex 4×4 matrix $\boldsymbol{M}$ and the complex four-vector $\boldsymbol{S}^{\mathrm{ext}}$ contain geometrical parameters, exterior and interior compliances

and boundary stresses, τ_{xx}^{bg}, τ_{yy}^{bg}. The exterior unknown stress components τ_{xx}, τ_{yy} and τ_{xy} are found via a polynomial solution for the stress function of the affine transform space (equation A 35). The assumed spatial uniformity of the interior stress field is verified *ab initio* from the finite element solution to the boundary value problem.

Model results based upon solutions to (A 39) are shown in figure 11. Of chief concern is the question of how the various models of anisotropy influence stress and strain fields within and immediately around the elliptical faulting heterogeneity. The values of the parameters plotted in figure 11 assume an ambient tectonic stress of 3.0 MPa. This value is unimportant, however, as it is the spatial variations that are of interest. Figure 11 shows spatial contours of stress intensity, $(3J_2')^{\frac{1}{2}}$, strain intensity, $(\frac{4}{3}I_2')^{\frac{1}{2}}$, and cubical dilatation, Δ. Both stress and strain intensity are proportional to the octahedral shear stress and strain, respectively (Freudenthal & Geiringer 1958, p. 240). The spatial distribution of strain intensity characterizes the distribution of elastically recoverable work. The definitions employed are

$$J_2' \equiv \tfrac{1}{6}[(\tau_{11}^{p}-\tau_{22}^{p})^2+\tau_{22}^{p2}+\tau_{11}^{p2}]^{\frac{1}{2}}, \tag{8a}$$

$$I_2' \equiv \epsilon_{11}^{p}\,\epsilon_{22}^{p}, \tag{8b}$$

$$\Delta \equiv \epsilon_{11}^{p}+\epsilon_{22}^{p}, \tag{8c}$$

where J_2' and I_2' are the second invariants of deviatoric stress and strain, ϵ_{11}^{p} and ϵ_{22}^{p} are first and second principal strains, and τ_{11}^{p} and τ_{22}^{p}, first and second principal stresses, respectively. Spatial variation in the cubical dilatation in figure 11 reveals regions of extension (contouring positive values) and regions of local compression (contouring negative values). The region absent of contour lines in figure 11 corresponds to the region of the ellipse where stress does not vary. For these analytical solutions this occurs by assumption. The validity of the assumption is substantiated by the finite element solutions shown in figure 13. For all cases shown in figure 11 except frame (*e*) the constitutive parameters of interior and exterior faulting anisotropy are the same when faults are unidirectional ($\phi^{e} = \phi^{e'}$). Therefore 11*a–d* shows the influence of the transversality of the longitudinal faulting structure with varying exterior strikes (ϕ^{e}) and constant interior strikes ($\phi^{e'} = 90°$). A comparison of figure 11*a* with figure 11*b* reveals that the difference between the crack anisotropy that assumes both mode I and II deformation and that assuming mode II only is, in fact, relatively small.

Strong symmetry about both *x* and *y* axes is revealed in figure 11 for all cases with $\phi^{e} = 45°$. As we discuss later in this paper, 45° orientation is a basic symmetry axis for crack models. Very different symmetries are found for $\phi^{e} \neq 45°$. For $\phi^{e} \neq 45°$ the symmetries fall into two types: $\phi^{e} < 45°$ and $\phi^{e} > 45°$ (see figure 11*c*, *d*). When $\phi^{e} = 30°$ a mirror-image symmetry occurs about an axis rotated clockwise about 30° (see figure 11*c*). On the other hand, if $\phi^{e} = 55°$ (keeping all other parameters the same as those of figure 11*a*, *c*), then this mirror axis of symmetry rotates to a position where exterior regions at enhanced extension–compression are about 40° out of phase with those when $\phi^{e} = 30°$.

Clearly the inclusion acts as a stress concentration. Note how quickly stress intensity drops off outside the ellipse, causing contour lines to bunch up. The surrounding faults have the ability to channel stress (recall figure 6), and their interaction with this elliptical stress concentration is what is revealed in figure 11. Comparison of the channelling in figure 11*c*, *d* most strikingly reveals the interaction of fault orientation with the effective elliptical stress concentration. It will be shown in §9 that the rigid rotation of the elliptical faulting inclusion is supported by

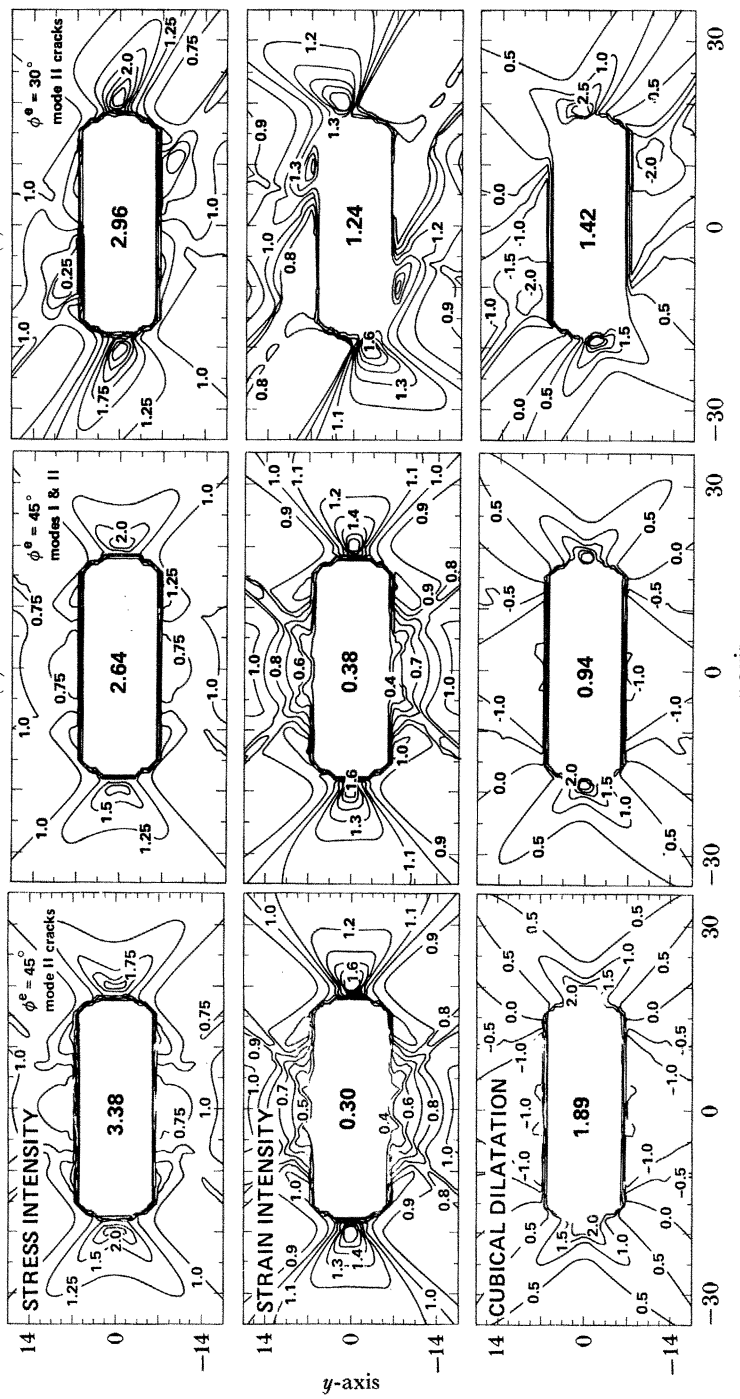

FIGURE 11 (*a*, *b*, *c*). For legend see opposite.

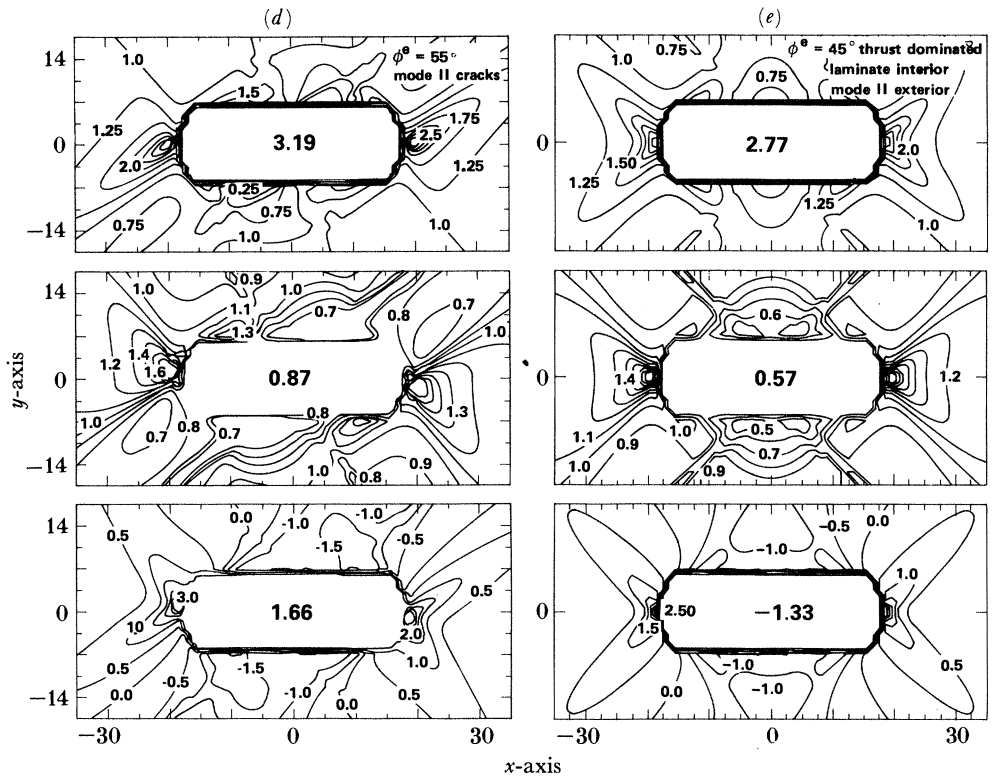

FIGURE 11. Contours of normalized stress intensity $(3J_2')^{\frac{1}{2}}$ (or $\frac{3^{\frac{1}{2}}}{2}$ times the octahedral shear stress), strain intensity, $(\frac{4}{3}I_2')^{\frac{1}{2}}$, and cubical dilatation for an elliptical inclusion of aspect ratio $c = 3.0$ in pure shear. Elastic mechanical properties of the inclusion and its surroundings are identical when the mean interior strikes ($\phi^{e'}$) and exterior strikes (ϕ^e) are equal for (*a*)–(*d*). In all cases $\phi^e = 90°$, $\Lambda = 0.9$, boundary stresses at infinity are $\tau_{xx}^{bg} = -\tau_{yy}^{bg} = 3.0$ MPa, $\tau_{xy}^{bg} = 0.0$; x and y units are tens of kilometres and the reference states for stress intensity and cubical dilatation are 5.20 MPa and 4.62×10^{-5}, respectively. Only case (*b*) allows for both mode I and II crack behaviour. For (*b*) the moduli correspond to the weakening shown in figure 9*e*, no. 10, 20% asperity. Case (*a*) corresponds to the case shown in figure 13. For (*a*), (*c*) and (*d*) the moduli at $\phi^e = 0°$, 90° are $E \approx E_p = 9.29 \times 10^4$ MPa, $\nu \approx \nu_p = 0.255$, $G = 3.7 \times 10^3$ MPa. For case (*e*) the inclusion has the properties of a thrust-dominated laminate whereas the exterior corresponds to mode II cracks. The interior properties correspond to the proportionalities shown in figure 21*d* (the compliances are increased by 2.47). Mean exterior strikes ϕ^e are as shown and analytical solutions for interior, τ'_{xx}, τ'_{yy}, τ'_{xy} (in megapascals) and reference states for strain intensity are: (*a*) 14.98, −4.33, 0.0, 4.78×10^{-4}; (*b*) 11.48, −3.68, −0.02, 3.69×10^{-4}; (*c*) 11.98, −4.00, 3.12, 4.14×10^{-4}; (*d*) 13.58, −4.18, −2.32, 4.49×10^{-4}; (*e*) 12.58, −3.13, 0.0, 3.69×10^{-4}, respectively.

the antisymmetry in the distribution of compression–extension that surrounds the transverse heterogeneity.

The case $\phi^e = 30°$ most closely corresponds to the orientation of northwesterly strike-slip (or wrench) faults surrounding the Transverse Ranges. When comparing this naïve model (figure 11*c*) with reality, two features show a positive correlation: specifically, the model with mode II cracks and $\phi^e = 30°$ predicts extension to the northeast and compression to the northwest of the Transverse Ranges. Extension is the dominant deformation mode along the eastern extent of the Garlock fault (Davis 1980; Plescia & Henyey 1982) and compression is a dominant feature in the Southern Coast Ranges (Dibblee 1976; Gawthrop 1978).

An important negative correlation is revealed in the analytical model results shown in figure 11*a–d*. Here, note the values for cubical dilatation. Net extension (positive dilatation) is

predicted when the interior anisotropy is of crack type. This feature is also shown in the positive large τ'_{xx} components that result (see also the finite element solution, figure 13). The Transverse Ranges, on the other hand, experience a rather uniform compression (Hadley & Kanamori 1977; Yeats 1983). Figure 11*e* shows results for $\phi^e = 45°$, mode II cracks on the exterior and a thrust laminate anisotropy on the interior. When the thrust anisotropy is assumed (figure 11*e*) then north–south strain accommodation is greatly enhanced, relative to east–west extension. The result is negative dilatation (compression) as shown at the bottom of figure 11*e*. However, even in the thrust laminate case, east–west extensional stress exceeds north–south compression by a factor of about 2. This model prediction is contradicted by the relatively strong north–south compressional state indicated by earthquake focal mechanisms and geological structure in the western Transverse Ranges (Yerkes & Lee 1979; Yerkes *et al.* 1981; Hill 1982; Pechmann 1983). The analytical model results, however, clearly demonstrate that a relatively large amount of stress is channelled into the contradirectional faulting heterogeneity. The sole source for this stress is the ambient forces caused by large-scale interplate shear.

Below we shall discuss an analytical model in which the elliptical inclusion is removed. Lekhnitskii 1954, 1968, 1981) has demonstrated that the tension–compression structure around relatively weak inclusions, $a'_{pp} \geqslant a_{pp}$, mimics that of the infinitely compliant limit; $a'_{pp} \to \infty$. Removing the inclusion allows us to isolate readily the channelling influence that is dominated by the surrounding fault anisotropy.

(*b*) *Analysis of the exterior stress channelling: elliptical hole in a plate under tension*

An anisotropic plate with an elliptical cutout is put into tension along the x axis, as shown in figure 12. The traction tangential to the ellipse boundary is shown by the arrows emanating from its surface. Arrows pointing outward indicate tension; those pointing inward, compression. The tangential edge stress, τ_t (see (A 9*a*) and figure A 1) is plotted as a function of angular position around the ellipse with the dotted line. The solid line in figure 12 shows the isotropic solution. Note that the isotropic case is symmetrical about both x and y axes. Here the anisotropy assumed is the two-dimensional strike-slip dominated type with $\Lambda \approx 0.9$. The fault orientation (shown in the inset in figure 12) destroys the symmetry about x and y axes that the isotropic case exhibits. For this anisotropy a mirror-image symmetry occurs along a shallow counter-clockwise rotated axis. Tension appears to be channelled orthogonally to fault strikes, the maximum values occurring at an angle of about 60° to the right of the y axis, i.e. orthogonal to fault direction (see figure 12).

(*c*) *Other faulting inhomogeneities: finite element calculations*

Model results shown in figure 11*a–e* together with figure 12 demonstrate the dominant influence of exterior fault orientation (ϕ^e) on the stress and strain field around the longitudinal anomaly in orientation. Aside from the surrounding orientation (ϕ^e), only the case of thrust laminate anisotropy seems to have a significant mechanical influence upon the qualitative picture that emerges from the models shown in figure 11. Even in the thrust-dominated case (figure 11*e*) the channelling in the surrounding medium is qualitatively similar to the other two cases with $\phi^e = 45°$ (figure 11*a*, *b*). This suggests that heterogeneities present in the surrounding crustal plate might strongly influence directional stress–strain channelling in all regions.

The case shown in figure 13 corresponds to the deformation problem posed by applying

PHILOSOPHICAL TRANSACTIONS OF THE ROYAL SOCIETY A MATHEMATICAL, PHYSICAL & ENGINEERING SCIENCES

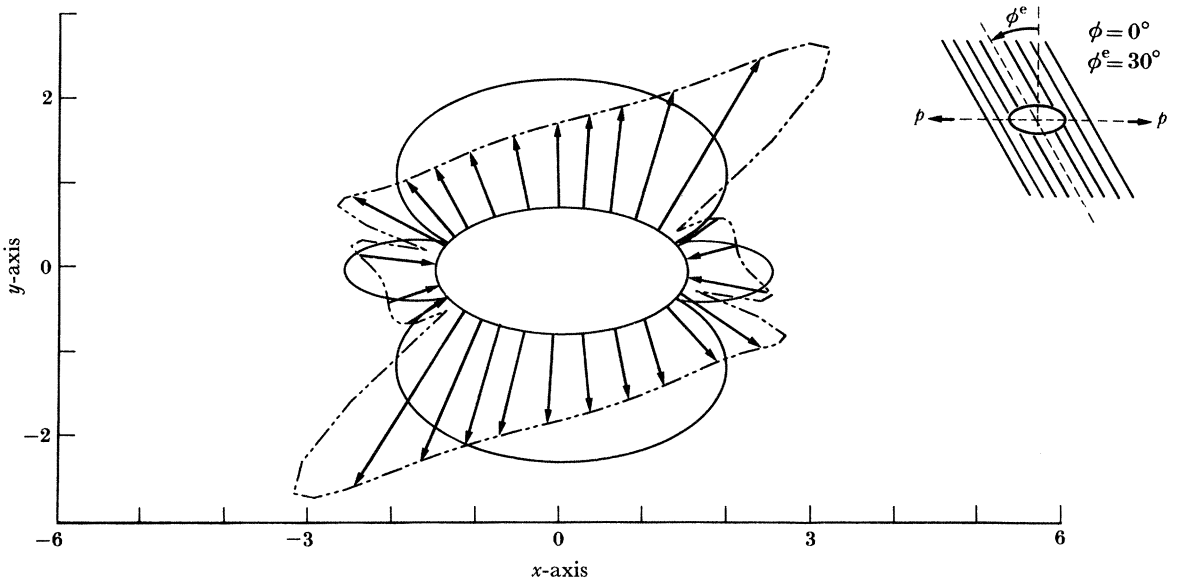

FIGURE 12. Tangential edge stress τ_t for a plate with hole and northwesterly striking faults; $A \approx 0.9$. Arrows emanating from the surface of the ellipse indicate the magnitude of tension; those directed toward the surface indicate compression. Note a shallow-angled axis of mirror symmetry and a minimum in tension magnitude roughly oriented with the faults. Note the maximum tension oriented orthogonal to fault direction. Parameters for this case correspond to case I of table 3 and figure 4 where $A \approx 0.9$. Solid lines outside the ellipse correspond to the isotropic solution. (See equation (A 22) of Appendix A.)

north–south compression and east–west extension to the plate shown at the bottom of figure 2 and elaborated upon in figure 11. In figure 13 we plot principal deviatoric stress and strain axes in and around the elliptical inclusion of weakening type and orientation corresponding to figure 11*a*. Notice that the stress orientation is influenced by the ellipse immediately outside its boundary. The reference ambient stress state is exemplified by the orientation and magnitude of the axes at the extreme left (west) and right (east) of figure 13. Note that there is a rotation of stress axes following an arc just outside the boundary of the ellipse from northwest to southeast. The degree of heterogeneity in stress and strain is relatively large. This is demonstrated by comparing these principal stresses with those caused by a bent dislocation (figure 15), an analogue of transpressional tectonics thought to be a relatively important mechanism of regional deformation (Rodgers & Chinnery 1973; Dickinson 1981).

The influence of additional spatial heterogeneity upon the pattern shown in figure 13 may be studied by calculating finite element solutions to the planar problem with elliptical inclusion and surrounding faults that correspond to those of figure 11*a* ($\phi^e = 45°$, $\phi^{e'} = 90°$ and all regions containing mode II cracks). The advantage of the finite element method is that it allows for the incorporation of spatial variation in anisotropic constitutive parameters beyond those represented by the elliptical heterogeneity.

Several observations suggest that the Sierra Nevada block experiences less deformation than its surrounding tectonic environment. Christensen (1965) suggests this on the basis of geological structure throughout this block. Seismic velocity structure suggest that this block is deeply rooted (Raikes 1980; Aki 1982). Figure 14 shows the solution for principal stress axes when

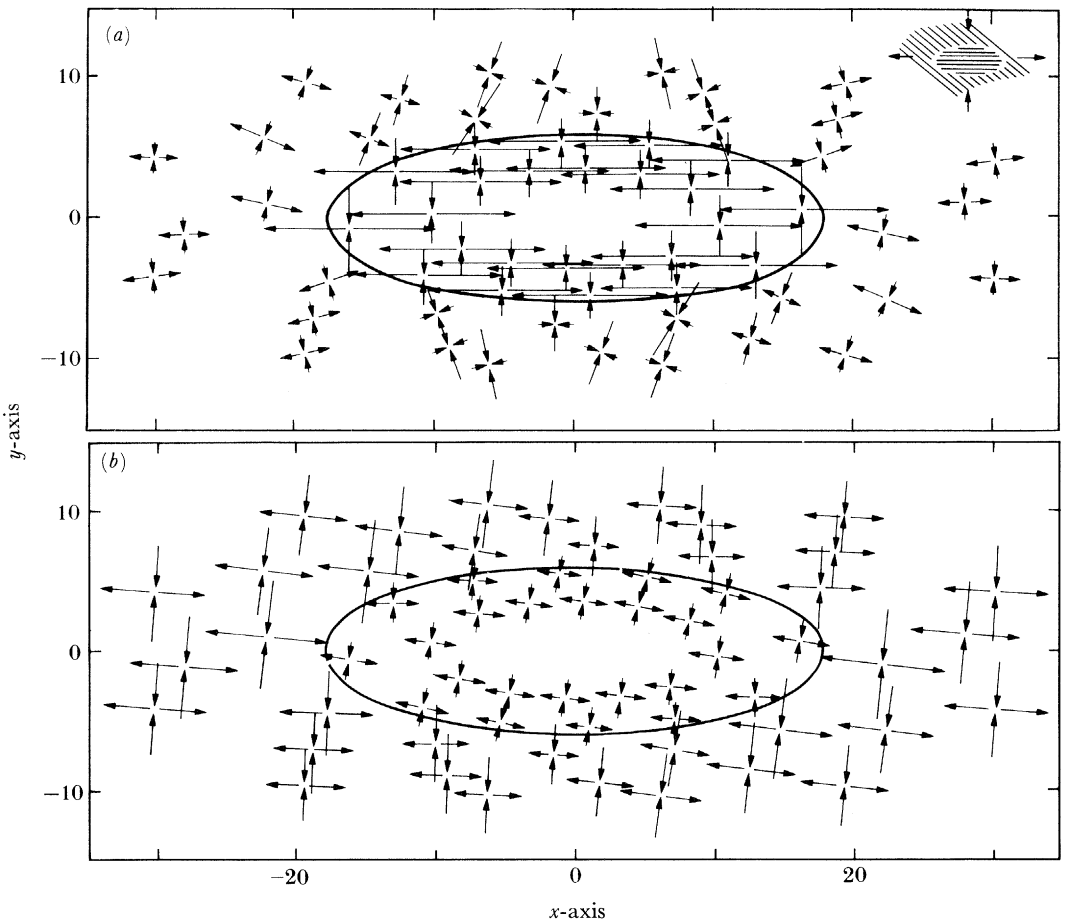

FIGURE 13. Principal horizontal deviatoric stresses (*a*) and strains (*b*) for case shown in figure 11 (*a*). The orientation is as shown in the inset with $\phi^e = 45°$. Plate is under north–south compression, east–west extension. Arrows at the end of orthogonal axes pairs indicate stress direction. Note the homogeneity of stress inside the ellipse. Note also the rotation of principal axes outside the ellipse boundary from north ($y \approx 7$, $x \approx 0$) to east ($y \approx 0$, $x \approx 22$).

the ambient stress system is applied to the configuration discussed above, only with the mechanical effect of this block included. It is assumed that the Sierra Nevada block represents a region where no faulting occurs (contrast the insets of figures 13 and 14). Quite naturally, the strong isotropic portion shows enhanced stress levels relative to the case in which the exterior region is uniformly anisotropic. More interesting is the fact that the values of the largest (extensional) principal horizontal stresses interior to the ellipse are decreased by as much as 50–75 % relative to the case shown in figure 13. Also of interest is that a large increase in stress magnitudes occurs to the south of the elliptical transverse structure. The orientation of the principal axes of stress to the southwest of this structure is rotated clockwise by about 30° or more owing to the presence of the strong block on the opposite side of the ellipse. Note that rotation around the ellipse boundary from north to south is fairly similar in figures 13 and 14. The strong Sierra Nevada block causes a slight clockwise rotation of stress axes interior to the ellipse. This degree of rotation is approximately the same as that observed in the principal axes deduced from focal mechanisms in the western Transverse Ranges (Yerkes & Lee 1979).

Figure 15 shows the rotation of horizontal principal stress axes caused by a bent dislocation,

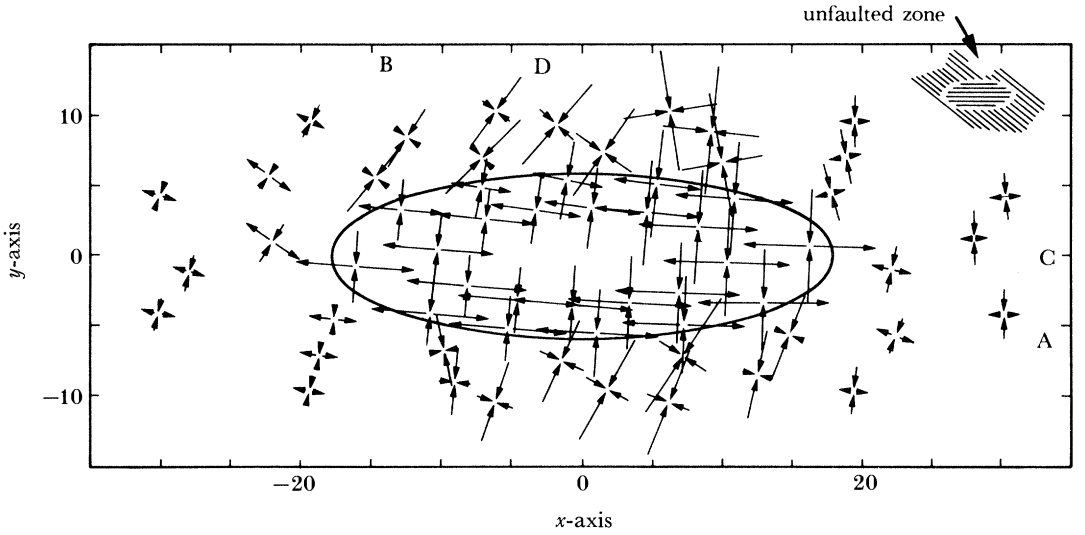

FIGURE 14. Principal horizontal stresses for plate with anisotropic inclusion and strong northeasterly section. Plate stress state at $y \to +\infty$ and $x \to +\infty$, fault weakening (Λ) directionality is the same as in figure 13. The unfaulted, isotropic zone represents the strong Sierra Nevada block (see figure 1); a mechanically competent zone in both geological (Christensen 1966) and seismic (Raikes 1980) interpretations. Relative to figure 13 note the enhancement of compressional stress in the north-northeastern and south-southeastern areas just outside the ellipse boundary. Note the slight clockwise rotation of axes and 50–70% decrease in magnitude in the ellipse interior caused by the presence of the Sierra Nevada block. Note also the 20–40° rotation and greater than 100% decrease in east–west extension, north–south compression magnitudes that occur to the west ($x < -15$) outside the ellipse when comparing with figure 13.

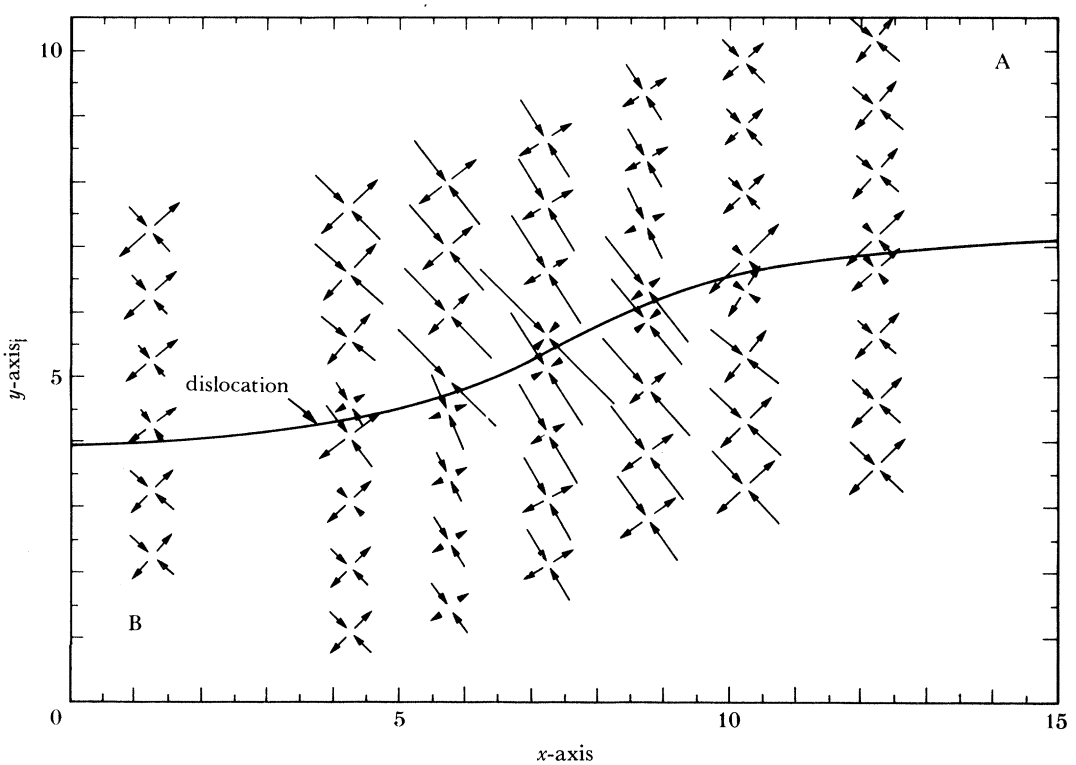

FIGURE 15. Principal horizontal stresses due to a bent dislocation undergoing mode II deformation. Note that the rotatation of stress axes along the dislocation are opposite to those occurring along a northwesterly striking fault that runs to the point ($y = 6$, $x = 0$) and then along the ellipse boundary in figure 13.

PHILOSOPHICAL TRANSACTIONS OF THE ROYAL SOCIETY A MATHEMATICAL, PHYSICAL & ENGINEERING SCIENCES

an analogue to the Big Bend feature of the San Andreas. Again, the ambient stress state is represented by axes to the extreme right or left, far from the dislocation.

The rotation of axes near the kink shown in figure 15 is opposite to the sense of rotation found in the elliptical inclusion model result as one moves from north to south across the inhomogeneity. The elliptical inclusion and bent dislocation predict qualitatively different rotations of principal axes in the vicinity of the San Andreas Big Bend (see figure 1 and 2). Examples of the deviations from the background shear stress axes orientation are shown in figure 22 where rotations are measured along traverses from position A to B and C to D in figures 14 and 15.

The spatial variation in magnitude of horizontal principal stresses revealed in the solution shown in figure 13 is noteworthy. Interior to the ellipse stresses are significantly enhanced, containing a strong east–west extensional component. This enhanced extension appears both in the stress and strain, consistent with the positive dilatation of figure 11*a*. Although a strong extensional stress component may have acted during the Pliocene (Hall 1981*a*, *b*; Yeats 1983), Quaternary deformation of the western Transverse Ranges is dominated by compressional stress (Crowell 1976).

As noted above, the strong east–west extensional state diminishes in thrust-dominated anisotropy interior to the ellipse (figure 11*e*). Note that the stress due to a bent dislocation alone acts to enhance north–south compression within the ellipse if placed in its geometrically appropriate position; also the influence of the Sierra Nevada block isolated in figure 14 shows a tendency to reduce this strong east–west extension. Some combination of various stress effects undoubtably causes the enhancement of north–south compression. Fault frictional effects will also tend to enhance compression in the region of the Big Bend (Scholz 1977).

In figure 16 we have constructed the same basic physical problem as in figure 13. In this case an allowance for strong gradients in the stiffness, c_{66}, along the east–west and north–south directions is modelled. There is a large body of geophysical evidence indicating that the San Andreas transform system consists of locked and unlocked segments (Agnew & Sieh 1978; Turcotte & Schubert 1982). Within the southern California region this implies greater strength north of the Transverse Ranges and some mechanical weakness to the south. This idea is supported by both the distribution of seismicity (Allen *et al.* 1965; Briggs *et al.* 1977) and by the relatively strong creeping motion along surficial fault expressions within the San Jacinto fault system (Louie *et al.* 1985).

The stiffness c_{66} varies by a factor of 15 from east to west within the ellipse (figure 16*a*) and by the same factor from north to south outside the ellipse (figure 16*b*). The north–south case reveals that there is a substantial difference in stress and strain when comparing results with those when there is no gradient (figure 13). The gradient placed outside the ellipse (figure 16*b*) has a mild homogenizing effect on the stress orientation both to the south and north of the ellipse. Stress axes do not rotate about an arc just outside the ellipse boundary as when there is no gradient (compare stresses in figure 16*b* and figure 13). The strains also become relatively homogenized when there is a north–south gradient.

Evidence for strength contrast interior to the ellipse is indicated by the apparent enhancement of late Quaternary deformation in the Santa Barbara Channel (Yerkes & Lee 1979). A general large-scale east–west contrast would be consistent with the general rheological differences between oceanic and continental lithosphere (Froidevaux *et al.* 1977). Such an east–west

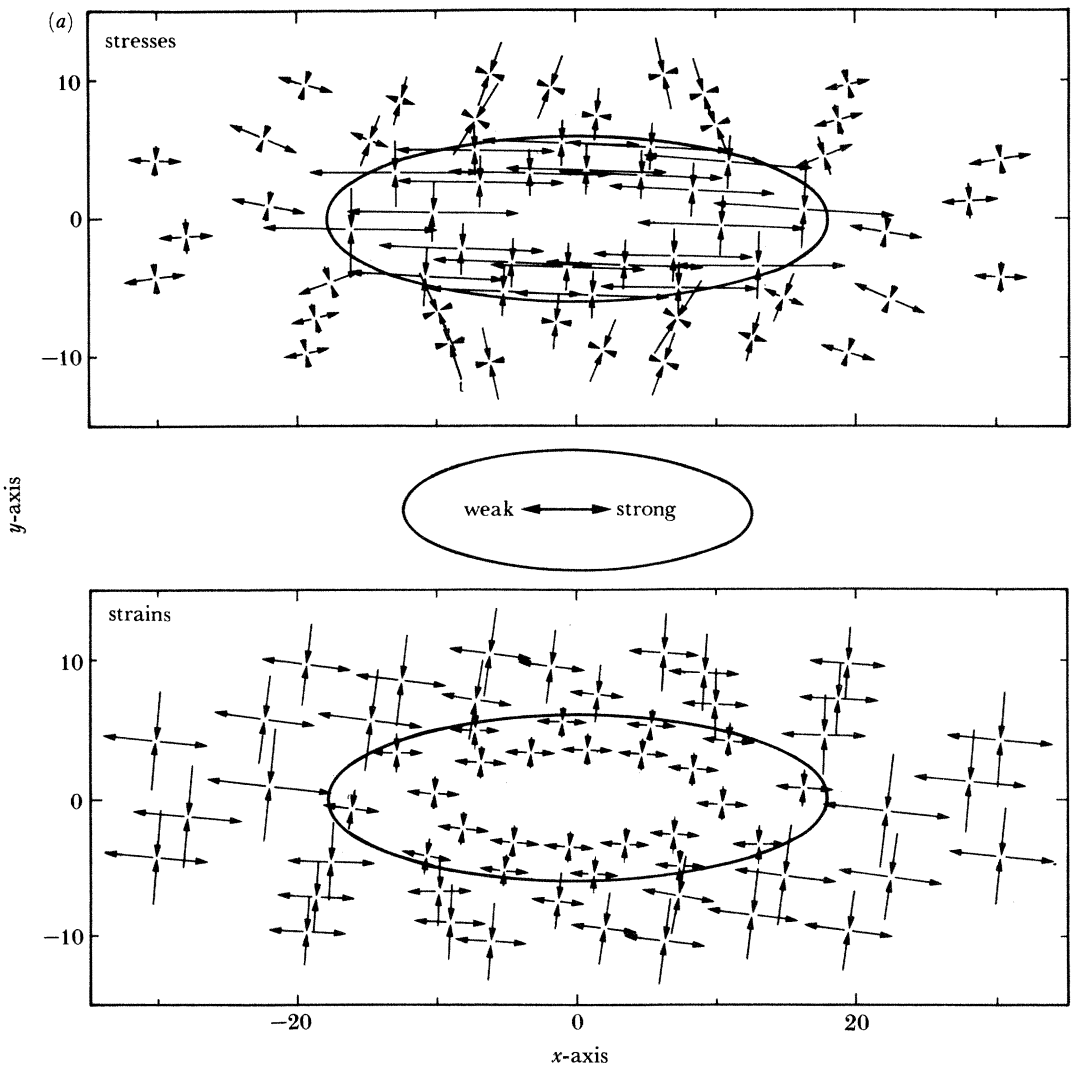

FIGURE 16. Influence of north–south, east–west mechanical contrasts upon principal horizontal stresses and strains. Fault orientation and north–south compression, east–west extensional state is the same as in figures 13 and 14. The Sierra Nevada block is present. The east–west contrast within the ellipse (*a*) assumes that $c_{66} = c_{66}^{\mathrm{iso}}\,[(1-0.06\Lambda)\,x/a_* + (1+0.06\Lambda)]$. The north–south contrast outside the ellipse (*b*) assumes $c_{66} = c_{66}^{\mathrm{iso}}\,[(1-0.06\Lambda)\,y/3b_* + \frac{1}{2}(1+0.06\Lambda)]$. ($c_{66}^{\mathrm{iso}}$ meaning isotropic value). The x and y dependent functions correspond to a factor of 15 in contrast for c_{66} and c'_{66}, respectively. North–south and east–west contrasts, qualitatively, correspond to distribution of moderate magnitude seismicity (see, for example, Allen *et al.* 1965; Briggs *et al.* 1977; Turcotte & Schubert 1982).

lithospheric contrast is strongly suggested by a statistical sampling of plutonic rocks (Baird & Miesch 1984). East–west variation interior to the ellipse has less influence on the stress or strain than when there is no gradient (compare figure 16*a* with figure 13). Apparently contrasts in the surrounding medium have a much more significant influence upon the static stress and strain environment than those in the interior (compare figure 16*a* with figures 14 and 16*b*).

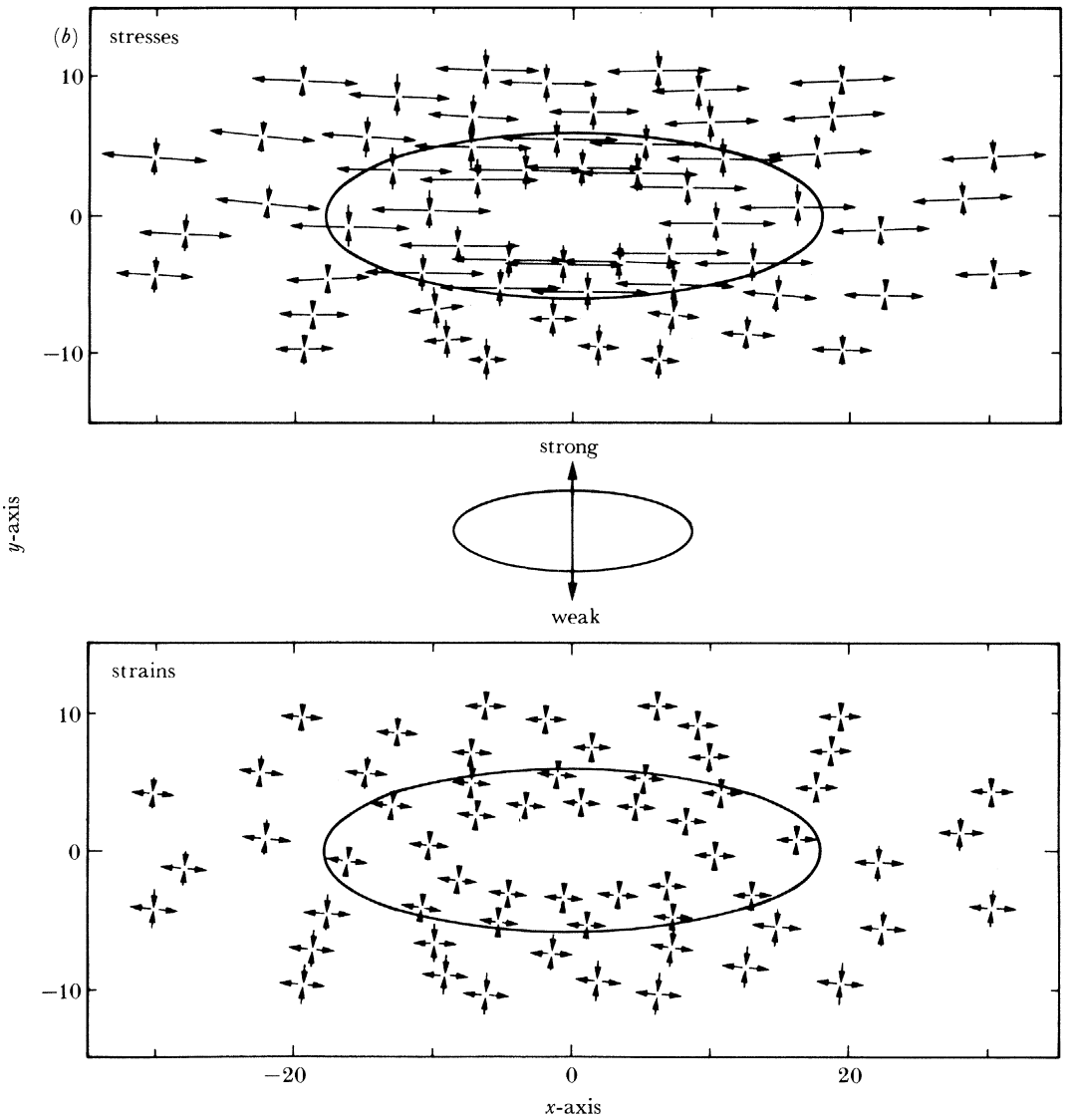

FIGURE 16(*b*). For legend see p. 321.

9. RIGID ROTATION

It has become a widely accepted view that contiguous crustal tectonic units, or blocks, are capable not only of large translational motion on geological time scales, but also of rather large rotations. The primary evidence is palaeomagnetic (Simpson & Cox 1977; Kammerling & Luyendyk 1979). In this section we shall show that crustal pieces that are identified as regional faulting heterogeneities can exhibit relatively strong rotations even when the ambient tectonic stress field is that of pure shear. Seeber (1983) has suggested that the sustenance of such rotational allochthonus behaviour depends critically upon the activity of an imbricate system of low-angle thrust faults surrounding the 'microplate'. We shall show that the underlying mechanism that drives the rotational motion does not require an imbricate structure. In fact, a local stress field sufficient to impart an effective torque on such a tectonic unit is described

by solutions to the problem of a thin elastic, fault-weakened plate acted upon by pure-shear horizontal stresses that contains an elliptical inclusion in which faults oriented counter to the general directional weakening act as an effective heterogeneity. This faulting heterogeneity is precisely that treated in the previous section and to which figures 11 and 13 refer.

There are, however, some subtleties of the question of rotation that will be more strikingly revealed by developing a tutorial example in which an externally applied twist drives the rotation. Later, this exercise will help clarify how rigid rotation takes place in the pure-shear ambient tectonic stress field.

(*a*) *Concentrated twist applied to a rigid inclusion*

In the tutorial example a rigid elliptical inclusion is embedded in a directionally faulted plate, and a concentrated twisting moment M_{zx}, applied to the centre of the inclusion, supplies the mechanical energy necessary to generate a rigid rotation through angle ϵ_{R}. The solution to this boundary value problem has been developed by Milne-Thomson (1968) and is discussed fully in Appendix A. Two geometrical features – the slenderness of the rigid inclusion (a_*/b_*) and the orientation of surrounding unidirectional strikes of faults (ϕ^{e}) – together with the planar orthotropic compliances, a_{11}, a_{22}, a_{12} and a_{66}, form the parameter space to be investigated with this tutorial example. The rigid rotation (in radians) may be written analytically as

$$\epsilon_{\mathrm{R}} = (M_{zx}/\pi)\, \Upsilon(a_{11}, a_{22}, a_{12}, \Lambda, \phi^{\mathrm{e}}, a_*, b_*). \tag{9}$$

The function Υ is given by (A 30) for the general case in which surrounding faults are non-aligned with respect to either major or minor axes of the rigid elliptical inclusion. The units of Υ are reciprocal newtons and a_*, b_* are half the lengths of the major and minor axes, respectively.

Particularly germane is the question of what rotational magnitudes can be generated given the variety of faulting anisotropies presented in §§5 and 7. In other words, the most fundamental question is: given particular values M_{zx}, a_*, b_*, how do the directional constitutive properties affect the magnitude of rotation ϵ_{R}? What is discovered by employing the Milne-Thomson (1968) expression for the rigid rotation (equation (9)) is that compressional and extensional modes of deformation are the most important mechanical aspects that support strong rotation. Shear weakening ($\Lambda \to 1$, or large a_{66}) enhances the extension–compression deformation.

Figure 17 summarizes the influence of the fault weakening and orientation upon the rotation for values of a_*/b_* ranging from 2.5 to 10.0 for the concentrated twist case from (9). The magnitude of the total rotation, ϵ_{R}, clearly increases as fault weakening parameter $\Lambda \to 1$. This influence of increased weakening upon the total rotation is shown in figure 18 for $a_*/b_* = 3.75$ and $M_{zx} = 2.11 \times 10^{15}$ N.

Figure 17*a* corresponds to weakening where strong compression–tension straining is allowed within the weak component of the faulted crust (for example figure 4*b*). The strongest influence of fault orientation upon rigid rotation occurs when there is some contrast in the directional bulk compressibilities. The contrast is expressed by the percentage of differences between the compliances a_{11} and a_{22}. For a 2% contrast in these compliances the effect of the fault strike, ϕ^{e}, almost disappears and for a 20% contrast the influence is still fairly weak (see figure 17*b* and *c* respectively). In fact, Milne–Thomson's (1968) analytical expression for Υ $(a_{11}, a_{22}, a_{12}, \Lambda, \phi^{\mathrm{e}}, a_*, b_*)$ as summarized in figure 17 reveals a rather remarkable lack of influence of ϕ^{e} in all cases. When the surrounding crust is characterized by incompressible oriented faults, the rotation appears to be entirely independent of the strike of these same faults.

PHILOSOPHICAL TRANSACTIONS OF THE ROYAL SOCIETY A MATHEMATICAL, PHYSICAL & ENGINEERING SCIENCES

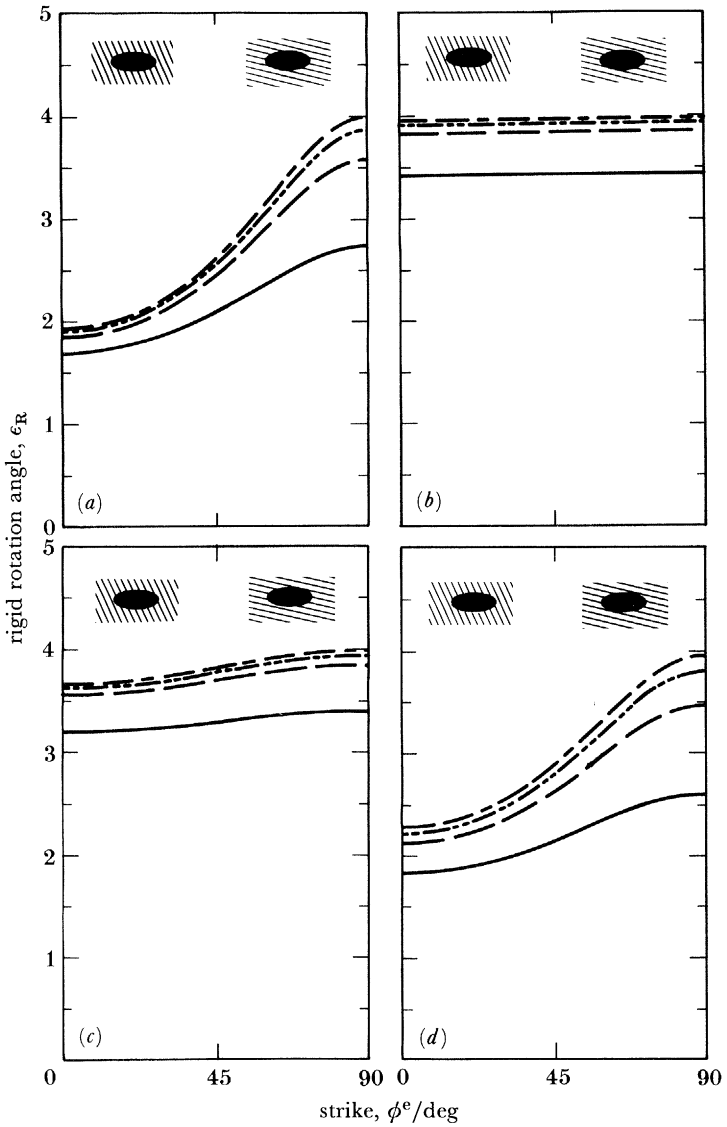

FIGURE 17. Total rigid rotation ϵ_R resulting from applied twist as a function of fault strike ϕ^e: (*a*) laminate thrusting; (*b*) mode II cracks; (*c*) mode I and II cracks; (*d*) laminate strike-slip. For each case the twisting moment is $M_{zx} = 2.11 \times 10^{15}$ N and $a_* = 280$ km. The ellipse aspect ratios correspond to (lines from bottom to top): $a_*/b_* = 2.5$, $a_*/b_* = 5.0$, $a_*/b_* = 7.5$, and $a_*/b_* = 10.0$. Percentage differences in compliances, i.e. $200 \times (a_{11} - a_{22})/(a_{11} + a_{22})$, values of Λ, a_{11}, a_{12}, a_{66} in MPa^{-1} and scaling factors in radians are respectively: (*a*) 460%, 0.99, 5.1×10^{-5}, -2.15×10^{-7}, 4.4×10^{-3}, 1 unit = 2.99×10^{-7}; (*b*) 2%, 0.999, 1.29×10^{-5}, -2.15×10^{-7}, 4.4×10^{-2} 1 unit = 1.47×10^{-6}; (*c*) 20%, 0.999, 1.29×10^{-5}, -2.33×10^{-7}, 4.4×10^{-2}, 1 unit = 1.6×10^{-6}; (*d*) 280%, 0.92, 2.03×10^{-4}, -1.73×10^{-7}, 5.66×10^{-4}, 1 unit = 6.59×10^{-7}.

This independence of ϕ^e occurs because of the symmetrical character of the a_{16} and a_{26} compliances (see figure 21) that enable the effects of shear stress τ_{xy} upon ϵ_{yy} and ϵ_{xx} to nearly cancel one another when $a_{11} \approx a_{22}$.

The independence of rotation upon ϕ^e allows us to simplify Milne-Thomson's expression for Υ and obtain an expression for total rotation ϵ_R as a function of Λ. Consider the fourth-rank tensor in equation (T2) of table 2, which operates on the fourth-rank compliance tensor A^{ijrs} with $\psi^e = 0°$ in (4) (see §5). As defined throughout, compliances a_{11}, a_{22}, a_{12} and a_{66} correspond

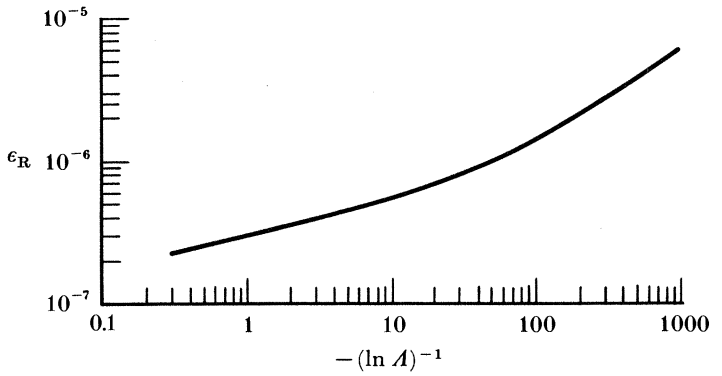

FIGURE 18. Plot of the analytical dependence of ϵ_R upon weakening parameter Λ for mode II cracks in the concentrated twist case. As $\Lambda \to 1$, $-\ln \Lambda \approx L$. In this case $a_*/b_* = 3.7$, $M_{zx} = 2.11 \times 10^{15}$ N and $a_* = 280$ km. At $-\ln \Lambda)^{-1} = 1000$; $a_{11} = 1.10 \times 10^{-5}$, $a_{22} = 1.08 \times 10^{-5}$, $a_{12} = -2.15 \times 10^{-7}$ and $a_{66} = 4.4 \times 10^{-2}$ MPa^{-1}, i.e. the same compliances as in (*b*) of figure 17.

to planar orthotropy with faults running parallel to the y-axis. For finite strike ϕ^e those compliances most sensitive to compression–extension, a_{11}, a_{22}, are

$$\bar{a}_{11} = a_{11} \cos^4 \phi^e + (2a_{12} + a_{66}) \sin^2 \phi^e \cos^2 \phi^e + a_{22} \sin^4 \phi^e; \tag{10a}$$

$$\bar{a}_{22} = a_{11} \sin^4 \phi^e + (2a_{12} + a_{66}) \sin^2 \phi^e \cos^2 \phi^e + a_{22} \cos^4 \phi^e \tag{10b}$$

(see also Lekhnitskii (1981), p. 44).

For shear-mode-dominated anisotropy (in particular for mode II cracks) then $a_{11} \approx a_{22}$ and consequently $\bar{a}_{11} \approx \bar{a}_{22}$ with maximum compressional weakness occurring at $\phi^e = 45°$ (see figure 21*b*). The Young modulus for this maximum weakening $E_{\frac{1}{4}\pi}$, is

$$E_{\frac{1}{4}\pi} \equiv 1/\bar{a}_{11} = 1/\bar{a}_{22}. \tag{11}$$

By using (10) with $\phi^e = \frac{1}{4}\pi$ and then substituting from (11) into (A 30), allowing $\Lambda \to 1$ (or equivalently letting the slide modulus $L \ll 1$) and finally approximating $E_{\frac{1}{4}\pi} \approx \frac{2}{3}E_0 L$ yields an approximate form for (9):

$$\epsilon_R = \frac{3M_{zx}\nu_0}{2\pi E_0 L}[1-(1-\nu_0)\Gamma^{\frac{1}{2}}+(\nu_0^{-1}+1)\Gamma]/[a_* b_* - b_*(a_* - b_* + 2a_*\nu_0)\Gamma^{\frac{1}{2}} + a_*(a_*+b_*)\Gamma],$$

where $\Gamma \equiv \frac{2}{3}E_0/G_0$ and E_0, G_0, ν_0 are isotropic moduli and Poisson's ratio. In simplified form (12) is

$$\epsilon_r = M_{zx}\hat{C}/L, \tag{13}$$

where (12) defines the constant $\hat{C}$.

The parameter study presented in figure 17 demonstrates the importance of compression–extension in generating rotation ϵ_R. For both laminate anisotropy models ϵ_R is approximately doubled when faults are aligned with the axis of the rigid ellipse (see figure 17*a*, *d*). For this type of anisotropy (laminate) significant contrast in directional compliances a_{11} and a_{22} occur (see figure 4 and figure 21*c*, *d*). When compressionally weak faults are aligned with the ellipse axis, the surrounding material acts as though it were softer than when faults and axis are not aligned.

The accuracy of (12) compared with the results from the full Milne–Thomson (1968)

PHILOSOPHICAL TRANSACTIONS OF THE ROYAL SOCIETY A MATHEMATICAL, PHYSICAL & ENGINEERING SCIENCES

expression (9) when $L \leqslant 0.1$ demonstrates the role that the overall shear weakening plays in enhancing compression–extension immediately outside the ellipse boundary. Below we discuss how this same compression–extension enhancement revealed in the applied twist case plays a critical role in a more geophysically realistic situation.

(*b*) *Passive rotation in pure shear*

We now consider the rotational displacement field that occurs along the interface of an elliptical faulting heterogeneity. The contact with the surrounding unidirectional faulted crustal plate is non-dislocational and no stress discontinuities occur. The physical situation is then precisely the same as that discussed in §8, figures 11 and 13. The investigation is limited to the case where the elliptical heterogeneity is acted upon by a pure shear stress field in which the axes of compression and extension are aligned with the semimajor and major axes of the ellipse, respectively. This alignment pursues explanations of the apparently allochthonus rotational behaviour of the Transverse Ranges (Yeats *et al.* 1974). However, during much of the rotation of the Ranges, principal horizontal interplate stress axes have not been aligned (Hamilton 1978; Crouch 1979; Hall 1981*a*). The model predicts that under the Quaternary

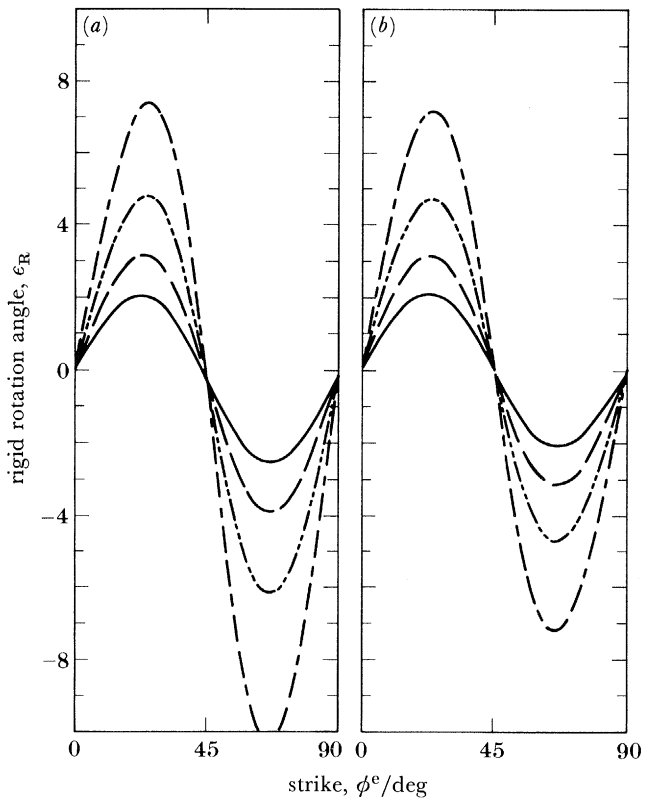

FIGURE 19. Rigid rotation (passive rotation in pure shear) of an elliptical faulting heterogeneity as a function of surrounding parallel fault strike: (*a*) mode I and II; (*b*) mode II only. Negative values correspond to counter-clockwise rotation and vice versa for positive values. Solid and dashed lines correspond to increasing values of a_*/b_* as in figure 17. The ratios are $a_*/b_* = 1.75$, 2.25, 2.75 and 3.25. Scale factors for rigid rotation angles are 1 unit $= 10^{-4}$ radians in all cases. The directional moduli are the same as mode II only, and modes I and II of figure 11*a*, *b*, respectively. As discussed in §10 of the text the direction of rigid rotation is positively correlated with the direction of shear τ_{xy} within the faulting heterogeneity. Values of the background tectonic stress and a_* are the same as in figure 11.

alignment of tectonic stress axes with respect to the Transverse Ranges (Zoback & Zoback 1980*b*), a net clockwise torque acts on the Ranges. This local torque does not depend upon the activity of an imbricate thrust structure.

In contrast to the case of a concentrated twist applied to a rigid inclusion, a relatively strong surrounding crust actually enhances the net rotational magnitude, ϵ_{R}. This is not surprising! The faulting heterogeneity rotates in passive response to the uneven distribution of forces surrounding it (see figure 20).

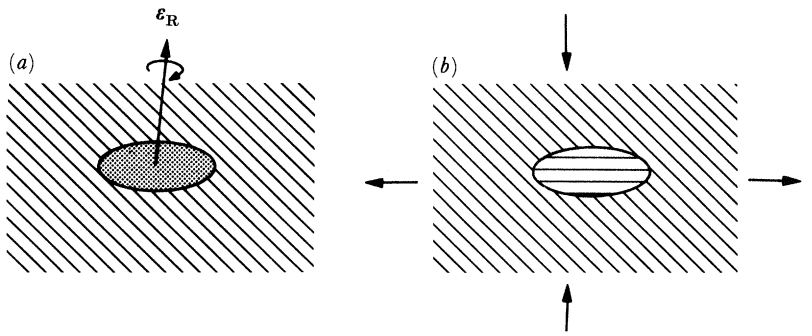

FIGURE 20. Schematic diagram of the differing physics of the two rotation models: (*a*) concentrated twist with rigid inclusion; (*b*) rotation in pure shear with faulted inclusion. Applied twist (*a*) corresponds to results shown in figures 17 and 18 and to the analytical result embodied in equation (A 30) of Appendix A. Passive rigid rotation in a pure shear environment (*b*) corresponds to the results shown in figure 19, which are obtained from the solution to equation (A 39).

Since it is precisely this anomalous stress field that induces the rigid rotation of the heterogeneity it now becomes important to consider again figures 11 and 13. Essential to the generation of finite rigid rotation is the maintenance of a local stress field that is both heterogeneous and markedly not pure shear. A further requirement is that the local stress field be asymmetric with respect to the minor axis of the elliptical heterogeneity: only then does a net torque operate on the heterogeneity. This fact is revealed in figure 19*a*, *b*, where a parameter study with solutions to (A 39) shows that $\epsilon_{\mathrm{R}} = 0$ when faults in the surrounding crust have strikes of $\phi^{\mathrm{e}} = 45°$. Note the symmetrical character of stress intensity, strain intensity and cubical dilatation in figure 11*a*, *b* and of principal axes shown in figure 13 when $\phi^{\mathrm{e}} = 45°$ and the anisotropy is of crack-deformation type. The distribution of stress intensity and cubical dilatation of figure 11*a* belies the fact that no net torques act upon the elliptical inclusion. Note from the vector $\boldsymbol{S}^{\mathrm{int}}$ defined in (A 40) that interior shear stress τ'_{xy} and rotation ϵ_{R} are simultaneously solved for in system (A 39). When exterior strike angles ϕ^{e} pass from values less than 45° to values greater than 45° the sense of rotation switches from clockwise to counter-clockwise. A similar sign reversal in the solution for τ'_{xy} also occurs. The sign of τ'_{xy} is always positively correlated with the sign of ϵ_{R}. The maximum values of ϵ_{R} occur at $\phi^{\mathrm{e}} = 22.5°$ and 67.5°. These maxima correspond to maxima for the non-orthotropic generation of normal shear strain induced by finite a_{16} and a_{26} (see (A 1) and figure 21*b*).

The concentrated twist case has demonstrated the importance of compression–extension deformation just outside the ellipse boundary. For rotation generated in tectonic shear, the sign of the cubical dilatation adjacent to the elliptical heterogeneity's longitudinal sides is antisymmetric about the y-axis for $\phi^{\mathrm{e}} \neq 45°$ (see figure 11*a*–*e*). When the cubical dilatation is negative (compression) to the left of the y-axis ($x < 0$) north of the heterogeneity and positive

to the right (see figure 11*c*), then the net torque is clockwise. Crustal material for $0° < \phi^e < 45°$ is compressed in the upper left and lower right hand corners, while extension occurs in the upper right and lower left hand positions with respect to the heterogeneity (see figure 11*c*). For exterior strikes with $45° < \phi^e < 90°$ the opposite antisymmetry occurs (see figure 11*d*), the interior shear stress τ'_{xy} is negative and the net torque is counter-clockwise. This compression–extension symmetry is precisely that which must occur in the applied twist case (figure 20*a*). However, with ambient-shear-induced rigid rotation (figure 20*b*) the orientation of net torque is left to be determined by the fault orientation. The stress channelling induced by the parallel faults in the surrounding crust selects which of the two symmetry types (see figure 11*c*, *d*) will occur.

(*c*) *Analytical rotation model and the Transverse Ranges*

It may now seem tempting to speculate at length concerning the Neogene rotation of the Transverse Ranges, particularly because there are strongly contrasting views on how to interpret palaeomagnetic and geological evidence (see, for example Hall 1981*a*, *b*). Clearly, however, the magnitudes of crustal rotations inferred from palaeomagnetic studies (*ca.* 50–70°; Kamerling & Luyendyk 1979) imply finite strain. We have not treated the case of finite strain in this paper. The study here treats a geometry that is probably applicable only to Quaternary deformation. It is therefore pertinent to address only two questions concerning the rotation of the Transverse Ranges: (1) Can the Transverse Ranges rotate as a contiguous tectonic unit? And, if so: (2) What is the predicted Quaternary sense of such a rigid rotation?

The results of the analytical model rather strongly support the notion that the Transverse Ranges act as contiguous crustal piece capable of rigid rotation even on geodetically measurable time scales. Since Quaternary faults that surround the Ranges are nearly parallel to the San Andreas ($\phi^e < 45°$) and the sense of rigid rotation predicted by the model is clockwise.

Finally we should return to the suggestion of Seeber (1983) that low-angle imbricate thrust structures are genetically related to allochthonus rotation. What is demonstrated above is that imbricate structure is not a necessary condition for rotation. None the less, an imbricate thrust structure is a pervasive feature of the western Transverse Ranges (Yeats 1981, 1983). Studies of aftershock sequences are the most conclusive observational evidence (Langston 1978; Corbett & Johnson 1982). The genetic relation of imbricate thrust structure to rotation probably occurs as it is necessitated by vertical variation of horizontal, large finite strains.

10. Synopsis

Model features that should not be left subtle are highlighted in this section. Results fall into three categories: (1) anisotropic models for an oriented, multiply faulted crust, (2) delineation of the anisotropic stress–strain channelling that occurs around a longitudinal faulting anomaly (analogue of the Transverse Ranges), and (3) explanation of how the longitudinal anomaly rotates rigidly in non-dislocational contact with the surrounding faulted plate, which experiences an ambient tectonic stress field analogous to North–American–Pacific interplate shear.

(*a*) *Result no.* 1: *crustal tectonic anisotropy*

First, we have shown how a laminated medium consisting of strong and weak components reduces the effective elastic moduli of a fault weakened crust (see figures 3 and 4 and table 3). Also considered has been the weakening induced by oriented faults which are modelled as a doubly periodic array of cracks (see figures 8, 9 and 10 and table 4). The three-dimensional

laminate model is one of transverse isotropy with x-axis symmetry (see equation (2) and table 2). When the laminate model is employed with faults dipping vertically, the linear elastic constitutive equation corresponds to one of an orthotropic planar system. Crack array models also exhibit orthotropic symmetry. The angular dependence of the compliances (a_{11}, a_{12}, a_{66}, a_{16}, a_{26}) is summarized in figure 21 for both two-dimensional laminate and crack models. The most significant difference between laminate and crack models occurs at angles of 45°. For the crack model a_{66} shows almost an order of magnitude decrease at 45°, whereas in the laminate model the reduction is only to between one third and one half. Resistance to shear straining is maximum at 45°, except in the compression dominated laminate (figure 19*d*).

Caution must be exercised in properly applying the equations (1) for a two-component laminate model because the condition of positive definiteness of the strain energy function may be violated (see figure 4*b*). The laminate anisotropy model has distinct advantages over crack models if exaggerated extension–compression is a desired model feature. However, unlike laminate models, crack models do not require a relatively large volumetric fraction of the crust to behave as an isotropically weak material (see figure 4). On the basis of figure 21 we deduce that for an arbitrarily oriented crust with parallel shearing cracks (strike-slip faults) the appropriate anisotropy corresponds to the elastic constants of a material with two-dimensional tetragonal–disphenoidal symmetry (see Gurtin 1972, p. 88). This symmetry simplifies analytical treatment because the cross-compliances have antisymmetry ($a_{16} = -a_{26}$) and compressional compliances are equal ($a_{11} = a_{22}$). We have shown how the effective fault-weakened anisotropy models work in some simple deformation boundary value problems. Consideration of in-plane stress (see figure 6) and the vertical strain of a non-aligned three-dimensional heterogeneity due to pure two-dimensional shearing (see figure 5) clearly demonstrates that stress–strain channelling is substantial when the weakening parameter $\Lambda \geqslant 0.9$ (or, equivalently, when Biot's (1965) slide modulus $L \leqslant 0.1$).

(*b*) *Result no.* 2: *stress channelling around the Transverse Ranges*

The main impetus of this paper has been to demonstrate that oriented fault weakening in the brittle elastic crust has a strong influence upon the way in which stress and strain occur locally within an interplate shearing zone such as that in the southern California region. Toward this goal the analytical solutions shown in figures 11 and 12 and the finite-element solutions shown in figures 13, 14 and 16 are our primary result. A fundamental feature of the elliptical inclusion model of the Transverse Ranges appears: the discordant geometrical orientation that the faults within the Ranges represent has a substantial tendency to concentrate regional stress (see figures 11 and 13). However, the anisotropic elliptical inclusion model with ambient pure shear fails to explain the apparent relative magnitudes of horizontal stresses determined from the orientation of fold axes and earthquake focal mechanisms (Yerkes & Lee 1979; Yerkes *et al.* 1981; Hill 1982). Matching the observed enhancement of the north–south principal stress requires the imposition of other strength contrasts or stress fields, or both. In this regard, the relative strength of the Sierra Nevada block may be of significance (see figure 14) as may the stress caused by transpression along the Big Bend of the San Andreas (see figure 15). A strong north–south gradient in fault weakening is also significant to the overall stress distribution (see figure 16*b*). Strength contrasts within the elliptical heterogeneity have comparatively little effect (see figure 16*a*).

In that the elliptical heterogeneity in figures 11, 13, 14 and 16 mimics the mechanics of the

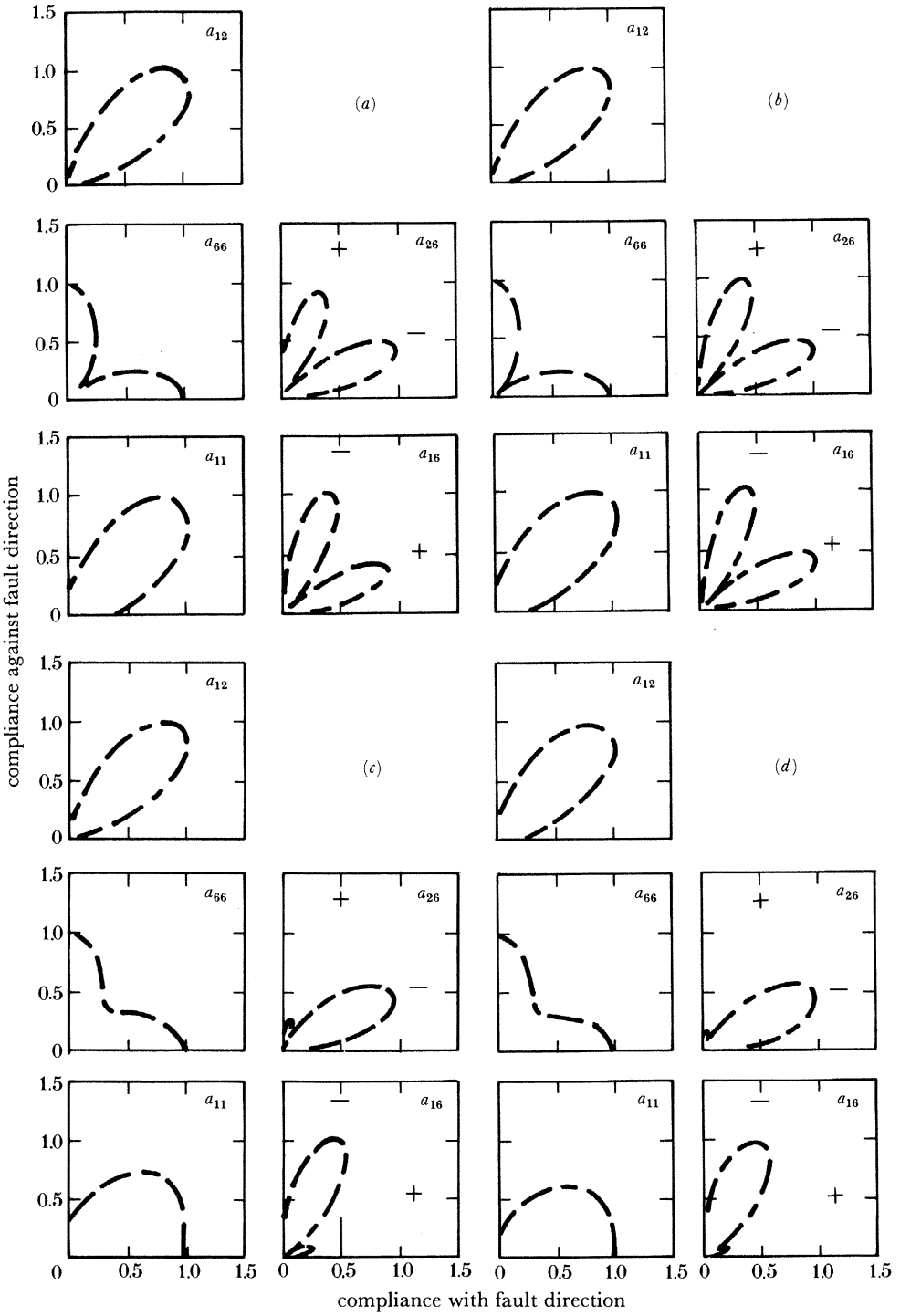

FIGURE 21. Relative value of the compliances as ϕ^e is varied from 0° (abscissa) to 90° (ordinate). Unit value is the maximum for the projection. a_{22} is the mirror image of a_{11} for each case. '+' and '−' on a_{16} and a_{26} plots represent positive and negative regions respectively. Cases (*a*) and (*b*) have compliances $a_{22} = 1.16 \times 10^{-5}$, $a_{12} = -2.78 \times 10^{-6}$, $a_{66} = 2.3 \times 10^{-4}$ and $a_{11} = 1.85 \times 10^{-5}$ for (*a*), and $a_{11} = 1.16 \times 10^{-5}$ MPa^{-1} for (*b*). Case (*c*) corresponds to the laminate model of figure 4*a* with $a/b = 0.19$ and the compliances with the fault direction are $a_{11} = 2.03 \times 10^{-4}$, $a_{22} = 6.08 \times 10^{-5}$, $a_{12} = -1.73 \times 10^{-7}$, $a_{66} = 5.66 \times 10^{-4}$ MPa^{-1}. Case (*d*) corresponds to case III, figure 4*c*, (laminate, thrust dominated) with $a/b = 0.19$ and the compliances with the fault direction are $a_{11} = 4.70 \times 10^{-5}$, $a_{22} = 2.40 \times 10^{-5}$, $a_{12} = -9.33 \times 10^{-7}$ and $a_{66} = 6.10 \times 10^{-5}$ MPa^{-1}. At $\phi^e = 15°$, a_{16} and a_{26} are: (*a*) 3.67×10^{-5}, -4.01×10^{-5}; (*b*) 3.99×10^{-5}, -3.99×10^{-5}; (*c*) 2.98×10^{-5}, -1.01×10^{-4}; (*d*) 2.98×10^{-5}, -1.01×10^{-4} MPa^{-1}, respectively.

PHILOSOPHICAL TRANSACTIONS OF THE ROYAL SOCIETY A MATHEMATICAL, PHYSICAL & ENGINEERING SCIENCES

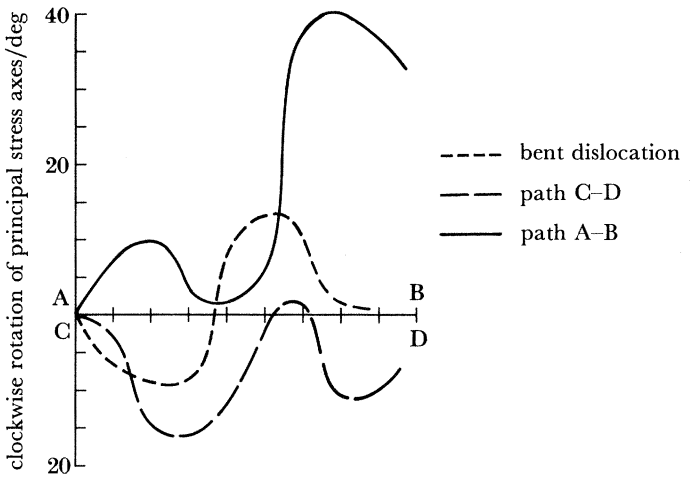

FIGURE 22. Variation of stress axis direction following paths from A to B and C to D in figure 14 and A to B in figure 15. The path across the bent dislocation traverses the area of maximum rotation. Similar paths across other regions of the elliptical inclusion plots shown in figures 13, 14 or 16 will show this type of strong variation. Curves are approximate, accurate to within about $\pm 4°$.

static stress–strain field of the Transverse Ranges in southern California, these results have some implications for interpretations of geodetic or stress field data (or both) in the region. The elliptical faulting heterogeneity causes considerably greater and more widespread perturbation of the stress field than that due to a bent dislocation alone. A comparison of the amount of rotation of the principal axes of stress as one follows a line connecting positions A and B in figures 14 and 15 is shown in figure 22. Since the model is entirely elastic and because we can neither constrain the regional variation of the fault-weakening parameter, A, nor constrain the geometry of the Transverse Ranges precisely to an ellipse, a direct comparison of figures 13, 14 and 16 with reductions of geodetic data from within the region (see, for example, Savage 1978) is tenuous. Interestingly, however, all solutions for stress–strain fields within the faulting heterogeneity (i.e. the elliptical inclusion) show a remarkable homogeneity in both orientation and magnitude of principal axes (see figures 13, 14 and 16). This homogeneity is observed in the overall deformation that occurs in the Transverse Ranges (Yerkes & Lee 1979).

(*c*) *Result no.* 3: *rotation in interplate shear*

Using an expression derived analytically by Milne-Thomson (1968) (see equation (A 30) of Appendix A) we are able to show the influence of both the fault-weakening parameter, A, and orientation of the primary faulting trend of the surrounding elastic crust, ϕ^{e}, on the total rigid rotation when a twist is applied to an inclusion (see figure 20*a*). These results are summarized in figures 17 and 18. Plots of the Milne–Thomson (1968) solution for the case of mode II cracks (figure 17*b*) reveals that ϕ^{e} has a negligible influence. For the case of laminate thrust anisotropy the magnitude of rotation increases when the major axis of the ellipse is parallel to the fault direction (see the hump in figure 17*a*). Compressional and extensional modes of deformation enhance rotation. For a very weak crust of oriented mode II cracks (strike-slip faults) a simplified form of the Milne–Thomson (1968) expression reveals that the magnitude of rigid rotation increases linearly with the inverse of Biot's (1965) slide modulus L. This proportionality helps clarify how shear-mode weakening (strike-slip) accommodates large compression–

extension deformation necessary for rotation. The case of applied twist is tutorial since an *ad hoc* torque is required.

However, a net torque acts upon an elliptical, transversely oriented, faulting heterogeneity which is embedded in a faulted plate subjected to shear at a distance (see figure 20*b*). The net torque arises from natural circumstances. It can be explained by the mirror-image symmetry in compression–extension that surrounds the heterogeneity (see figure 11*c*, *d*). The torque causes clockwise rotation for surrounding faults with parallel strikes, ϕ^e, less than 45°, and counter-clockwise for strikes greater than 45° (see figure 19). Palaeomagnetic evidence favours late Cainozoic deformation in which the Transverse Ranges experience a net clockwise rigid rotation (Luyendyk *et al.* 1980). Though such evidence is not incontrovertible, it is consistent with the ongoing sense of rigid rotation predicted by our analytical model because Quaternary strike orientation is roughly bounded by $30° \leqslant \phi^e \leqslant 45°$ (see figures 1 and 19).

11. Conclusions

Chinnery (1964) was one of the first to argue that the elastic shear modulus of the brittle elastic crust is effectively reduced by an order of magnitude in zones of active tectonism. His assertions rested upon calculations of the stress fields induced by static dislocations. Self-consistent global lithospheric stress fields computed by Richardson *et al.* (1979) by using a linear elastic constitutive assumption rely upon assuming that major transform faults, mid-oceanic rifts and other weak zones are characterized by a rigidity that is decreased by an order of magnitude over those measured seismically. Anisotropy models capture many of the essential ingredients of both the weakening and directionality associated with faulting.

The pervasive Quaternary strike-slip (or wrench) structure that occurs in southern California has been analysed in this paper by solving a series of planar, linear elastic boundary value problems of tractional type that assume pure shear forces at infinity. The northwesterly strike-slip faulting has been approximated as a constitutive anisotropic weakening. When this northwest-striking pattern is broken by a longitudinal transversely (east–west) oriented crustal piece the problem becomes a complicated one. The complexity occurs because the two regionally distinct fault sets channel the ambient tectonic stress in differing directions. By approximating the transversely oriented piece as having an elliptical boundary we can apply the analytical treatment of Lekhnitskii (1954). The combination of both analytical and finite element solutions allow us to come to two fairly robust conclusions:

1. The cross-cutting tectonic fabric of the Transverse Ranges in southern California cause the Ranges to act as a stress concentrator.

2. Rigid rotation of the Transverse Ranges is mechanically supported by an asymmetric distribution of stress and elastic strain encircling it. For Quaternary tectonic orientation a clockwise sense to this rotation is predicted.

Regarding the concentration of stress, we should clarify that this is entirely consistent with the notion that bends, or kinks, in strike-slip structures give rise to zones where stresses build up periodically, and energy stored elastically is released in the form of large earthquakes (Koide & Bhattacharji 1977). Our analytical and finite element models are one approach to quantifying the question of regional variation in stored elastic energy and stress. The Sierra Nevada batholith may also act as a significant heterogeneity. Spatial and temporal variation

PHILOSOPHICAL TRANSACTIONS OF THE ROYAL SOCIETY A MATHEMATICAL, PHYSICAL & ENGINEERING SCIENCES

of seismicity and deformation along Quaternary faults of southern and northern California (Raleigh *et al.* 1982; Sharp 1982) probably implies that the effective system of faulting heterogeneity is also spatio-temporal in character. However, over both the span of the Quaternary and of recorded seismic history the Transverse Ranges comprise an important tectonic feature with anomalous deformational style and sense (Allen *et al.* 1965; Briggs *et al.* 1977; Yerkes & Lee 1979; Yerkes *et al.* 1981).

The homogeneity of stress within the Transverse Ranges is predicted by our models. This homogeneity is consistent with the notion that the Transverse Ranges act as a contiguous tectonic unit. Palinspastic reconstructions and palaeomagnetic evidence indicate that this unit is capable of sustaining significant tectonic rotation. We have divided southern California into two spatially distinct fault sets. This idealized division has allowed us to examine what influence the northwesterly striking faults have upon the second (east–west) fault set and vice versa. The homogeneity of stress within the second set (east–west) occurs because of encirclement by the northwesterly striking set. A substantial net torque acts upon the crust containing the second set of faults. Our model predicts an asymmetric distribution of channelled tectonic stress with respect to the longitudinal axis of the east–west fault set. This asymmetric distribution provides the necessary mechanical energy to generate the torque. Detachment faults and an imbricate structure are probably associated with the allochthonous motion of the Transverse Ranges (Yeats 1981). However, the calculations presented in this paper demonstrate that the physical circumstances that lead to the generation of tectonic rotation need not require an imbricate structure. If the tectonic rotation of the Transverse Ranges is a real component of Quaternary deformation then it should be observable geodetically. It is possible that space geodetic strategies will be capable of discriminating such evidence in the future (Musman 1982; Lyzenga *et al.* 1986).

Our study is similar to that of Zoback & Zoback (1980*a*), Hill (1982) and of Bird & Baumgardner (1984) in one aspect: that fault orientation is an essential geometrical feature that must be accounted for if consistent relations between overall tectonic stress and interaction among adjacent tectonic units are to be explained. There is also a fundamental difference. We have derived stress–strain fields on the basis of solutions of the compatibility equations of elasticity without explicitly accounting for stress-limiting plastic yield surfaces in terms of fault friction. The major discovery retrieved from the analytical and finite element treatments is that both the torque-sustaining allochthonous rotation and the accumulation of excess recoverable strain energy within the Transverse Ranges can be attributed to the contradirectional fault orientation.

R. S. Saunders has provided useful geological insight and we wish to thank him for his support and encouragement. The finite element calculations could not have been carried out without the expert assistance and guidance of Arthur Raefsky. The authors wish to thank W. B. Banerdt, A. K. Baird, S. M. Baloga, B. H. Hager and J. B. Plescia for useful discussions. Matthew Golombek's comments on a rough draft helped immensely. Vladimir Petrov and the J.P.L. library must be thanked for finding S. G. Lehknitskii's 1954 *Inzhenernyi Sbornik* article from the Linda Hall Library, Kansas City, Missouri. This research was supported by the Geodynamics Program Office and was carried out in the Planetology and Oceanography Section and in the Tracking Systems and Applications Section of Jet Propulsion Laboratory, California Institute of Technology, under contract no. NAS7-100, sponsored by the National Aeronautics and Space Administration.

PHILOSOPHICAL TRANSACTIONS OF THE ROYAL SOCIETY A MATHEMATICAL, PHYSICAL & ENGINEERING SCIENCES

Appendix A. Analytical solution for a plate with elliptical hole or inclusion

In this appendix we outline the Kolosov–Muskhelishvili method for obtaining the analytical solutions for cases of an elliptical inclusion or cutout in a non-orthotropic plate under plane stress. Here we also write down the solutions plotted in figures 11*a–e*, 12, 17, 18 and 19 in analytical form. Our outline attempts to be as complete as possible. However, it is recommended to the reader who wishes to rederive solutions fully that they refer to the monographs by Lekhnitskii (1968) and Milne-Thomson (1968).

The stress–strain equations for planar non-orthotropic elasticity are:

$$\left.\begin{aligned} \epsilon_{xx} &= a_{11}\tau_{xx}+a_{12}\tau_{yy}+a_{16}\tau_{xy},\\ \epsilon_{yy} &= a_{12}\tau_{xx}+a_{22}\tau_{yy}+a_{26}\tau_{xy},\\ \epsilon_{xy} &= a_{16}\tau_{xx}+a_{26}\tau_{yy}+a_{66}\tau_{xy}, \end{aligned}\right\} \tag{A 1}$$

where the finite compliances a_{16} and a_{26} are due to the non-alignment of faults with the x or y coordinate axes (see table 2). Here we shall assume that coordinates x and y coincide with major and minor axes of the ellipse (see figure 12) and that the origin is at its centre. The stress function F is defined by

$$\tau_{xx} = \partial_{yy}F, \quad \tau_{yy} = \partial_{xx}F, \quad \tau_{xy} = -\partial_{xy}F \tag{A 2}$$

where subscripts on ∂ indicate partial differentiation with respect to independent variables x and y respectively. Application of the compatibility equation for the stresses to (A 1) and (A 2) casts the mathematical boundary-value problem as

$$\Xi^4 F = 0, \tag{A 3a}$$

where the partial differential operator is

$$\Xi^4 \equiv \prod_{k=1}^{4} (\partial_y - \mu_k \partial_x) \tag{A 3b}$$

and μ_k are the four complex roots of the characteristic equation

$$a_{11}\mu^4 - 2a_{16}\mu^3 + (2a_{12}+a_{66})\mu^2 - 2a_{26}\mu + a_{22} = 0. \tag{A 3c}$$

In (A 3b) Π indicates the sum-product. Of the four roots μ_k there exists a complex conjugate pair such that $\mu_k = \alpha_k + \mathrm{i}\beta_k$ and $\mu_k = \alpha_k - \mathrm{i}\beta_k$ for $k = 1, 2$ and $k = 3, 4$, respectively. The roots of the characteristic equation (A 3) suggest the separation of (A 3a) via the affine transformation to the complex variables:

$$z_k = x + \mu_k y. \tag{A 4}$$

Since the roots μ_k form a conjugate pair, we need only to consider $k = 1, 2$. For plane problems with no body forces present and $\mu_1 \neq \mu_2$ the boundary value problem (A 3a) may be recast by using complex independent variables (A 4) to form the four analytical functions $\Phi_k(z_k) \equiv \mathrm{d}F_k/\mathrm{d}z_k$, $\Phi_k'(z_k) \equiv \mathrm{d}\Phi_k/\mathrm{d}z_k$ such that

$$F = 2\,\mathrm{Re}\,[F_1(z_1) + F_2(z_2)], \tag{A 5a}$$

$$\tau_{xx} = 2\,\mathrm{Re}\sum_{k=1}^{2} \mu_k^2 \Phi_k'(z_k), \tag{A 5b}$$

$$\tau_{yy} = 2\,\mathrm{Re}\sum_{k=1}^{2} \Phi_k'(z_k), \tag{A 5c}$$

$$\tau_{xy} = -2\,\mathrm{Re}\sum_{k=1}^{2} \mu_k \Phi_k'(z_k), \tag{A 5d}$$

$$u = 2\,\mathrm{Re}\sum_{k=1}^{2} p_k \Phi_k(z_k), \tag{A 5e}$$

$$v = 2\,\mathrm{Re}\sum_{k=1}^{2} q_k \Phi_k(z_k). \tag{A 5f}$$

In equations (A 5) we assume that background stresses, rigid rotations, and pure translations are absent. In (A 5*e*, *f*)

$$p_k \equiv a_{11}\mu_k^2 + a_{12} - a_{16}\mu_k, \tag{A 6a}$$

$$q_k \equiv a_{12}\mu_k + a_{22}/\mu_k - a_{26}. \tag{A 6b}$$

Edge stresses along an elliptical cutout with tension at angle ϕ applied at infinity

Boundary tractions of components $\hat{t}_n \cdot \hat{\imath}$, $\hat{t}_n \cdot \hat{\jmath}$ are considered with respect to outward normal $\hat{n}$. In an elliptical cutout, or hole, then $\hat{n}$ is towards its centre (see figure A 1). If the coordinates x, y emanate from the centre of the elliptical hole, the normal $\hat{n}$ is

$$\hat{n} = g_{nx}\hat{\imath} + g_{ny}\hat{\jmath} \tag{A 7a}$$

and the tangent $\hat{t}$ is

$$\hat{t} = g_{tx}\hat{\imath} + g_{ty}\hat{\jmath}, \tag{A 7b}$$

where $g_{.x}$ and $g_{.y}$ are direction cosines of tangent and normal vectors. For the boundary of an elliptical hole with x and y positive,

$$g_{ty} = g_{nx} = -b_* \cos\theta/l, \tag{A 8a}$$

$$g_{tx} = -g_{ny} = a_* \sin\theta/l, \tag{A 8b}$$

where a_* and b_* are the half-lengths of the major and minor axes respectively. Here θ is measured counter-clockwise from the positive x-axis and

$$l \equiv (a_*^2 \sin^2\theta + b_*^2 \cos^2\theta)^{\frac{1}{2}}.$$

The stress tangential to the surface of an ellipse is

$$\tau_t = 2\,\mathrm{Re}\sum_{k=1}^{2} (g_{ty} - \mu_k g_{tx})^2 \Phi_k'(z_k) \tag{A 9a}$$

and the stress normal to the surface is

$$\tau_n = 2\,\mathrm{Re}\sum_{k=1}^{2} (g_{ny} - \mu_k g_{nx})(g_{nx} + \mu_k g_{ny}) \Phi_k'(z_k). \tag{A 9b}$$

Stress boundary conditions for Φ_k are

$$2\,\mathrm{Re}\sum_{k=1}^{2} \Phi_k(z_k) = \mp \int_0^s \hat{t}_n \cdot \hat{\jmath}\, \mathrm{d}s \tag{A 10a}$$

$$2\,\mathrm{Re}\sum_{k=1}^{2} \mu_k \Phi_k(z_k) = \pm \int_0^s \hat{t}_n \cdot \hat{\imath}\, \mathrm{d}s, \tag{A 10b}$$

PHILOSOPHICAL TRANSACTIONS OF THE ROYAL SOCIETY A MATHEMATICAL, PHYSICAL & ENGINEERING SCIENCES

where the integral over surface s is taken to be counter-clockwise, and the upper and lower signs are for outward and inward projecting normals, respectively.

For forces applied to the boundary we may evaluate $\Phi_k(z_k)$ as a power series solution in the reciprocal complex variable:

$$\zeta_k = [z_k + (z_k^2 - a_*^2 - \mu_k^2 b_*^2)^{\frac{1}{2}}]/(a_* - \mathrm{i}\mu_k b_*). \tag{A 11}$$

When no net force resultants occur due to body couples and no body forces are present then a Fourier series expansion

$$\mp \int_0^s \hat{t}_n \cdot \hat{\jmath}\, \mathrm{d}s = \sum_{n=-m}^{n=m} \gamma_n^y \, \mathrm{e}^{\mathrm{i}n\theta}, \tag{A 12a}$$

$$\pm \int_0^s \hat{t}_n \cdot \hat{\imath}\, \mathrm{d}s = \sum_{n=-m}^{n=m} \gamma_n^x \, \mathrm{e}^{\mathrm{i}n\theta} \tag{A 12b}$$

is appropriate. The complex Fourier coefficients γ_n^y, γ_n^x may be determined by integration on $[\theta\colon -\pi; \pi]$ by using the left hand side of (A 10a, b). Here coefficients γ_n with negative n are assumed to be the complex conjugate of those with corresponding positive n. This treatment of boundary conditions has been discussed at length by Novozhilov (1961).

The complex variable ζ_k arises as a natural property of mapping of boundary conditions (A 10a, b) onto the unit circle. For an ellipse the consecutive conformal mappings are

$$z = \tfrac{1}{2}(a_* + b_*)\,\zeta + \tfrac{1}{2}(a_* - b_*)/\zeta, \tag{A 13a}$$

$$z_k = \tfrac{1}{2}(a_* - \mathrm{i}\mu_k b_*)\,\zeta_k + \tfrac{1}{2}(a_* + \mathrm{i}\mu_k b_*)/\zeta_k \quad (k = 1, 2), \tag{A 13b}$$

(see Milne-Thomson (1968), p. 192, Lekhnitskii (1968), p. 33, or Lekhnitskii (1981), p. 162). If we restrict x and y to the boundary of the ellipse then

$$\zeta = \zeta_k = \mathrm{e}^{\mathrm{i}\theta}. \tag{A 14}$$

We should note that Milne-Thomson assumes θ directed in a clockwise sense; hence, if we were to follow his notation, we would include a minus sign with iθ in (A 14).

For an infinite plate with an elliptical hole the transformation of boundary conditions (A 10) depend upon assumptions about the stress state at infinity. For finite tension at infinity, and the plate everywhere else unloaded and no net force resultants, the solution of the form

$$\Phi_k(z_k) = \sum_{n=1}^{\infty} A_{nk}\, \zeta_k^{-n} \tag{A 15}$$

can be shown to satisfy the equation of equilibrium (A 3) and the boundary conditions (A 10a, b). Coefficients A_{nk} can be evaluated by using the boundary conditions in the form (A 12a, b) with γ_n^x, γ_n^y evaluated, and consequently

$$\Phi_k(z_k) = (-1)^{k+1} \sum_{n=1}^{\infty} \zeta_k^{-n} (\gamma_{-n}^x \mu_{\substack{k+1 \\ \mathrm{mod}\,2}} - \gamma_{-n}^y)/(\mu_1 - \mu_2) \tag{A 16}$$

because

$$\mathrm{d}z_k/\mathrm{d}\zeta_k = [z_k^2 - (a_*^2 + \mu_k^2 b_*^2)]^{\frac{1}{2}}/\zeta_k, \tag{A 17}$$

then

$$\mathrm{d}z_k/\mathrm{d}\zeta_k \cdot \Phi_k'(z_k) = (-1)^k \sum_{n=1}^{\infty} n\zeta_k^{-(n+1)} (\gamma_{-n}^x - \mu_{\substack{k+1 \\ \mathrm{mod}\,2}}\, \gamma_{-n}^y)/(\mu_1 - \mu_2). \tag{A 18}$$

For tension of magnitude p at an angle ϕ from the x-axis as in figure 12, the background stress components are

$$\tau_{xx}^{\mathrm{bg}} = p\cos^2\phi, \quad \tau_{yy}^{\mathrm{bg}} = p\sin^2\phi, \tag{A 19a}$$

and

$$\tau_{xy}^{\mathrm{bg}} = p\sin\phi\cos\phi. \tag{A 19b}$$

Only the first terms in (A 16) and (A 18) are non-zero, and

$$\gamma_{-1}^{y} = -\tfrac{1}{2}p\sin\phi(a_*\sin\phi - \mathrm{i}b_*\cos\phi) \tag{A 20a}$$

and

$$\gamma_{-1}^{x} = \tfrac{1}{2}p\cos\phi(a_*\sin\phi - \mathrm{i}b_*\cos\phi). \tag{A 20b}$$

Substituting from (A 20a) into (A 18) and using the result in (A 9a) with the modification for background stress such that

$$\tau_{\mathrm{t}} = (\tau_{xx}+\tau_{xx}^{\mathrm{bg}})\,g_{\mathrm{t}x}^2 + (\tau_{yy}+\tau_{yy}^{\mathrm{bg}})\,g_{\mathrm{t}y}^2 + 2(\tau_{xy}+\tau_{xy}^{\mathrm{bg}})\,g_{\mathrm{t}x}\,g_{\mathrm{t}y} \tag{A 21}$$

results in

$$\tau_{\mathrm{t}} = 2\sin\phi/l^2\sum_{k=1}^{2}(-1)^{k+1}(\eta_k^{(1)}\eta_k^{(2)}+\eta_k^{(3)}\eta_k^{(4)})/[(\eta_k^{(2)})^2+(\eta_k^{(4)})^2]$$
$$+2/l^2\,[\tau_{xx}^{\mathrm{bg}}(a_*\sin\theta)^2+\tau_{yy}^{\mathrm{bg}}(b_*\cos\theta)^2-2a_*\,b_*\sin\theta\cos\theta\,\tau_{xy}^{\mathrm{bg}}], \tag{A 22}$$

where

$$\eta_k^{(1)} = -\beta_k\,a_*\sin\theta(\alpha_k\,a_*\sin\theta+b_*\cos\theta)\cdot[\cos\theta(a_*\cos\phi+\alpha_{\substack{k+1\\ \mathrm{mod}\,2}}\,a_*\sin\phi+\beta_{\substack{k+1\\ \mathrm{mod}\,2}}\,b_*\cos\phi)$$
$$+\sin\theta(a_*\beta_{\substack{k+1\\ \mathrm{mod}\,2}}\sin\phi-b_*\cos\phi\alpha_{\substack{k+1\\ \mathrm{mod}\,2}}-b_*\cos\phi\cot\phi)]$$
$$+\tfrac{1}{2}[(\alpha_k\,a_*\sin\theta+b_*\cos\theta)^2-(\beta_k\,a_*\sin\theta)^2]$$
$$\times[\sin\theta(a_*\cos\phi+\alpha_{\substack{k+1\\ \mathrm{mod}\,2}}\,a_*\sin\phi+b_*\beta_{\substack{k+1\\ \mathrm{mod}\,2}}\cos\phi)$$
$$-\cos\theta(a_*\beta_{\substack{k+1\\ \mathrm{mod}\,2}}\sin\phi-b_*\alpha_{\substack{k+1\\ \mathrm{mod}\,2}}\cos\phi-b_*\cos\phi\cot\phi), \tag{A 23a}$$

$$\eta_k^{(2)} = (a_*\sin\theta-\alpha_k\,b_*\cos\theta)\,(\alpha_1-\alpha_2)+\beta_k\,b_*\cos\theta(\beta_1-\beta_2), \tag{A 23b}$$

$$\eta_k^{(3)} = \beta_k\,a_*\sin\theta(\alpha_k\,a_*\sin\theta+b_*\cos\theta)\cdot[\sin\theta(a_*\cos\phi+\alpha_{\substack{k+1\\ \mathrm{mod}\,2}}\,a_*\sin\phi+b_*\beta_{\substack{k+1\\ \mathrm{mod}\,2}}\cos\phi)$$
$$-\cos\theta(a_*\beta_{\substack{k+1\\ \mathrm{mod}\,2}}\sin\phi-b_*\alpha_{\substack{k+1\\ \mathrm{mod}\,2}}\cos\phi-b_*\cos\phi\cot\phi]$$
$$+\tfrac{1}{2}[(\alpha_k\,a_*\sin\theta+b_*\cos\theta)^2-(\beta_k\,a_*\sin\theta)^2]$$
$$\times[\cos\theta(a_*\cos\phi+\alpha_{\substack{k+1\\ \mathrm{mod}\,2}}\,a_*\sin\phi+b_*\beta_{\substack{k+1\\ \mathrm{mod}\,2}}\cos\phi)$$
$$+\sin\theta(a_*\beta_{\substack{k+1\\ \mathrm{mod}\,2}}\sin\phi-b_*\alpha_{\substack{k+1\\ \mathrm{mod}\,2}}\cos\phi-b_*\cos\phi\cot\phi)], \tag{A 23c}$$

and

$$\eta_k^{(4)} = (a_*\sin\theta-\alpha_k\,b_*\cos\theta)\,(\beta_1-\beta_2)+\beta_k\,b_*\cos\theta(\alpha_1-\alpha_2). \tag{A 23d}$$

Equation (A 22) is plotted in figure 12. Comparisons of (A 22) with solutions given by Lekhnitskii (1968, figures 78, 80 and 81 therein) and Lekhnitskii (1981, figures 47–55 therein) verified (A 22) and aided in establishing resolution requirements for the finite-element solutions.

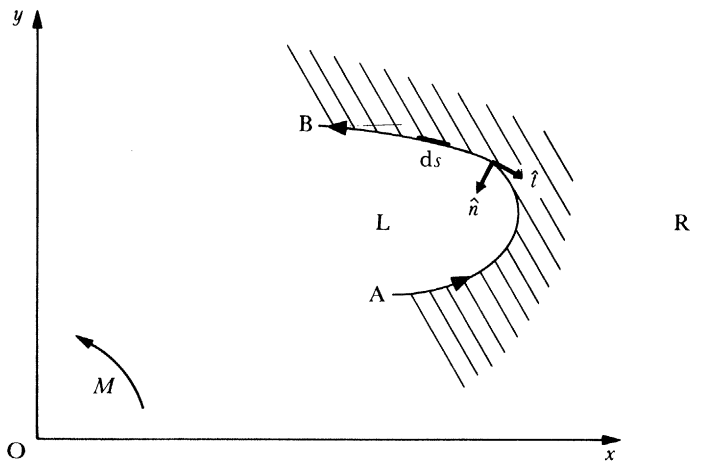

FIGURE A 1. Geometry of contact and vectorial representation for the analytical boundary-value problem solved for an elliptical inclusion (see text of Appendix for discussion).

Solution for the rotational response of a rigid elliptical inclusion subjected to pure twisting moment M_{zx}

We now consider the planar plate discussed above when subjected to a twisting moment of magnitude M_{zx} with a perfectly rigid inclusion welded into the elliptical cutout. The interface between the elastic plate and rigid inclusion is assumed to be non-dislocational. If the plate is considered to be of finite dimension and the moment M_{zx} is distributed along its vertical edges, then an equivalent concentrated moment M occurring at the centre of the rigid inclusion can be considered for the purpose of relating the total rigid rotational response ϵ_{R} and the driving twist M_{zx}. The relation will involve the compliances of the plate and all geometrical factors (a_*, b_* and ϕ^{e}).

Consider the moment M about O due to the contact of material in region R with L on the surface from A to B in figure A 1. The moment of L due to R is

$$M = \mathrm{Re} \int_{\mathrm{AB}} -2z \frac{\mathrm{d}}{\mathrm{d}s} \left(\frac{\partial F}{\partial z} \right) \mathrm{d}s \tag{A 24}$$

(Milne-Thomson 1968, pp. 8 and 180). For a pure twist and a closed loop C along ds,

$$M = \mathrm{Re}\,[F_k(z_k)]_C. \tag{A 25}$$

In (A 25), and henceforth, the subscript k implies sum, as written explicitly in equations (A 5). The bracket $[\ldots]_C$ indicates the closed circuit C on all implied integration. Equation (A 25) neglects terms involving Φ_k explicitly because these can be shown to be zero over closed circuit C for pure twist.

The displacement condition at the interface of L with R is that of small rigid rotation through angle ϵ_{R}. In terms of the reciprocal complex transform variable, ζ, a convenient combination of x and y components of boundary displacement, u_{b} and v_{b} respectively, is

$$^*u_{\mathrm{b}} = u_{\mathrm{b}} + \mathrm{i}v_{\mathrm{b}} = (\mathrm{i}\tfrac{1}{2}\epsilon_{\mathrm{R}})\,[(a_* + b_*)\,\zeta + (a_* - b_*)/\zeta]. \tag{A 26}$$

Since the interface is non-dislocational we can use (A 5e,f) and (A 26) to write

$$\begin{aligned} 2\,\mathrm{Re}\,(p_k\,\Phi_k) + \mathrm{i}2\,\mathrm{Re}\,(q_k\,\Phi_k) &= {}^*p_k\,\Phi_k + {}^*\bar{q}_k\,\bar{\Phi}_k \\ &= (\mathrm{i}\tfrac{1}{2}\epsilon_{\mathrm{R}})\,[(a_* + b_*)\,\sigma + (a_* - b_*)/\sigma], \end{aligned} \tag{A 27}$$

where σ is the value of ζ evaluated at the interface (see A 14),

$$*p_k \equiv p_k + \mathrm{i}q_k, \quad *q_k \equiv p_k - \mathrm{i}q_k, \tag{A 28}$$

and $(\overline{\ldots})$ indicates complex conjugate. Multiplying (A 27) by $\mathrm{d}\sigma/[2\pi\mathrm{i}\ (\sigma - *\zeta)]$ (with $*\zeta$ indicating either ζ_1 or ζ_2) yields

$$*p_k\, \Phi_k(z_k) = 2\mathrm{i}\ \epsilon_{\mathrm{R}}(a_* - b_*)/*\zeta. \tag{A 29a}$$

Performing the same multiplication and integration on the complex conjugate of (A 27) yields

$$*q_k\, \Phi_k(z_k) = -2\mathrm{i}\epsilon_{\mathrm{R}}(a_* + b_*)/*\zeta, \tag{A 29b}$$

$*\zeta$ lying outside the loop so that Cauchy's integral formula applies (see Milne-Thomson 1968, p. 56). This last step embodies the essential difference between the treatment of boundary conditions by Lekhnitskii (1968, 1981) and that used by Milne–Thomson (1968). The latter author essentially uses the Hilbert transform while the former uses a Fourier expansion and direct integration.

Finally, to construct the moment M (see A 25) we must (i) solve for $\boldsymbol{\Phi}_k$ in terms of $*\zeta$ from (A 29a, b), and (ii) use the differential relation (A 17) and perform the integrals $\int \boldsymbol{\Phi}_1(\mathrm{d}z_1/\mathrm{d}\zeta_1)\,\mathrm{d}\zeta_1$ and $\int \boldsymbol{\Phi}_2(\mathrm{d}z_2/\mathrm{d}\zeta_2)\,\mathrm{d}\zeta_2$. Consequently, (A 25) is

$$M = \epsilon_{\mathrm{R}}\pi\ \mathrm{Re}\{(a_* - \mathrm{i}\mu_k b_*)\,[*p_k(a_* + b_*) + *q_k(a_* - b_*)]/[*p_{\substack{k+1 \\ \mathrm{mod}\ 2}}\, *q_k - *p_k\, *q_{\substack{k+1 \\ \mathrm{mod}\ 2}}]\}, \tag{A 30}$$

which then defines Υ in (9) and represents the analytical results plotted in figures 17 and 18.

For the case $\phi^{\mathrm{e}} = 0°$,

$$\begin{aligned}\Upsilon = {} & [a_{12}(a_{12} + a_{11}\beta_1\beta_2)\,(\beta_2 - \beta_1) + a_{11}a_{22}(\beta_1^2/\beta_2 - \beta_2^2/\beta_1) \\ & + a_{22}a_{12}(1/\beta_1 - 1/\beta_2)]/[(a_*^2\, a_{11}(\beta_1^2 - \beta_2^2) + a_*\, b_*(\beta_1 - \beta_2)\,(a_{11}\beta_1\beta_2 + 2a_{12}) \\ & - a_*\, b_*\, a_{22}(1/\beta_1 - 1/\beta_2) + b_*^2\, a_{22}(\beta_1/\beta_2 - \beta_2/\beta_1)],\end{aligned} \tag{A 31}$$

which reduces the form given in (12) when $a_{11} \approx a_{22}$ and $\beta_1 \gg \beta_2$.

Solution for pure shear applied at infinity in a non-orthotropic plate with an elliptical non-orthotropic inclusion

We now consider the case when the inclusion discussed above is a non-orthotropic material with compliances a'_{11}, a'_{22}, a'_{12}, a'_{66}, a'_{16} and a'_{26}. The elliptical inclusion may therefore represent the effective multiple fault anisotropy considered in §8 where parallel two-dimensional faults are arbitrarily oriented with respect to both the coordinate frame, and the ellipse axes and/or the surrounding faulted media. Again, the plate is of infinite extent. The plate is subjected to a uniform background stress field of magnitudes τ_{xx}^{bg} and τ_{yy}^{bg}. The outline to obtain the solution for the stress field near the elastic inclusion follows the development of Lekhnitskii (1954).

We consider the case when stresses, τ'_{xx}, τ'_{yy} and τ'_{xy} interior to the elliptical inclusion are spatially homogeneous. Finite-element solutions demonstrate this approximation to be an adequate assumption *ab initio*. The values of these spatially homogeneous stresses denoted by τ'_{xx}, τ'_{yy} and τ'_{xy} are not, however, given *a priori*. Their values are to be determined together with the rigid rotational response of the inclusion, ϵ_{R}, as a part of the solution to the boundary-value problem.

The x and y components of displacements within the inclusion may be written in terms of the stresses by simple integration of the constitutive relation resulting in

$$u' = (a'_{11}\tau'_{xx} + a'_{12}\tau'_{yy} + a'_{16}\tau'_{xy})\,x - \epsilon_R\,y \qquad \text{(A 32}a\text{)}$$

and

$$v' = (a'_{16}\tau'_{xx} + a'_{26}\tau'_{yy} + a'_{66}\tau'_{xy})\,x + (a'_{12}\tau'_{xx} + a'_{22}\tau'_{yy} + a'_{26}\tau'_{xy})\,y + \epsilon_R\,x. \qquad \text{(A 32}b\text{)}$$

Similarly, the x and y displacements in the surrounding material due to the background stresses are

$$u^0 = (a_{11}\tau^{bg}_{xx} + a_{12}\tau^{bg}_{yy})\,x \qquad \text{(A 32}c\text{)}$$

and

$$v^0 = (a_{16}\tau^{bg}_{xx} + a_{26}\tau^{bg}_{yy})\,x + (a_{12}\tau^{bg}_{xx} + a_{22}\tau^{bg}_{yy})\,y.$$

The traction normal to the surface of contact may be divided into x and y components, X_n and Y_n respectively. We shall assume that the boundary between the two materials is non-dislocational. Continuity of stress along the interface (see figure A 1) demands that

$$X_n = -X'_n \qquad \text{(A 33}a\text{)}$$

and

$$Y_n = -Y'_n, \qquad \text{(A 33}b\text{)}$$

where the primed and unprimed components represent inclusion and surroundings respectively. Continuity of displacement demands that

$$u = u', \qquad \text{(A 33}c\text{)}$$

and

$$v = v'. \qquad \text{(A 33}d\text{)}$$

When $\tau^{bg}_{xy} = 0$, integration of the traction conditions (A 33a, b) about a closed circuit C yields;

$$2\,\mathrm{Re}\sum_{k=1}^{2} \Phi_k(z_k) = (\tau'_{yy} - \tau^{bg}_{yy})\,x - \tau'_{xy}\,y, \qquad \text{(A 34}a\text{)}$$

$$2\,\mathrm{Re}\sum_{k=1}^{2} \mu_k\,\Phi_k(z_k) = (\tau'_{xx} - \tau^{bg}_{xx})\,y - \tau'_{xy}\,x, \qquad \text{(A 34}b\text{)}$$

respectively (see (A 10a, b)). The displacement conditions (A 33a, b) are transformed to the complex variable z_k by a similar integration procedure and yields

$$2\,\mathrm{Re}\sum_{k=1}^{2} p_k\,\Phi_k(z_k) = u' - u^0, \qquad \text{(A 34}c\text{)}$$

$$2\,\mathrm{Re}\sum_{k=1}^{2} q_k\,\Phi_k(z_k) = v' - v^0, \qquad \text{(A 34}d\text{)}$$

where on the r.h.s. of (A 34c, d) we use the explicit forms of u', u^0, v', v^0 as in expressions (A 32a–d). The complex integrations may be reconstructed in detail by referring to chapter 7 of the monograph by Milne-Thomson (1968).

We now seek an expression for $\Phi_k(z_k)$ to be evaluated at $\zeta_k = e^{i\theta}$. For a plate with an elliptical hole we know that the solution for the homogeneous problem for $\Phi_k(z_k)$ is of the form

$$\Phi_k(z_k) = \omega_k/\zeta_k \qquad \text{(A 35)}$$

(see (A 15)). This homogeneous form must satisfy the traction conditions at the boundary of

contact between the elliptical inclusion and the surrounding medium. Using (A 34*a*, *b*), then, we can write

$$2\sum_{k=1}^{2}\omega_k = (\tau'_{yy}-\tau^{\mathrm{bg}}_{yy})\,a_*-\mathrm{i}\tau'_{xy}\,b_* \tag{A 36a}$$

and

$$2\sum_{k=1}^{2}\mu_k\,\omega_k = \mathrm{i}(\tau'_{xx}-\tau^{\mathrm{bg}}_{xx})\,b_*-\tau'_{xy}\,a_*. \tag{A 36b}$$

We must solve for both real and imaginary parts of ω_k, so similar equations hold for the complex conjugates of (A 36).

The two solutions for $k = 1, 2$ may be written as

$$2(\mu_1-\mu_2)\,\omega_k = (-1)^{k+1}\,[(\tau'_{xx}-\tau^{\mathrm{bg}}_{xx})\,\mathrm{i}b_*-(\tau'_{yy}-\tau^{\mathrm{bg}}_{yy})\,a_*\,\mu_{\substack{k+1\\ \mathrm{mod}\,2}}+\tau'_{xy}(\mathrm{i}b_*\,\mu_{\substack{k+1\\ \mathrm{mod}\,2}}-a_*)]. \tag{A 37}$$

To complete the solution we need only solve for the unknowns τ'_{xx}, τ'_{yy}, τ'_{xy} and the rigid rotation of the inclusion ϵ_{R}. Incorporating the two solutions represented by (A 35) together with (A 37) into (A 34*a–d*) we reduce the remaining work to solving a set of four complex algebraic equations for the real constants τ'_{xx}, τ'_{yy}, τ'_{xy} and ϵ_{R}.

Stress components may be recovered by noting that

$$\Phi'_k(z_k) = -\omega_k/(\zeta_k\,s_k) \tag{A 38}$$

with

$$s_k = (z_k^2-a_*^2-\mu_k^2\,b_*^2)^{\frac{1}{2}}.$$

The final step for the analytical solution is then to solve

$$\boldsymbol{M}\boldsymbol{S}^{\mathrm{int}} = \boldsymbol{S}^{\mathrm{ext}}, \tag{A 39}$$

where $\boldsymbol{S}^{\mathrm{int}}$ are interior unknown constants and $\boldsymbol{S}^{\mathrm{ext}}$ is formed solely from background stresses and material properties of the surrounding medium. The boundary condition matrix operator $\boldsymbol{M}$ is written explicitly as

$$\boldsymbol{M} = \begin{bmatrix} \mathrm{i}\delta^p_\mu/c-a'_{11} & \delta^{p\mu}_\mu-a'_{12} & -(\delta^p_\mu+\mathrm{i}\delta^{p\mu}_\mu/c+a'_{16}) & -\mathrm{i}/c \\ \mathrm{i}(\delta^q_\mu-a'_{12})/c-a'_{16} & \delta^{q\mu}_\mu-\mathrm{i}a'_{22}/c-a'_{26} & -(\delta^q_\mu+\mathrm{i}\delta^{q\mu}_\mu/c+a'_{66}+\mathrm{i}a'_{26}/c) & 1 \\ -\mathrm{i}\delta^p_\mu/c-a'_{11} & \delta^{p\mu}_\mu-a'_{12} & -(\delta^p_\mu-\mathrm{i}\delta^{p\mu}_\mu/c+a'_{16}) & \mathrm{i}/c \\ -\mathrm{i}(\delta^q_\mu-a'_{12})/c-a'_{16} & \delta^{q\mu}_\mu+\mathrm{i}a'_{22}/c-a'_{26} & -(\delta^q_\mu-\mathrm{i}\delta^{q\mu}_\mu/c+a'_{66}-\mathrm{i}a'_{26}/c) & 1 \end{bmatrix} \tag{A 40a}$$

and the four-vectors $\boldsymbol{S}^{\mathrm{int}}$ and $\boldsymbol{S}^{\mathrm{ext}}$ as

$$\boldsymbol{S}^{\mathrm{int}} = \begin{bmatrix} \tau'_{xx} \\ \tau'_{yy} \\ \tau'_{xy} \\ \epsilon_{\mathrm{R}} \end{bmatrix} \tag{A 40b}$$

and

$$\boldsymbol{S}^{\mathrm{ext}} = \begin{bmatrix} \tau^{\mathrm{bg}}_{xx}(\mathrm{i}\delta^p_\mu/c-a_{11})+\tau^{\mathrm{bg}}_{yy}(\delta^{p\mu}_\mu-a_{12}) \\ \tau^{\mathrm{bg}}_{xx}(\mathrm{i}\delta^q_\mu/c-\mathrm{i}a_{12}/c-a_{16})+\tau^{\mathrm{bg}}_{yy}(\delta^{\mu q}_\mu-\mathrm{i}a_{22}/c-a_{26}) \\ \tau^{\mathrm{bg}}_{xx}(-\mathrm{i}\delta^p_\mu/c-a_{11})+\tau^{\mathrm{bg}}_{yy}(\delta^{p\mu}_\mu-a_{12}) \\ \tau^{\mathrm{bg}}_{xx}(-\mathrm{i}\delta^q_\mu/c+\mathrm{i}a_{12}/c-a_{16})+\tau^{\mathrm{bg}}_{yy}(\delta^{\mu q}_\mu+\mathrm{i}a_{22}/c-a_{26}) \end{bmatrix}, \tag{A 40c}$$

introducing the complex constants

$$\delta_\mu^p \equiv (p_1 - p_2)/(\mu_1 - \mu_2),$$
$$\delta_\mu^q \equiv (q_1 - q_2)/(\mu_1 - \mu_2),$$
$$\delta_\mu^{q\mu} \equiv (\mu_1 q_2 - \mu_2 q_1)/(\mu_1 - \mu_2)$$

and

$$\delta_\mu^{p\mu} \equiv (\mu_1 p_2 - \mu_2 p_1)/(\mu_1 - \mu_2),$$

which depend upon the elastic properties of the surrounding medium and the real constant $c \equiv a_*/b_*$. When $\tau_{yy}^{bg} = -\tau_{xx}^{bg}$ the background stress corresponds to that of pure shear.

Notation

symbol	description	units
C^{ijrs}	fourth-rank tensor of stiffness coefficients	MPa (1MPa = 10^6 N m^{-2})
A^{ijrs}	fourth-rank tensor of compliance coefficients	MPa^{-1}
c_{pq}	the pq stiffness	MPa
a_{pq}	the pq compliance	MPa^{-1}
$\partial \bar{x}_k/\partial x_i$	rotation matrix	—
$\bar{a}_{pq}$	the pq compliance with respect to a rotated frame	MPa
ϵ^{ij}	strain tensor	—
τ_{ij}	stress tensor	MPa
τ_{pq}	stress component $p, q = 1, 2, 3$ (or $p, q = x, y$ for elliptical inclusion exterior of §8 and Appendix A)	—
ϵ_{pq}	strain component $p, q = 1, 2, 3$ (or $p, q = x, y$ for elliptical inclusion exterior of §8 and Appendix A)	—
τ_{qq}^p	the qth principal stress	MPa
ϵ_{qq}^p	the qth principal strain	—
τ'_{pq}	stress components of elliptical inclusion interior	MPa
a'_{pq}	the pq compliance of elliptical inclusion interior	MPa^{-1}
τ_{pq}^{bg}	background stress component applied at infinity	MPa
$\mu^{(1,2)}$	isotropic shear moduli for laminate components: 1, 2	MPa
$\lambda^{(1,2)}$	isotropic first Lamé constants for laminate components: 1, 2	MPa
$K^{(1,2)}$	isotropic bulk compressiblities for laminate components: 1, 2	MPa
d	distance between similar sides of like components in periodic laminate	m
a	laminate fraction occupied by weak component (1)	—
b	laminate fraction occupied by strong component (2)	—
ν	Poisson's ratio in any plane whose normal is a transverse isotropy axis	—
ν_p	Poisson's ratio normal to any plane whose normal is a transverse isotropy axis	—

G	shear modulus in any plane whose normal is a transverse isotropy axis	MPa
G_p	shear modulus normal to any plane whose normal is a transverse isotropy axis	MPa
E	Young's modulus in any plane whose normal is a transverse isotropy axis	MPa
E_p	Young's modulus normal to any plane whose normal is a transverse isotropy axis	MPa
ν_0	isotropic Poisson's ratio for crustal bedrock	—
E_0	isotropic Young's modulus for crustal bedrock	MPa
G_0	isotropic shear modulus for crustal bedrock	MPa
ψ^e	90° − dip	degrees
ϕ^e	strike	degrees
$\phi^{e'}$	strike of faults within elliptical inclusion	degrees
ϵ_R	magnitude of clockwise rigid rotational motion	radians
M_{zx}	magnitude of concentrated clockwise rotational twisting moment	N
a_*	half-length of major axis of elliptical inclusion	m
b_*	half-length of minor axis of elliptical inclusion	m
$E_{\frac{1}{4}\pi}$	Young's modulus at maximum weakening direction for crack anisotropy	MPa
J_2'	second deviatoric stress invariant	MPa
I_2'	second deviatoric strain invariant	—
Δ	cubical dilatation	—
L	Biot's slide modulus (or ratio of weakened to isotropic shear moduli)	—
Λ	$1-L$	—
B_1^{I}	stress intensity coefficient for mode I crack deformation	—
B_1^{II}	stress intensity coefficients for mode II crack deformation	—
α	half length of an unlocked fault segment	m
β	distance between adjacent collinear fault segments	m
δ	distance between collinear fault segment centres	m
A	total areal extent of reference crust (crack model)	m^2
A_d	areal density of cracks	m^{-2}
H_c	total collinear length scale of reference crust (crack model)	m
H	total orthogonal length scale of reference crust (crack model)	m
N_c	number of collinear cracks in reference crust (crack model)	—
N	number of parallel collinear crack sets in reference crust (crack model)	—

References

Agnew, D. C. & Sieh, K. E. 1978 A documentary study of the felt effects of the great California earthquake, of 1857. *Bull. seism. Soc. Am.* **68**, 1711–1725.

Aki, K. 1979 Characteristics of barriers on an earthquake fault. *J. geophys. Res.* **84**, 6140–6148.

Aki, K. 1982 Three-dimensional seismic inhomogeneities in the lithosphere and asthenosphere: Evidence for decoupling in the lithosphere and flow in the asthenosphere. *Rev. Geophys. Space Phys.* **20**, 161–170.

Allen, C. R., St Amand, P., Richter, C. F. & Nordquist, J. M. 1965 Relationship between seismicity and geologic structure in the southern California region. *Bul. seism. Soc. Am.* **55**, 753–797.

Allison, M. L., Whitcomb, J. A., Cheatum, C. E. & McEuen, R. B. 1978 Elsinore fault seismicity: The September 13, 1983, Agua Calente Springs, California, earthquake series. *Bul. seism. Soc. Am.* **68**, 429–440.

Backus, G. E. 1962 Long-wave elastic anisotropy produced by horizontal layering. *J. geophys. Res.* **67**, 4427–4440.

Baird, A. K., Morton, O. M., Woodford, A. O. & Baird, K. W. 1974 Transverse Ranges province: A unique structural–petrochemical belt across the San Andreas fault system. *Bull. geol. Soc. Am.* **85**, 163–174.

Baird, A. K. & Miesch, A. T. 1984 Chemical variation in source materials for the batholithic rocks of southern California. *U.S.G.S. prof. Pap. no.* 1284, pp. 1–42.

Barenblatt, E. I., Keilis-Borok, V. I. & Vishik, M. M. 1981 Model of clustering of earthquakes. *Proc. natn. Acad. Sci. U.S.A.* **78**, 5284–5287.

Bilby, B. A. & Eshelby, J. D. 1968 Dislocations and theory of fracture. In *Fracture: an advanced treatise* (ed. H. Liebowitz), vol. 1, pp. 99–182. New York: Academic Press.

Biot, M. A. 1965 *Mechanics of incremental deformations.* (504 pages.) New York: Wiley.

Bird, P. & Baumgardner, J. 1984 Fault friction, regional stress, and crust–mantle coupling in southern California from finite element models. *J. geophys. Res.* **89**, 1932–1944.

Bird, P. & Piper, K. 1980 Plane–stress finite element models of tectonic flow in southern California. *Phys. Earth planet. Inter.* **21**, 158–175.

Bird, P. & Rosenstock, R. W. 1984 Kinematics of present crust and mantle flow in southern California. *Bull. geol. Soc. Am.* **95**, 946–957.

Briggs, P., Press, F. & Guberman, Sh. A. 1977 Pattern recognition applied to earthquake epicenters in California and Nevada. *Bull. geol. Soc. Am.* **88**, 161–173.

Bruggeman, D. A. G. 1937 Berechnung verschiedener physikalischer Konstanten von heterogenen Substanzen. III. Die elastischen Konstanten der quasiisotropen Mirschkörper aus isotropen Substanzen. *Annln Phys.* **29**, 160–178.

Budiansky, B. & O'Connell, R. J. 1976 Elastic moduli of a cracked solid. *Int. J. Solids Struct.* **12**, 81–97.

Burk, C. A. & Moores, E. M. 1968 Problems of major faulting at continental margins with special reference to the San Andreas fault system. In *Conference on Geologic Problems of the San Andreas Fault System* (*Stanford Univ. Publ. geol. Sci.* no. 11), pp. 358–374.

Byerlee, J. D. 1978 Friction of rocks. *Pure appl. Geophys.* **116**, 615–626.

Chinnery, M. A. 1963 The stress changes that accompany strike-slip faulting. *Bull. seism. Soc. Am.* **53**, 921–932.

Chinnery, M. A. 1964 The strength of the Earth's crust under horizontal shear stress. *J. geophys. Res.* **69**, 2085–2089.

Chinnery, M. A. 1966 Secondary faulting: I. Theoretical aspects. *Can. J. Earth Sci.*, **3**, 163–174.

Christensen, M. N. 1966 Late Cenozoic crustal movement in the Sierra Nevada of California. *Bull. geol. Soc. Am.* **77**, 163–183.

Christie, J. M. & Ord, A. 1980 Flow stress from microstructures of mylonites: Example and current assessment. *J. geophys. Res.* **85**, 6253–6262.

Corbett, E. J. & Johnson, C. E. 1982 The Santa Barbara, California earthquake of 13 August 1978. *Bull. seism. Soc. Am.* **72**, 2201–2226.

Crouch, J. K. 1979 Neogene tectonic evolution of the western Transverse Ranges and the California continental borderland. *Bull. geol. Soc. Am.* **90**, 338–349.

Crowell, J. C. 1952 Lateral displacement on the San Gabriel fault, southern California. *Bull. geol. Soc. Am.* **63**, 1241–1242.

Crowell, J. C. 1976 Implications of crustal stretching and shortening of coastal Ventura Basin. *Pacific Section, Am. Assoc. Petrol. Geol. Misc. Publ.* no. 24, pp. 365–382.

Crowell, J. C. 1981 An outline of the tectonic history of southeastern California. In *The geotectonic development of California* (ed. W. G. Ernst), pp. 582–600. Englewood Cliffs, N.J.: Prentice-Hall.

Cummings, D. 1976 Theory of plasticity applied to faulting, Mojave Desert, southern California. *Bull. geol. Soc. Am.* **87**, 720–724.

Davis, G. A. 1980 Problems of intraplate extensional tectonics, western United States. In *Continental tectonics*, pp. 84–95. Washington, D.C.: National Academy of Sciences.

Delameter, W. R., Herrmann, G. & Barnett, D. M. 1975 Weakening of an elastic solid by rectangular array of cracks. *J. appl. Mech.* **47**, 74–80.

Dibblee, T. W. 1976 The Rinconada and related faults in the Southern Coast Ranges, California, and their tectonic significance. *U.S. geol. Surv. prof. Paper.* no. 981, pp. 1–55.

PHILOSOPHICAL TRANSACTIONS OF THE ROYAL SOCIETY A MATHEMATICAL, PHYSICAL & ENGINEERING SCIENCES

Dickinson, W. R. 1981 Plate tectonics and the continental margin of California. In *The geotectonic development of California* (ed. W. G. Ernst), pp. 1–28. Englewood Cliffs, N.J.: Prentice-Hall.

Dokka, R. K. 1983 Displacement on late Cenozoic strike-slip faults of the central Mojave Desert, California. *Geology* **11**, 305–308.

Ebel, J. E. & Helmberger, D. V. 1982 *P*-wave complexity and fault asperities: The Borrego Mountain, California, earthquake of 1968. *Bull. seism. Soc. Am.* **72**, 413–437.

England, P. & McKenzie, D. P. 1982 A thin viscous sheet model for continental deformation. *Geophys. Jl. R. astr. Soc.* **70**, 295–321.

Ergas, R. A. & Jackson, D. D. 1981 Spatial variation of crustal seismic velocities in southern California. *Bull. seism. Soc. Am.* **71**, 1849–1861.

Eubanks, R. A. & Sternberg, E. 1954 On the axisymmetric problem of elasticity theory for a medium with transverse isotropy. *J. rat. Mech. Analysis.* **3**, 89–101.

Fleitout, L. & Froidevaux, C. 1982 Tectonics and topography for a lithosphere containing density heterogeneities. *Tectonics*, **1**, 21–56.

Freudenthal, A. M. & Geiringer, H. 1958 The mathematical theories of the anelastic continuum. In *Handbuch der Physik* (ed. S. Flugge), vol. 6, pp. 229–433. Berlin: Springer-Verlag.

Froidevaux, C., Schubert, G. & Yuen, D. A. 1977 Thermal and mechanical structure of the upper mantle: A comparison between continental and oceanic models. *Tectonophysics* **37**, 233–246.

Garfunkel, Z. 1974 Model for the late Cenozoic tectonic history of the Mojave Desert, California, and for its relation to adjacent regions. *Bull. geol. Soc. Am.* **85**, 1931–1944.

Gawthrop, W. 1978 The 1927 Lompoc, California earthquake. *Bull. seism. Soc. Am.* **68**, 1705–1716.

Graham, S. A. & Dickinson, W. R. 1978 Evidence for 115 kilometers of right slip on the San Gregorio–Hosgri fault trend. *Science, Wash.* **199**, 179–181.

Green, A. E. & Taylor, G. I. 1939 Stress systems in aeolotropic plates. I. *Proc. R. Soc. Lond.* A **173**, 162–172.

Gurtin, M. E. 1972 The linear theory of elasticity. In *Handbuch der Physik* (ed. C. Truesdell) vol. 6 (*Mechanics of Solids II*), pp. 1–295. Berlin: Springer–Verlag.

Hadley, D. & Kanamori, H. 1977 Seismic structure of the Transverse Ranges, California. *Bull. geol. Soc. Am.* **88**, 1469–1478.

Hall, C. A. 1981*a* San Luis Obispo transform fault and middle Miocene rotation of the western Transverse Ranges, California. *J. geophys. Res.* **86**, 1015–1031.

Hall, C. A. 1981*b* Evolution of the western Transverse Ranges microplate: Late Cenozoic faulting and basinal development. In *The geotectonic development of California* (ed. W. G. Ernst), pp. 559–582. Englewood Cliffs, N.J.: Prentice–Hall.

Hamilton, W. 1978 Mesozoic tectonics of the Western U.S. In *Mesozoic Paleogeography of the Western United States* (*Pacific Coast Paleogeography Symposium* no. 2) (ed. D. G. Howell & K. A. McDougal), pp. 30–70. Los Angeles: Society of Economic Paleontologists and Minerologists.

Hartzell, S. & Brune, J. N. 1979 The Horse Canyon earthquake of August 2, 1975 – two stage stress-release process in a strike-slip earthquake. *Bull. seism. Soc. Am.* **69**, 1161–1173.

Helbig, K. 1958 Elastische Wellen in anisotropen Medien. *Beitr. Geophys.* **67**, 256–288.

Hill, D. P. 1982 Contemporary block tectonics: California and Nevada. *J. geophys. Res.* **87**, 5433–5450.

Humphreys, E., Clayton, R. W. & Hager, B. H. 1984 A tomographic image of mantle structure beneath southern California. *Geophys. Res. Lett.* **11**, 625–627.

Kamerling, M. J. & Luyendyk, B. P. 1979 Tectonic rotations of the Santa Monica Mountains region, Western Transverse Ranges, California, suggested by paleomagnetic vector. *Bull. geol. Soc. Am.* **90**, 331–337.

Kasahara, A. 1981 *Earthquake mechanics.* (293 pages.) Cambridge University Press.

Koide, H. & Bhattacharji, S. 1977 Geometric patterns of active faults and their significance as indicators for areas of energy release. In *Energetics of geological processes* (ed. S. K. Saxena), pp. 46–66. New York: Springer-Verlag.

Lachenbruch, A. H. & Sass, J. H. 1980 Heat flow and energetics of the San Andreas Fault zone. *J. geophys. Res.* **85**, 6185–6222.

Langston, C. A. 1978 The February 9, 1971 San Fernando Earthquake: A study of source finiteness in teleseismic body waves. *Bull. seism. Soc. Am.* **68**, 1–29.

Lekhnitskii, S. G. 1954 Stress distribution in an anisotropic plate with an elliptic elastic core (plane problem). [In Russian]. *Inzh. Sb.* **19**, 83–106.

Lekhnitskii, S. G. 1968 *Anisotropic plates* (translated from the 2nd Russian edition by S. W. Tsai & T. Cheron). (534 pages.) New York: Gordon & Breach.

Lekhnitskii, S. G. 1981 *Theory of elasticity of an anisotropic body* (430 pages.) Moscow: Mir Publishers.

Louie, J. N., Allen, C. R., Johnson, D. C., Haase, P. C. & Cohn, S. N. 1985 Fault slip in southern California. *Bull. seism. Soc. Am.* **75**, 811–833.

Luyendyk, B. P., Kamerling, M. J. & Terres, R. 1980 Geometrical model for Neogene crustal rotations in southern California. *Bull. geol. Soc. Am.* **91**, 211–217.

Lyzenga, G. A., Wallace, K. S., Raefsky, A., Groth, P. M. & Fanselow, J. L. 1986 Tectonic motions in California inferred from VLBI observations, 1980–1984. *J. geophys. Res.* (In the press.)

PHILOSOPHICAL TRANSACTIONS OF THE ROYAL SOCIETY A MATHEMATICAL, PHYSICAL & ENGINEERING SCIENCES

McGarr, A. 1980 Some constraints on levels of shear stress in the crust from observations and theory. *J. geophys. Res.* **85**, 6231–6238.
McGarr, A. 1982 Analysis of states of stress between provinces of constant stress *J. geophys. Res.* **87**, 9279–9288.
Mavko, G. M. 1981 Mechanics of motion on major faults. *A. Rev. Earth. planet. Sci.* **9**, 81–111.
Melosh, H. J. & Raefsky, A. 1981 A simple and efficient method for introducing faults into finite element computation. *Bull. seism. Soc. Am.* **71**, 1391–1400.
Milne-Thomson, L. M. 1968 *Plane elastic systems.* (211 pages.) Berlin: Springer-Verlag.
Minster, J. B. & Jordan, T. H. 1978 Present-day plate motions. *J. geophys. Res.* **83**, 5331–5354.
Morrow, C. A., Shi, L. Q. & Byerlee, J. D. 1982 Strain hardening and strength of clay-rich fault gouges. *J. geophys. Res.* **87**, 6771–6780.
Musman, A. 1982 Statistical tests of ARIES data. *J. geophys. Res.* **87**, 5553–5562.
Norris, R. M. & Webb, R. W. 1977 *Geology of California.* (365 pages.) New York: Wiley.
Novozhilov, V. V. 1961 *Theory of elasticity* (translated from the Russian by J. K. Lusher) (448 pages.) New York: Pergamon.
Oliver, H. W. 1980 Interpretation of the gravity map of California and its continental margin. *Calif. Div. Mines and Geol. Bull.* no. 205, pp. 1–52. Sacramento, California.
Page, B. M. 1981 The Southern Coast Ranges. In *The geotectonic development of California* (ed. W. G. Ernst), pp. 329–417. Englewood Cliffs, N.J.: Prentice-Hall.
Pechmann, J. C. 1983 The relationship of small earthquakes to strain accumulation along major faults in southern California. Ph.D. thesis, California Institute of Technology, Pasadena, California.
Plescia, J. B. & Henyey, T. L. 1982 Geophysical character of the proposed eastern extension of the Garlock fault and adjacent areas, eastern California. *Geology* **10**, 209–214.
Puente, I. & de la Peña, A. 1979 Geology of the Cerro Prieto geothermal field. *Geothermics* **8**, 155–175.
Raikes, S. A. 1980 Regional variations in upper mantle structure beneath southern California. *Geophys. Jl. R. astr. Soc.* **63**, 187–216.
Raleigh, C. B., Sieh, K. E., Sykes, L. R. & Anderson, D. L. 1982 Forecasting southern California earthquakes. *Science, Wash.* **217**, 1097–1104.
Rice, J. R. 1980 The mechanics of earthquake rupture. In *Proceedings of the International School of Physics, Enrico Fermi, Course* no. LXX VIII (ed. A. M. Dziewonski & E. Boschi), pp. 555–649. Amsterdam: North-Holland.
Rice, J. R., Rudnicki, J. W. & Simons, D. A. 1978 Deformation of spherical cavities and inclusion in fluid-infiltrated elastic materials. *Int. J. Solids Struct.* **14**, 289–303.
Richardson, R., Solomon, S. C. & Sleep, N. H. 1979 Tectonic stress in the plates. *Rev. Geophys. Space Phys.* **17**, 981–1019.
Rodgers, D. A. & Chinnery, M. A. 1973 Stress accumulation in the Transverse Ranges, southern California. In *Proceedings of the Conference on Tectonic Problems of the San Andreas Fault System, held at Stanford, California* (*Stanford Univ. Publ. geol. Sci.* **13**), pp. 70–79.
Rose, M. E. 1957 *Elementary theory of angular momentum.* (222 pages.) New York: Wiley.
Rudnicki, J. W. & Kanamori, H. 1981 Effects of fault interaction on moment, stress drop, and strain energy release. *J. geophys. Res.* **86**, 1785–1793.
Rundle, J. B. & Thatcher, W. 1980 Speculations on the nature of the southern California uplift. *Bull. seism. Soc. Am.* **70**, 1869–1886.
Sanders, C. O. & Kanamori, H. 1984 A seismotectonic analysis on the Anza seismic gap, San Jacinto fault zone, southern California. *J. geophys. Res.* **89**, 5873–5890.
Savage, J. C. 1978 Strain patterns and strain accumulation along plate margins. In *Applications of geodesy to geodynamics* (*Proc. 9th Geodesy/Solid Earth and Ocean Physics Research Conference*, 2–5 *Oct.* 1978), pp. 93–97. Ohio State University.
Sbar, M. L. 1982 Delineation and interpretation of seismotectonic domains in western North America. *J. geophys. Res.* **87**, 3919–3928.
Scheidegger, A. E. 1956 Forces in the Earth's crust. In *Handbuch der Physik* (ed. S. Flugge), vol. 47 (*Geophysics I*), pp. 258–287. Berlin: Springer-Verlag.
Scholz, C. H. 1977 Transform fault systems of California and New Zealand: similarities and their tectonic and seismic styles. *J. geol. Soc. Lond.* **133**, 215–299.
Seeber, L. 1983 Large scale thin-skin tectonics. *Rev. Geophys. Space Phys.* **21**, 1528–1538.
Sharp, R. V. 1981 Variable rates of late Quaternary strike slip on the San Jacinto fault zone, southern California. *J. geophys. Res.* **86**, 1754–1762.
Simpson, R. W. & Cox, A. 1977 Rotations in the Coast Ranges. *Geology* **5**, 585–589.
Singh, B. 1973 Continuum characterization of jointed rock masses, Part I. The constitutive equations. *Int. J. Rock Mech. Min. Sci.* **10**, 311–335.
Stauffer, P. H. 1967 Grain flow deposits and their implications, Santa Ynez Mountains, California. *J. sedim. Petrol.* **37**, 487–508.
Sylvester, A. G., Smith, S. W. & Scholz, C. H. 1970 Earthquake swarm in the Santa Barbara Channel, California, 1968. *Bull. seism. Soc. Am.* **60**, 1047–1060.

PHILOSOPHICAL TRANSACTIONS OF THE ROYAL SOCIETY A MATHEMATICAL, PHYSICAL & ENGINEERING SCIENCES

Sylvester, A. G. & Smith, R. R. 1976 Tectonic transpression and basement-controlled deformation in San Andreas fault zone, Salton Trough, California. *Bull. Am. Ass. Petrol. Geol.* **60**, 2012–2018.

Sylvester, A. G. & Darrow, A. C. 1979 Structure and neotectonics of the Western Santa Ynez fault system in southern California. *Tectonophysics* **52**, 389–405.

Tchalenko, J. S. 1970 Similarities between shear zones of different magnitudes. *Bull. geol. Soc. Am.* **81**, 1625–1640.

Tsuboi, C. 1956 Earthquake energy, earthquake volume aftershock area, and strength of the Earth's crust. *J. Phys. Earth* **4**, 63–66.

Turcotte, D. L. & Schubert, G. 1982 *Geodynamics: applications of continuum physics to geological problems.* (608 pages.) New York: Wiley.

Veeder, J. G. & Brown, R. D. 1968 Structure and stratigraphic relations along the Nacimento fault in the southern Santa Lucia Range and San Rafael Mountains, California. In *Conference on Geological Problems of the San Andreas Fault System* (*Stanford University Publ. geol. Sci.* no. 11), pp. 242–259.

Walck, M. C. & Minister, J. B. 1982 Relative array analysis of upper mantle lateral velocity variations in southern California. *J. geophys. Res.* **87**, 1757–1772.

Wallace, T. C., Helmberger, D. V. & Ebel, J. E. 1981 A broadband study of the 13 August 1978 Santa Barbara earthquake. *Bull seism. Soc. Am.* **70**, 1869–1886.

Walpole, L. J. 1981 Elastic behaviour of composite materials: Theoretical foundations. *Adv. appl. Mech.* **21**, 169–242.

Walsh, J. B. & Grosenbaugh, M. A. 1979 A new model for analyzing the effect of fractures on compressiblity. *J. geophys. Res.* **84**, 3532–3536.

Whitcomb, J. H., Allen, C. R., Garmany, J. D. & Hileman, J. A. 1973 San Fernando earthquake series, 1971: Focal mechanisms and tectonics. *Rev. Geophys. Space Phys.* **11**, 693–730.

Wilcox, R. E., Harding, T. P. & Seely, D. R. 1973 Basic wrench tectonics. *Bull. Am. Ass. Petrol. Geol.* **57**, 74–96.

Yeats, R. S. 1981 Quaternary flake tectonics of the California Transverse Ranges. *Geology* **9**, 16–20.

Yeats, R. S. 1983 Large-scale Quaternary detachments in Ventura Basin, southern California. *J. geophys. Res.* **88**, 569–583.

Yeats, R. S., Cole, M. R., Mershat, W. R. & Parsley, R. M. 1974 Poway fan submarine cone and rifting of the inner southern California borderland. *Bull. geol. Soc. Am.* **85**, 293–302.

Yerkes, R. F. & Lee, W. H. K. 1979 Late Quaternary deformation in the western Transverse Ranges, California. *U.S. geol. Surv. Circ.* no. 799-B, pp. 1–11.

Yerkes, R. F., Greene, H. G., Tinsley, J. C. & Lajoie, K. R. 1981 Seismotectonic setting of the Santa Barbara Channel area, southern California. Text accompanying *U.S. geol Surv. map no. MF*-1169. (25 pages.) Department of Interior, U.S. Geological Survey.

Zoback, M. L. & Zoback, M. 1980*a* Faulting patterns in north-central Nevada and strength of the crust. *J. geophys. Res.* **85**, 275–284.

Zoback, M. L. & Zoback, M. 1980*b* State of stress in the conterminous United States. *J. geophys. Res.* **85**, 6113–6156.

PHILOSOPHICAL TRANSACTIONS OF THE ROYAL SOCIETY A MATHEMATICAL, PHYSICAL & ENGINEERING SCIENCES

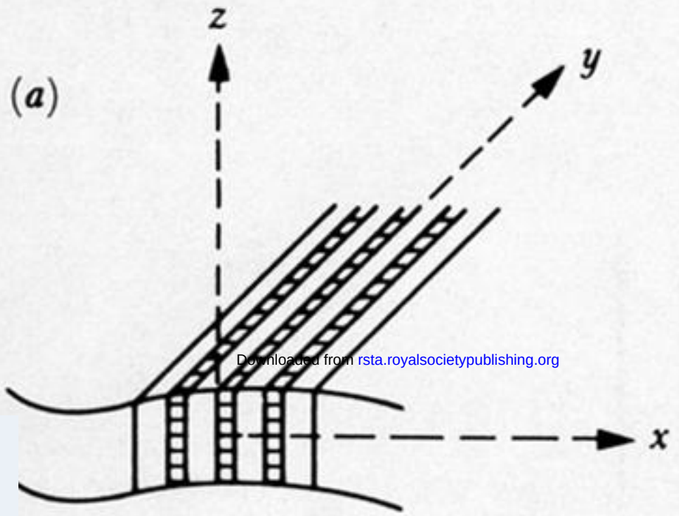

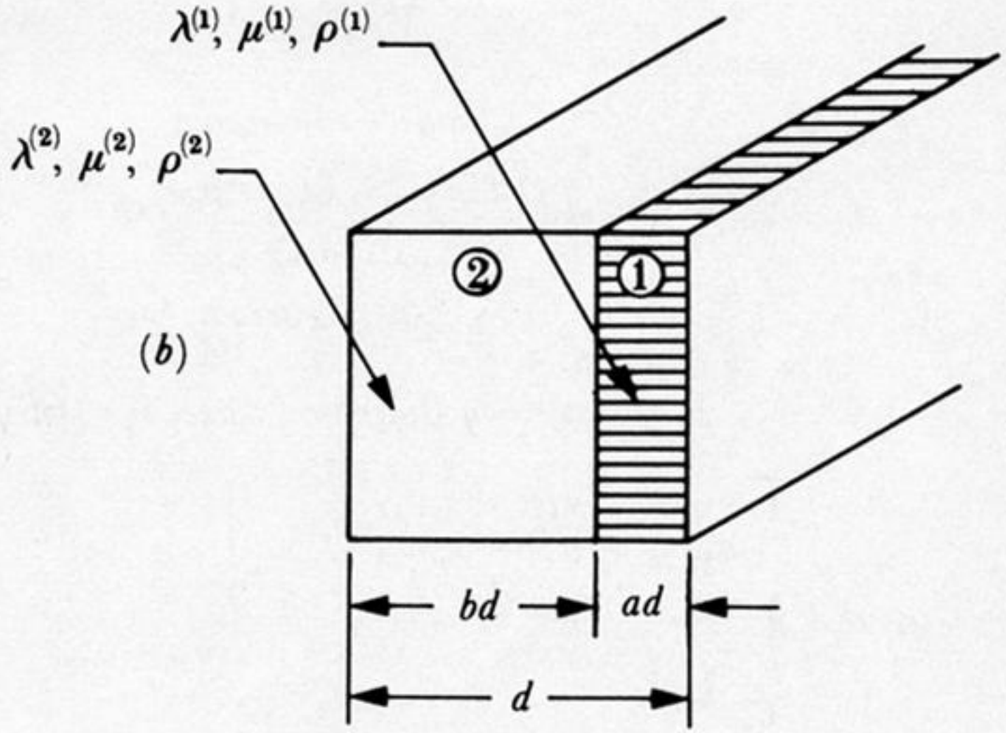

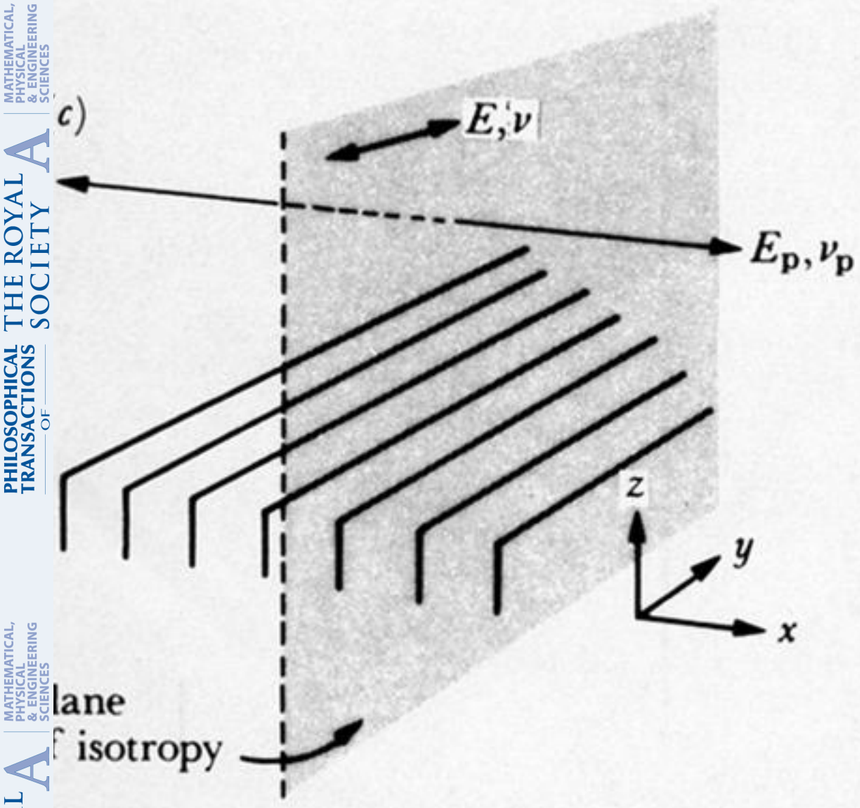

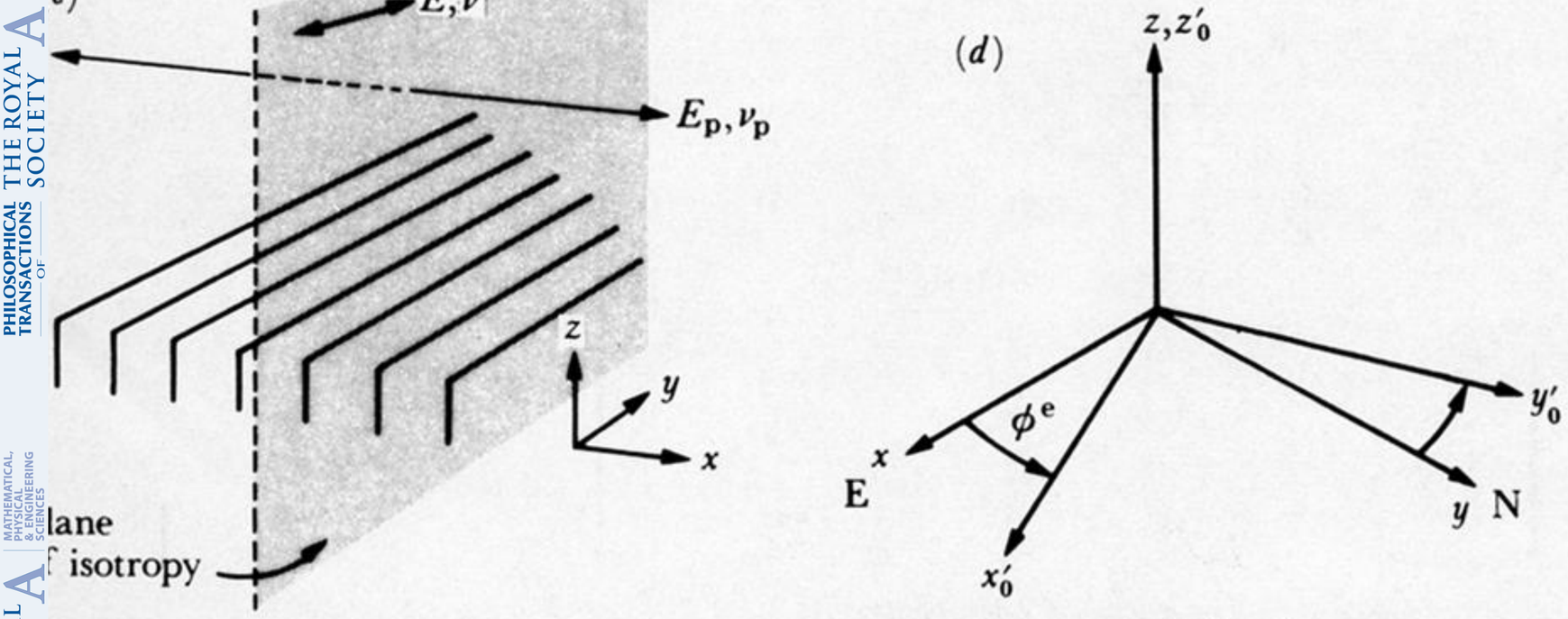

FIGURE 3. Three-dimensional, two-component laminate model: (*a*) coordinates of the laminate; (*b*) faulted (1) and unfaulted (2) phases; (*c*) interpretation of moduli E, E_p, ν and ν_p in terms of crustal fault orientation; (*d*) counter-clockwise rotations from coordinates of transverse isotropy (x, y, z) to attitude of fault plane $(y'-z')$, yielding the inverse of the rotation matrix given by Rose (1957) (see equation (4) in text). (E and E_p are the Young moduli for tension or compression in the plane of isotropy and normal to the plane; respectively; dip $= 90° - \psi^e$; strike $= \phi^e$.)